Non-collinear Magnetism, Hidden Symmetry Lowering and Magneto-transport Effects in Antiperovskite Nitrides

Dissertation

Zur Erlangung des Doktorgrades der Naturwissenschaften
(Dr. rer. nat.)

der

Naturwissenschaftlichen Fakultät II
Chemie, Physik und Mathematik

der Martin-Luther-Universität
Halle-Wittenberg

Vorgelegt von

Herrn Berthold Henry Rimmler

Gutachter:
Prof. Dr. Stuart S. P. Parkin
Prof. Dr. Ingrid Mertig
Prof. Dr. Christian Back

Tag der öffentlichen Verteidigung:
31.01.2024

Eidesstattliche Erklärung

Hiermit erkläre ich, dass ich die vorliegende Arbeit selbstständig verfasst und keine anderen als die angegebenen Quellen und Hilfsmittel benutzt habe. Alle Stellen der Arbeit, die wörtlich oder sinngemäß aus anderen Quellen übernommen wurden, sind als solche kenntlich gemacht. Ich habe keine vergeblichen Promotionsversuche unternommen und keine Dissertation an einer anderen wissenschaftlichen Einrichtung zur Erlangung eines akademischen Grades eingereicht. Ich bin weder vorgestraft noch sind gegen mich Ermittlungsverfahren anhängig.

Halle (Saale), den 02.01.2024,

Berthold Rimmler

Acknowledgments

This work would not have been possible without the support of many people. First, I want to express my deepest appreciation to Prof. Stuart Parkin for giving me the opportunity to pursue a PhD in his group at the Max Planck Institute of Microstructure Physics and for giving me the freedom to find and shape my own research project as well as for his support in the process. I am also deeply indebted to Prof. Ingrid Mertig at the Martin-Luther-Universität Halle-Wittenberg for her valuable co-supervision, interesting discussions and fruitful collaboration. Furthermore, I thank the Max Planck Gesellschaft and the Max Planck Research School for Science and Technology of Nano-Systems.

I would like to extend my sincere thanks to the many collaborators in this research project. Most notably, I would like to thank Binoy Krishna Hazra and Banabir Pal with help in sample preparation and device fabrication, James Taylor for his support in experiment design and Holger Meyerheim and Katayoon Mohseni for sharing their passion for X-ray diffraction with me. Furthermore, I'd like to acknowledge the help of Amilcar Bedoya-Pinto, Hakan Deniz, Ilya Kostanovskiy, Robin Neumann, Arthur Ernst, Malleswararao Tangi, Anagha Mathew and Prajwal Rigvedi. For their organizational support in the PhD process, I greatly acknowledge Simone Jäger, Michael Strauch and Antje Paetzold. For technical assistance I thank Norbert Schammelt, Florian Thiele, Kai-Uwe Aßmann, Mike Bormann and Julia Ducke.

Over the last four years I was fortunate to have met many great colleagues and friends, who made this journey a lasting experience for me. Many thanks to my office mates Avanindra Kumar Pandeya, Ajesh Kollakuzhiyil Gopi and Zihan Yin (I am very sorry uncontrolled whistling and singing in the office). I am also grateful to Lukas Fischer, Jiho Yoon, André Farinha, Pedram Bassirian, Andrea Migliorini, Jae-Chun Jeon and Pierre-Jean Zermatten.

I could not have undertaken this journey without the help of my family and my dear friends. I thank my parents for their inexhaustible encouragement and guidance. Words cannot express my sincere gratitude to my wonderful partner Svenja for her unconditional love and support both in good times and in times of crisis. Last but not least, I want to express my gratitude to Lukas, Franziska, Tobias, Arne, Noah, Mechthild and Julian.

Abstract

Antiferromagnets are promising materials for next-generation spintronic data storage devices due to their negligible magnetization and associated magnetic stray fields that limit the usefulness of conventional ferro- and ferrimagnets at the nanoscale. Of particular interest are a class of antiferromagnets that have non-collinear spin textures and which can display unusual transport properties, of which particular examples are an anomalous Hall effect, a longitudinal spin polarization of charge currents, and a spin Hall effect with unusual spin polarization directions. These effects can be readily observed only if the sample is set predominantly into a single antiferromagnetic domain state. One way to enable control of the domain structure is if the antiferromagnetic order is perturbed and displays weak moments due to spin canting. In thin films of cubic non-collinear antiferromagnets this imbalance was previously assumed to require substrate strain-induced tetragonal distortions. In this work it is found that non-collinear antiferromagnets with an antiperovskite structure may exhibit non-zero transport effects in the absence of such tetragonal distortions. In this case, net moments result instead from structural symmetry lowering induced by displacements of the manganese atoms away from high-symmetry positions. These displacements preserve the bulk-like lattice constants of the films and, therefore, remain hidden in structural characterization by X-ray diffraction when only probing the lattice metric. Instead, structural refinement of a large set of scattering vectors is required to resolve the local atomic positions. In the antiperovskite Mn_3SnN these displacements enable the observation of an anomalous Hall effect with an unusual temperature dependence, which is conjectured to be due to a previously unexplored temperature-dependent spin rotation. These findings challenge the long-held assumption that tetragonal distortions are required to observe non-zero transport effects in cubic non-collinear antiferromagnets. Furthermore, the experimental results and comparison with the literature suggest that manganese displacements are common in antiperovskite nitrides and that they may enable the observation of transport effects beyond the anomalous Hall effect.

Zusammenfassung

Antiferromagnete sind aufgrund ihrer vernachlässigbar kleinen Magnetisierung und damit einhergehenden geringen magnetischen Streufeldern vielversprechende Materialien für die nächste Generation spintronischer Datenspeicher, deren Skalierbarkeit durch die Verwendung von herkömmlichen Ferro- und Ferrimagneten stark eingeschränkt ist. Von besonderem Interesse sind hierbei Antiferromagnete, die nichtkollineare Spintexturen aufweisen, die zu ungewöhnlichen Transporteigenschaften führen können, wie zum Beispiel ein anomaler Hall-Effekt, longitudinale Spinpolarisation von Ladungsströmen und ein Spin-Hall-Effekt mit ungewöhnlichen Spinpolarisationsrichtungen. Diese Effekte lassen sich nur beobachten, wenn die Probe überwiegend in einem Eindomänenzustand vorliegt. Eine Möglichkeit, die Domänenstruktur zu kontrollieren, besteht in der Störung der antiferromagnetischen Ordnung, was zur Entwicklung schwacher Momente aufgrund von Spinverkantung führt. Im Fall von dünnen Schichten kubischer, nichtkollinearer Antiferromagnete wurde bisher angenommen, dass dieses Ungleichgewicht tetragonale Verzerrungen erfordert, die durch Gitterfehlanpassungen entstehen. In dieser Arbeit wird gezeigt, dass nichtkollineare Antiferromagnete mit einer Antiperowskit-Struktur auch ohne solche tetragonalen Verzerrungen messbare Transporteffekte aufweisen können. In diesem Fall entstehen Nettomomente durch Verringerung der Kristallsymmetrie, hervorgerufen durch die Verschiebung der Manganatome aus hochsymmetrischen Positionen. Diese Verschiebungen erhalten die Gitterkonstanten des Volumenkristalls in den Schichten und bleiben daher bei der strukturellen Charakterisierung durch Röntgenbeugung verborgen, wenn nur die Gittermetrik untersucht wird. Stattdessen ist eine strukturelle Verfeinerung eines großen Satzes von Streuvektoren erforderlich, um die lokalen Atompositionen aufzulösen. Im Antiperowskit Mn_3SnN ermöglichen diese Verschiebungen die Beobachtung eines anomalen Hall-Effekts mit einer ungewöhnlichen Temperaturabhängigkeit, von der vermutet wird, dass sie auf bisher weitgehend unerforschte temperaturabhängige Spinrotationen zurückzuführen ist. Diese Ergebnisse stellen einen Bruch mit der allgemeinen Annahme dar, dass tetragonale Verzerrungen erforderlich sind, um Nettotransporteffekte in kubischen nichtkollinearen Antiferromagneten zu beobachten. Darüber hinaus deuten die experimentellen Ergebnisse und der Vergleich mit der Literatur darauf hin, dass Manganverschiebungen in Antiperowskitnitriden üblich sind und dass sie die Beobachtung von Transporteffekten über den anomalen Hall-Effekt hinaus ermöglichen könnten.

Glossary

Terms	
AF	Antiferromagnet, Antiferromagnetic
AFM	Atomic force microscopy, microscopic
AHC	Anomalous Hall conductivity
AHE	Anomalous Hall effect
ANC	Anomalous Nernst conductivity
ANE	Anomalous Nernst effect
IP	In-plane
LGR	Laue group
LSP	Longitudinal spin polarization, Longitudinally spin-polarized
MAE	Magneto-crystalline anisotropy energy
MBE	Molecular beam epitaxy
NCAF	Non-collinear antiferromagnet, antiferromagnetic
OP	Out-of-plane
PLD	Pulsed laser deposition
RBS	Rutherford backscattering spectroscopy
SHE	Spin Hall effect
SIXC	Six-circle diffractometer
SQUID	Superconducting quantum interference device
SOT	Spin-orbit torque
STT	Spin-transfer torque
TEM	Transmission electron microscopy, microscopic
VSM	Vibrating sample magnetometry
XMCD	X-ray circular magnetic dichroism
XRD	X-ray diffraction
XRR	X-ray reflectivity

Compounds, Materials and Chemicals	
BTO	$BaTiO_3$
KTO	$KaTiO_3$
LSAT	$(LaAlO_3)_{0.3}(Sr_2TaAlO_6)_{0.7}$
MGN	Mn_3GaN
MSN	Mn_3SnN
STO	$SrTiO_3$

Contents

Eidesstattliche Erklärung i

Acknowledgments iii

Abstract v

Zusammenfassung vii

Glossary ix

Contents xi

Part I Introduction

---

1 Novel Magnets for Spintronics 3

2 Experimental Methods 7

- 2.1 Thin Film Growth by Sputtering 7
  - 2.1.1 Reactive DC Sputtering 7
  - 2.1.2 Epitaxial Thin Films 9
- 2.2 X-ray Diffraction for Thin Film Characterization 12
  - 2.2.1 Kinematic Diffraction 12
  - 2.2.2 Four-circle Diffractometer and Thin Film Characterization 15
  - 2.2.3 Six-circle Diffractometer 17
- 2.3 Magnetic Characterization 20
  - 2.3.1 Vibrating Sample Magnetometry 20
  - 2.3.2 X-ray Magnetic Circular Dichroism 22

3 The Anomalous Hall Effect: Theory and Measurement 25

- 3.1 Semi-classical Transport Theory 25
- 3.2 Anomalous Hall Effect in Cubic Non-collinear Antiferromagnets 26

Part II Identification of Promising Antiperovskite Nitrides

4 Mn-based Antiperovskite Nitrides 31

4.1 Chemistry and Crystal Structure 31

4.2 Magnetism 33
4.2.1 Overview 33
4.2.2 Triangular Magnetic Structures 33
4.2.3 Chirality in Triangular Magnetic Structures 37
4.2.4 Other Magnetic Structures 38

4.3 Electronic Structure and Exchange 39
4.3.1 Valencies in Mn_4N 39
4.3.2 Band Structure 39
4.3.3 Magnetic Exchange 40

4.4 Implications 42

Part III Crystallography, Magnetism and the Anomalous Hall Effect in Mn_3SnN

5 Lead-in 47

6 Mn_3SnN Thin Films 49

6.1 Growth Procedure 49
6.1.1 Substrate Preparation of $SrTiO_3$ 49
6.1.2 Growth Parameter Optimization 50

6.2 Thin Film Characterization by XRD, AFM and TEM 51

6.3 Magnetic Properties 54
6.3.1 SQUID-VSM 55
6.3.2 XMCD 58

7 Anomalous Hall Effect Measurements 61

7.1 Hall Effect Measurements 62
7.1.1 Facet Dependence 62
7.1.2 Temperature Dependence 65

7.2 Discussion 68

8 Hidden Atomic Manganese Displacements 71

8.1 Lattice Strain in (001)-oriented Mn_3SnN 71

8.2 Structural Refinement Procedure 72

8.3 Centrosymmetric Models 75

8.4 Non-centrosymmetric Models 78
  8.4.1 Structural Refinement 78
  8.4.2 Temperature and Thickness Dependence 80
  8.4.3 Summary of Structural Models 82

8.5 Interpretation of the Probability Density Function 82

9 Resolving the Anomalous Hall Effect in Mn_3SnN 85

9.1 Magneto-structural Coupling and Spin Canting in Antiperovskite Nitrides 85

9.2 Manganese Displacements and the Anomalous Hall Effect 89
  9.2.1 Crystal Structure, Magnetism and Magneto-Transport 89
  9.2.2 Comparison of Mn_3SnN and Mn_3Sn 91

9.3 Open Questions and Outlook 93

Part IV Manganese Displacements and Transport in Non-collinear Antiferromagnets

10 Transport Effects Beyond the Anomalous Hall Effect 99

10.1 Lead-in 99

10.2 Magnetic Domains in Charge and Spin Transport 100
  10.2.1 Anomalous Nernst Effect 100
  10.2.2 Spin Polarized Current and the Spin Hall Effect 101
  10.2.3 Symmetry Analysis: The Role of Magnetic Domains 102

10.3 The Role of Mn Displacements in the Observation of Intrinsic Transport Effects 106
  10.3.1 Overview 106
  10.3.2 Anomalous Hall Effect and Related Effects 106
  10.3.3 Spin Hall Effect in Mn_3GaN and Mn_3SnN 108
  10.3.4 Mn Displacements in Mn_3GaN and Domain Structure Control . . 109
  10.3.5 Longitudinal Spin Polarization 111
  10.3.6 Summary and Open Questions 113

11 Conclusions, Implications and Open Questions 115

Part V Appendices

A ST-FMR Measurements of Mn_3SnN Thin Films 121

Curriculum Vitae 127

List of Figures 129

List of Tables 133

Bibliography 135

Part I

Introduction

Chapter 1

Novel Magnets for Spintronics

The research field of spintronics (short for spin electronics) attempts to use the spin degree of freedom of electrons for data storage and computing technologies. Thereby, it goes beyond the charge-based paradigm of conventional complementary metal-oxide-semiconductor (CMOS) technology, which is ultimately limited by quantum effects at the nanoscale [1]. Historically, spintronics has heavily relied on ferromagnets as key active materials, as they allow for effective storage and read-out of data. However, ferromagnets come at the cost of limited scalability, power consumption and speed [2]. These shortcoming call for the development of novel magnetic materials for spintronics.

Antiferromagnets (AFs) are such a class of magnetic materials with the potential to replace ferromagnets in next generation spintronic devices [2–5]. AFs exhibit magnetic ordering but zero net magnetization. So far, they have mostly played passive, albeit crucial roles in spintronics. For instance, they were integral to the development of spin valves and magnetic tunnel junction, which are key components in magnetic data storage technologies and are used as magnetic field sensors in magnetic hard drives and as storage elements in magnetic random access memory (MRAM) devices [6, 7], which is currently the most advanced commercially available spintronic data storage technology. Magnetic tunnel junctions are also key components in the emerging racetrack memory technology [8, 9]. In recent years, AFs have proven to be promising active materials for spintronic devices, because of their robustness against magnetic fields, the absence of magnetic stray fields, ultrafast dynamics and large magneto-transport effects [2, 3]. Furthermore, antiferromagnetism is more abundant in nature than ferromagnetism and AFs span the whole material range from insulators to superconductors. In combination with the observed presence of non-trivial topological phases found in some AFs they, thereby, greatly enlarge the material playground of spintronics [4, 10].

The class of non-collinear antiferromagnets (NCAFs) comprises of materials with spin configurations that are more complex than the collinear two-sublattice structures such as those found in MnO, for instance [11]. In this work, the term is used to refer to materials with non-collinear and coplanar spin textures that are found in many Mn-based nitride and non-nitride compounds with generic formulae Mn_3ZN and Mn_3Z, wherein Z are typically (post-)transition metal elements. These materials have in common that the Mn atoms, on which the spins reside, form trigonal Kagome lattices, which causes geometric frustration of the spins and leads to the formation of distinct triangular spin textures. Among these, nitrides with cubic antiperovskite crystal structures are particularly interesting, as they also display various other kinds of collinear and non-collinear ferromagnetic, ferrimagnetic and antiferromagnetic ordering as well as phases with temperature-dependent spin rotation and magnetic structures with long magnetic propagation vectors [12, 13].

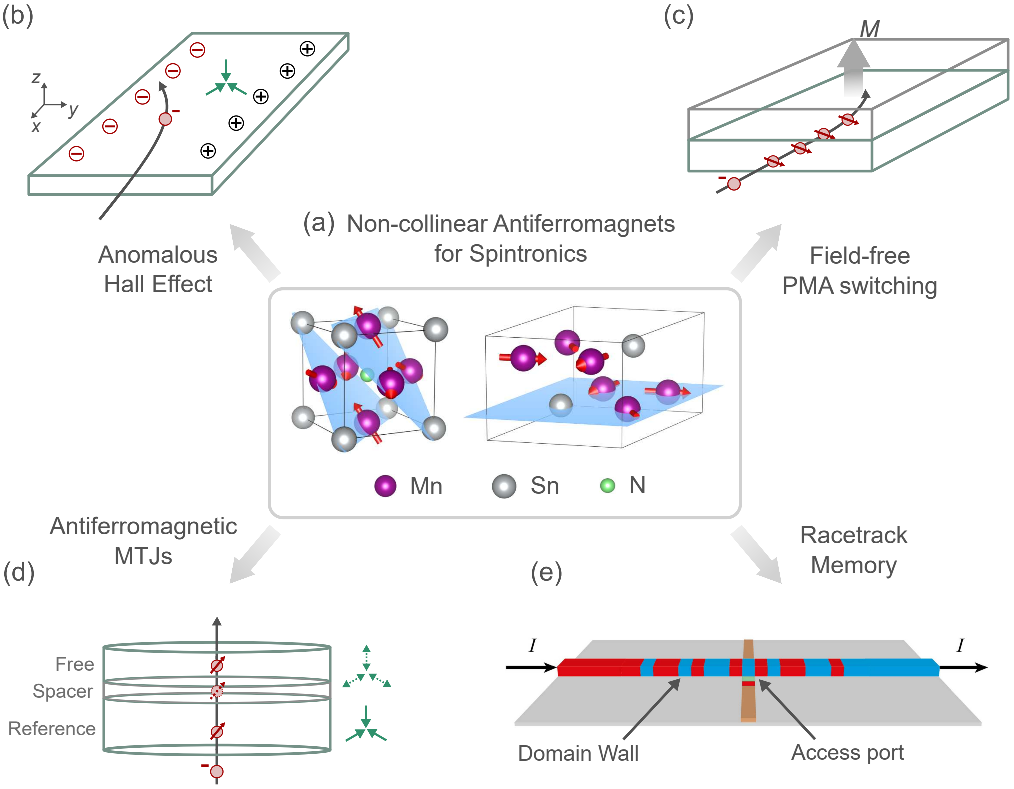

Figure 1.1: Potential applications of non-collinear antiferromagnets (NCAFs) in spintronics. NCAFs such as Mn_3SnN and Mn_3Sn, shown in (a), exhibit transport effects usually not associated with antiferromagnets, such as (b) an anomalous Hall effect and longitudinal charge current polarization and (c) a spin Hall effect with spin polarization directions allowing for field-free switching of magnetic layers perpendicular magnetic anisotropy (PMA). Thereby, they may replace ferromagnets in (d) magnetic tunnel junctions used in MRAM and (e) racetrack memory devices, in which NCAFs may also replace ferromagnets in the racetrack itself. Figure (e) taken and adapted from Ref. [9].

NCAFs have gained recent attention in spintronics due to the presence of interesting magneto-transport effects arising from symmetry-allowed Berry curvature in crystal momentum space [14], as schematically shown in Figure 1.1. Some of these effects are unexpected in antiferromagnets because of their vanishing magnetization. For instance, NCAFs display an intrinsic anomalous Hall effect (AHE) [15–17] and charge currents become spin-polarized when passing through a NCAF [18–21]. NCAFs also exhibit the spin Hall effect (SHE), which is conventionally associated with paramagnetic heavy metals with strong spin-orbit coupling [22, 23]. Furthermore, the spin currents generated in NCAFs have spin polarization directions that cannot be generated in heavy metals and that allow for magnetic field-free switching of magnetic layer with perpendicular magnetic anisotropy (PMA) [24–27]. These examples show that NCAFs are interesting materials for next-generation spintronic applications, in which they may replace conventionally used materials. For instance, they may substitute ferromagnets in magnetic tunnel junctions used in MRAM devices and in the access ports of racetrack memory devices. In racetrack memory, they may also supersede synthetic antiferromagnets in the racetrack itself [28]. Furthermore, they may be an alternative to heavy metals in spin-orbit torque devices with the additional functionality of field-free spin-orbit torque switching of magnetic layers with perpendicular magnetic anisotropy.

Using NCAFs in spintronic devices requires control of the magnetic domain structure. While ferromagnets can be easily magnetized and switched by external magnetic field or upon the application of spin torque, generation of a single-domain state in NCAFs is more challenging and there is a gap in knowledge as to the exact mechanisms allowing for domain structure control in cubic NCAFs. One of the major advantages of NCAFs, namely their insensitivity to magnetic field, is also a drawback in that it necessitates novel approaches to control the magnetic domain state. The non-collinear antiferromagnetic (NCAF) spin textures of the hexagonal compounds Mn_3Sn and Mn_3Ge exhibit intrinsic spin canting that gives rise to weak moments coupled to the magnetic textures. These moments allow to control the NCAF domain structure [29–31]. Cubic NCAFs, on the other hand, are fully compensated and, therefore, require an additional mechanism to achieve domain control. It was previously assumed that in thin films of cubic NCAFs substrate strain-induced tetragonal distortions of the films play that role [27, 32–35].

However, in this work it is shown that non-zero transport signals are observed in (001)-oriented thin films of the cubic NCAF Mn_3SnN despite them exhibiting a cubic lattice metric. It is shown that in this material domain structure control is not enabled by tetragonal distortion but, instead, by displacements of the Mn atoms away from high symmetry position. The observation of these displacements requires detailed structural analysis as they remain hidden in conventional thin film X-ray characterization that only probes the lattice metric of the films. It is shown that these displacements lead to spin canting and the emergence of small net moments that allow for control of the NCAF domain structure. Thereby, they enable the observation of a non-zero AHE. Furthermore, the AHE displays an unusual temperature dependence, which can be explained by the presence of material-intrinsic coherent spin rotation as a function of temperature. In contrast, Mn_3SnN thin films with (111)-growth orientation, in which Mn displacements are absent, do not display an AHE. Lastly, it is found that the phase diagram of Mn_3SnN in thin films form is very different to that in bulk samples [36].

It is further shown that Mn displacements are also present in the isostructural Mn_3GaN and are, therefore, not limited to a single material or deposition technique. Mn_3GaN was previously shown, by spin-transfer ferromagnetic resonance, to exhibit a SHE in which the spin polarization direction is not limited to be perpendicular to the charge and spin current direction [27]. The Mn_3GaN films used in that work appear cubic from standard structural characterization. However, similar to the AHE, the unconventional torque components are inconsistent with a single-domain state that is expected in a sample with bulk-like cubic crystal structure.

The experimental findings presented here as well as comparison with literature suggest that Mn displacements are common in antiperovskite nitrides and that they may enable the observation of magneto-transport effects beyond the AHE. Therefore, this work also systematically analyzes the symmetries of the charge and spin conductivity tensors of the spin textures of cubic NCAF. Thereby, the effect of different kinds of NCAF domain on various magneto-transport effects is determined and the results compared with the existing literature.

The work is structured as follows. The remainder of this part introduces the experimental methods employed here and lays the conceptual foundation of the observation of the AHE in NCAFs. Afterwards, the crystallographic and magnetic textures of various Mn-based antiperovskite nitrides are reviewed in Part II. Part III then presents the optimization procedure of the growth parameters of (001)- and (111)-oriented Mn_3SnN thin films, compositional and structural thin film characterization as well as AHE measurements. Afterwards, the structural refinement of the Mn_3SnN thin films using different structural models and as a function of temperature and film thickness is presented. It is then established that the observation of a non-zero AHE in (001)-oriented Mn_3SnN can be explained by the presence of atomic Mn displacements. Lastly, Part IV elaborates on the implications of these findings in aid of presenting structural refinement of Mn_3GaN thin films and symmetry analysis of the charge and spin conductivity tensors and it is discussed how the results obtained here relate to the existing literature.

Chapter 2

Experimental Methods

2.1 Thin Film Growth by Sputtering

2.1.1 Reactive DC Sputtering

The growth of epitaxial thin films places high requirements on the quality of the substrate surface [37, 38]. Even at a vacuum of 1×10^{-6} mbar (high vacuum conditions) enough molecules in the air to form a monolayer of adatoms (water, hydrocarbons etc.) are impinging on the substrate surface every second. Therefore, ultra high vacuum (UHV) conditions with pressures down to 1×10^{-9} mbar to 1×10^{-10} mbar are required for the growth of epitaxial thin films [38].

To establish UHV conditions in a vacuum chamber numerous different kinds pumps are employed that can be categorized into three main types based on their function in the process of generating UHV conditions [39]. First, roughening pumps (scroll pumps, diaphragm pumps, rotary pumps etc.) operate from ambient pressure to high vacuum pressure, typically down to 1×10^{-6} mbar. Secondly, in order to reach UHV conditions, turbo molecular pumps are employed, which consist of sets of rapidly rotating rotor blades to transfer momentum to impinging molecules to push them out of the chamber and toward a roughening pump connected in series. Turbo molecular pumps require that the molecules are moving freely in the chamber and are not adsorbed at the chamber walls and other surfaces. Therefore, the vacuum chamber needs to be baked out, i.e. heated to up to 200 °C in order to release adsorbed molecules, especially water. Lastly, additional pumps such as ion getter pumps or titanium sublimation pumps can be used to improve the vacuum further. These pumps operate on the principle of trapping gas molecules. Ion getter pumps ionize remaining molecules and implant them into a metal sheet by applying a strong electric field. On the other hand, titanium sublimation pumps periodically cover their walls with Ti (through sublimation from a Ti target), which strongly absorbs water molecules, thereby trapping them.

A broad range of techniques has been developed to grow thin films [37]. They can be broadly categorized into chemical vapor deposition (CVD) and physical vapor deposition (PVD) techniques. The most commonly used PVD techniques employed in the field of spintronics are sputtering, molecular beam epitaxy (MBE) and pulsed laser deposition (PLD). They are based on the principle of creating a beam of molecules or a plume of plasma particles that are directed toward a substrate, at which they condense. They differ in the methods with which the atoms are transferred from a solid target to the substrate.

In MBE a molecular beam of molecules is generated by evaporating a precursor from an effusion cell by heating it either thermally or using an electron beam. Because the vapor pressure of an element depends on its atomic mass, in order to grow complex materials, co-evaporation from multiple sources is required. A more direct approach is taken in PLD. The material is ablated directly from a pre-mixed target (usually a complex oxide) by focusing an intense laser beam onto the target, thereby ablating the material and bringing it directly into the plasma phase. This generally allows for stoichiometric transfer of the target material to the substrate, which makes this technique very suitable for very complex compounds, especially oxides.

In this work, reactive DC sputtering is employed to grow complex metal nitride films. This technique is commercially well-established and allows for the growth of high quality (epitaxial) thin films on large-scale wafers, while maintaining a simple setup and allowing for a high degree of automation.

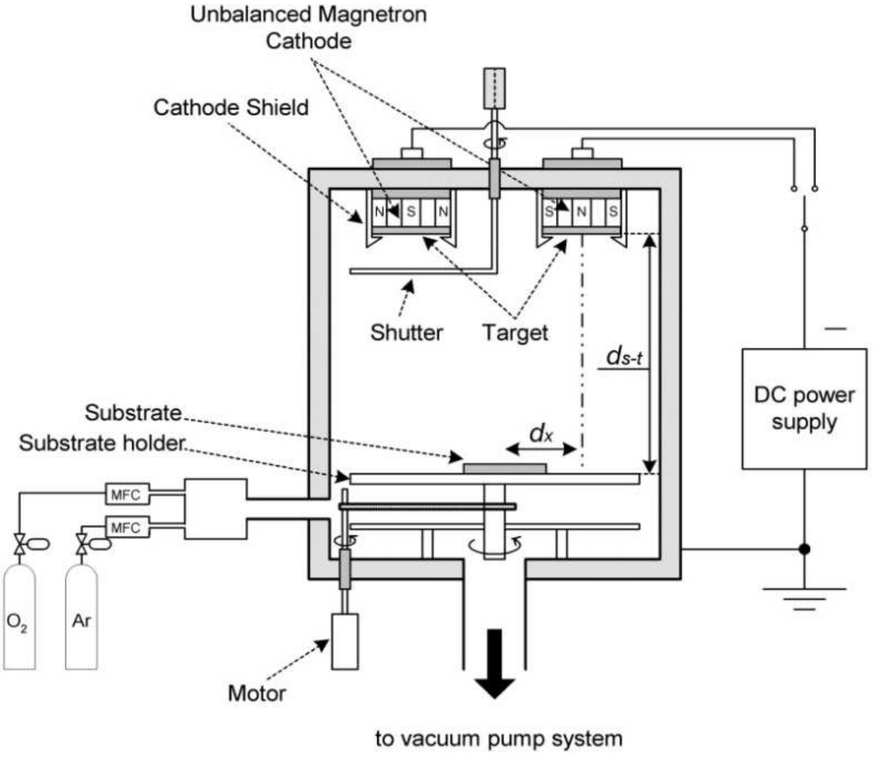

Figure 2.1: Schematic of a typical reactive DC sputtering setup. Taken from Ref. [40].

Figure 2.1 schematically shows a typical reactive DC sputtering setup. A UHV chamber is connected to several pumps and pressure gauges as well as an inlet for argon (required for the sputtering process) and a reactive gas (oxygen in the figure, nitrogen in the case of the nitrides grown in this work). A substrate is attached to a sample holder plate and can be heated to elevated temperatures (in this work from room temperature to up to

600 °C). In the above figure the substrate is shown below the targets, while in the setup used in this work it is placed above the targets. The substrate is rotated to ensure uniformity of the film. Facing the substrate are two sputtering targets at a distance of typically a few tens of centimeters. For the growth of Mn_3SnN, high-purity, commercially available Mn and Sn targets are co-sputtered. A shutter can be used to protect the targets from contamination from the other target, if they are not co-sputtered at the same time.

The sputtering process is initiated by igniting a dense metal plasma by applying a high electric bias to the target (in the deposition system used in this work around 400 V). Ar atoms are ionized and accelerated onto the target, where they impinge and transfer momentum to the metal atoms. The metal atoms are sputtered from the target surface and may be ionized in the plasma as well. In magnetron sputtering targets, water-cooled permanent magnets behind the target trap the ions in the plasma along the magnetic field lines, thereby localizing the plasma further at the target. The particles in the plasma plume reach the substrate surface, at which several processes can occur. The particles may be implanted into the substrate (at high energy), they may absorb at the surface, diffuse, form clusters or desorb again. The probability for a particle to be deposited at the substrate surface is parametrized by the sticking coefficient. The sticking coefficient depends on the plasma species, the substrate material and the substrate temperature. By applying reactive gases such as O_2 or N_2 to the chamber in addition to Ar, the plasma particles may further react and form metal oxides or nitrides at the substrate surface.

The outcome of a deposition of a complex metal nitride thin films by DC magnetron sputtering depends on numerous process parameters. First, the composition of the films is largely controlled by the DC powder supplied to the individual sputtering targets. The N content is further controlled by the total gas pressure and gas flow as well as the ratio of Ar to N_2 in the background gas. Furthermore, the substrate temperature affects the sticking coefficients of the different plasma species at the substrate. Furthermore, it greatly affects the growth kinetics by affecting the relative rates of diffusion, cluster nucleation and growth, island formation and (re-)crystallization. The substrate temperature is also the main parameter to control the epitaxial relationship of substrate and film. This aspect of thin film growth is further discussed in the next chapter.

2.1.2 Epitaxial Thin Films

In this work, heteroepitaxial thin films of the antiperovskite nitride Mn_3SnN are grown on single crystalline $SrTiO_3$ substrates. Epitaxy refers to a special type of crystal growth, in which a single crystalline thin film grows with well-defined orientation with respect to a single-crystalline substrate that acts as a seed layer. In the special case of heteroepitaxy the film and substrate materials are dissimilar [38,41]. Heteroepitaxy requires a low lattice mismatch of substrate and film f:

$$f = \frac{a_f - a_s}{a_s} \tag{2.1}$$

Herein, a_f and a_s are the in-plane lattice parameters of film and substrate. In the case of the growth of Mn_3SnN on $SrTiO_3$, the lattice mismatch is 3.9 %. Therefore, the film film is under compressive strain. There are two generally accepted mechanism for strain relaxation in thin films: tetragonal distortion and formation of misfit dislocations, as shown in Figure 2.2. Misfit dislocations are formed at the interface, if the elastic strain energy exceeds the energy stored in the stress field of a newly formed dislocation. Dislocations typically form above a critical lattice mismatch and film thickness [38].

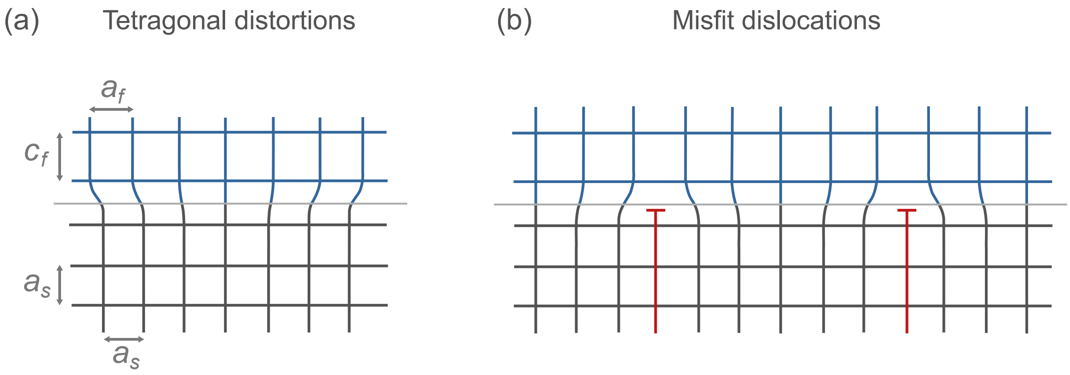

Figure 2.2: Common mechanisms for strain relaxation in epitaxial thin films. Schematic representation of the interface between an epitaxial film with lattice parameter a_f and a substrate with lattice parameter a_s with $a_f > a_s$. The strain due to the lattice mismatch can be released through (a) tetragonal distortions or (b) the formation of misfit dislocations (marked in red) at the interface.

Thin Film Growth Particles in the sputtering plasma arrive at the substrate and undergo various processes, including condensation at the surface or at special sites such as terraces or already formed islands, diffusion, re-evaporation, implantation and nucleation of clusters. The kinetic rates of these processes are temperature-dependent. There are three growth modes to describe the growth of thin films: Layer-by-layer, Stransky-Krastanov and island growth [37, 38], as shown in Figure 2.3

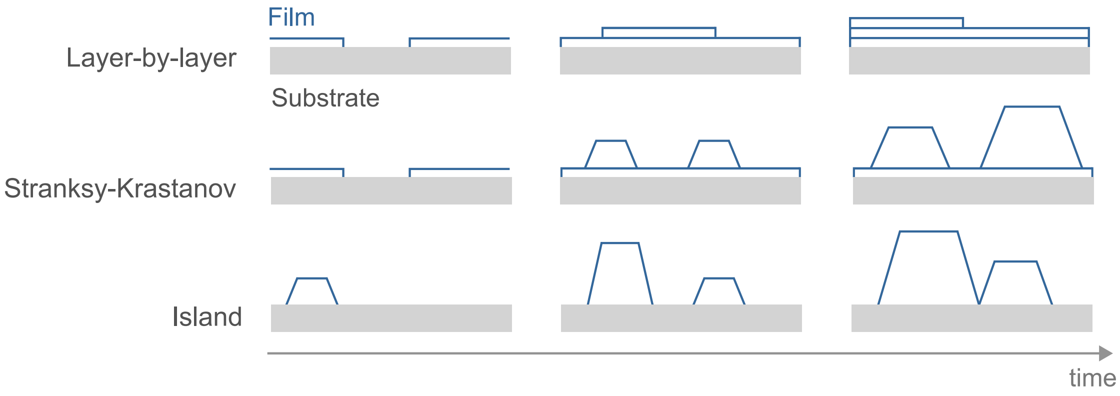

Figure 2.3: Schematic representations of common thin film growth modes: Layer-by-layer, Stransky-Krastanov and island growth.

Thin films grow in a *layer-by-layer* fashion, if the interaction between film species with the substrate is stronger than with other film species. This growth mode is also known as *Frank-van der Merve* growth. In contrast, if there is a strong interaction between the film species, islands start to form to reduce interaction with the substrate (island or *Volmer-Weber* growth mode). *Stransky-Krastanov* growth is an intermediate mode. It occurs, when island formation becomes energetically favorable after growth of a few atomic monolayers in layer-by-layer growth mode.

The different growth modes result from differences in surface energy. The atomic bonds at the surface differ from the bulk. This gives rise to a surface tension (or surface energy) γ. The wetting angle of a film deposit on the substrate is given by Young's equation:

$$\gamma_s = \gamma_{s/f} + \gamma_f \cos\phi \tag{2.2}$$

Herein, γ_s and γ_f are the surface energies of substrate and film (in contact with the surrounding metal vapor) and $\gamma_{s/f}$ is the interfacial energy between substrate and film. ϕ is the wetting angle of a deposit on the substrate surface, as shown in Figure 2.4). Layer-by-layer growth occurs if $\gamma_s \geq \gamma_{s/f} + \gamma_f$. On the other hand, island growth occurs if $\gamma_s < \gamma_{s/f} + \gamma_f$, which is often the case for the growth of metal films on oxide substrates. This shows that the growth mode is controlled not only by the lattice mismatch of substrate and film, but also by their surface and interface chemistry.

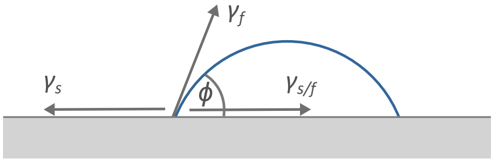

Figure 2.4: Schematic representation of the energy balance of a deposit on a substrate surface. ϕ is the wetting angle, γ_s and γ_f are the surface energies of substrate and film and $\gamma_{s/f}$ is their interfacial energy.

2.2 X-ray Diffraction for Thin Film Characterization

2.2.1 Kinematic Diffraction

X-ray diffraction (XRD) is a well-established method for structural investigation of solids [42–44]. Kinematic diffraction is a good approximation for thin films, as they are mosaic crystals, which comprise of many coherently scattering crystallites. Kinematic diffraction assumes that the primary beam does not suffer any intensity loss, that secondary beams are not scattered again and that possible interference between primary beam and scattered beam can be ignored.

X-ray diffraction means X-ray scattering from a periodic structure, in this case from electrons in atoms arranged periodically in a crystal. The monochromatic plane wave of an incident X-ray photon accelerates the electron, which itself acts as a point source of a wave with the same frequency. Interference of waves scattered from electrons at different scattering centers A and B occurs. This is shown in Figure 2.5(a).

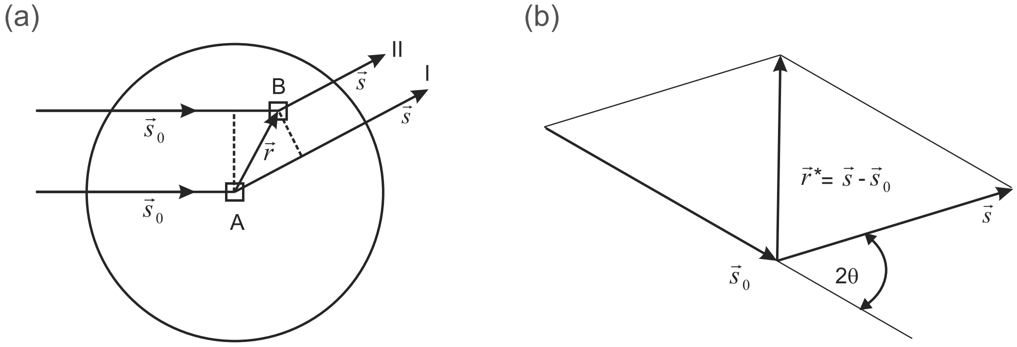

Figure 2.5: (a) Scattering of a X-ray beam from matter. (b) The definition of the scattering vector $\boldsymbol{q} = \boldsymbol{r}^*$. Taken from Ref. [43].

The phase difference between the scattered waves is

$$\Delta\varphi = \frac{2\pi}{\lambda}(\boldsymbol{s} - \boldsymbol{s_0}) \cdot \boldsymbol{r} = 2\pi(\boldsymbol{q} \cdot \boldsymbol{r}) \tag{2.3}$$

Herein, λ is the wavelength of the incident photon, $\boldsymbol{s_0}$ and $\boldsymbol{s}$ are the wave vectors of the incident and scattered photon and $\boldsymbol{q}$ is the scattering vector:

$$\boldsymbol{q} = \frac{1}{\lambda}(\boldsymbol{s} - \boldsymbol{s_0}) \tag{2.4}$$

$$|\boldsymbol{q}| = \frac{2\sin\theta}{\lambda} \tag{2.5}$$

The definition of $\boldsymbol{q}$ and its relation to the scattering angle θ are graphically shown in Figure 2.5(b).

Until now, the nature of the scattering centers A and B was not defined. In a real sample, these are atoms α. They are characterized by an electron density distribution ρ_α

which is related to the atomic wave function. The scattering contribution of the electrons of an atom α are described by the *atomic form factor* f_α:

$$f_\alpha(\boldsymbol{q}) = \int_V d^3\boldsymbol{r}\rho_\alpha(\boldsymbol{r})e^{2\pi i(\boldsymbol{q}\cdot\boldsymbol{r})} \tag{2.6}$$

Therefore, the atomic form factor is the Fourier transform of the electron density distribution of the atom. It depends on the atomic number Z and the scattering vector. The atomic form factors are listed in the International Tables for Crystallography [45] and some examples are given in Figure 2.6.

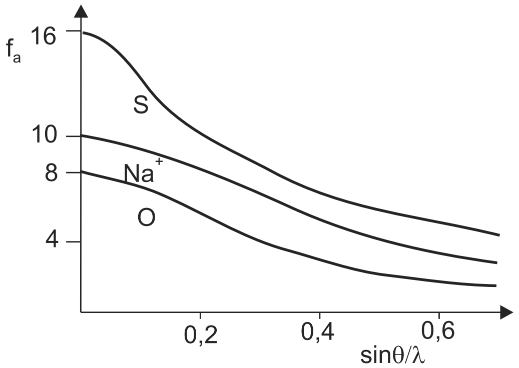

Figure 2.6: The atomic form factor of atomic sulfur, oxygen and the monovalent sodium ion as a function of the scattering vector. Taken from Ref. [43].

In a crystal, which is a period arrangement of atoms, the total scattering contribution of the unit cell is given by the *structure factor*:

$$F(\boldsymbol{q}) = \sum_{\alpha=1}^{N} f_\alpha(\boldsymbol{q})\exp[2\pi i(\boldsymbol{q}\cdot\boldsymbol{r}_\alpha)] \tag{2.7}$$

The structure factor depends on the kind and positions of all the atoms in the unit cell. It can be explicitly written for a given lattice plane with Miller indices (hkl) as:

$$F(hkl) = \sum_{\alpha=1}^{N} f_\alpha(\boldsymbol{q})\exp[2\pi i(hx_\alpha + ky_\alpha + lz_\alpha)] \tag{2.8}$$

The total scattering amplitude of a crystal is given as:

$$\frac{I}{I_0} = K\cdot L(\theta)\cdot P(\theta)\cdot|F(hkl)|^2 \tag{2.9}$$

$$= \left(\frac{e^2}{mc^2}\right)^2 \lambda^3\frac{V_{Cr}}{V_{UC}}\cdot L(\theta)\cdot\left(\frac{1+\cos^2(2\theta)}{2}\right)\cdot|F(hkl)|^2 \tag{2.10}$$

K summarizes all constants, including the volume of the crystal V_{Cr} and of the unit cell V_{UC}. $L(\theta)$ is the Lorentz factor, which depends on the diffraction geometry. It describes the ratio of the angular velocity with which the crystal is rotated to the angular velocity with which a lattice point (hkl) passes through the Ewald sphere. $P(\theta)$ is the polarization factor, which takes into account that in the case of diffraction from a transversal wave only the electric field component perpendicular to the scattering direction is active.

Laue Equation and Bragg Equation The intensity of the beam scattered from a crystal is non-zero only at specific point in space. This is due to the periodicity of the crystal. Only those reciprocal lattice vectors $\boldsymbol{q}$ lead to a non-vanishing intensity that fulfill the *Laue equations*:

$$\boldsymbol{a_1} \cdot \boldsymbol{r} = h, \;\; \boldsymbol{a_2} \cdot \boldsymbol{r} = k, \;\; \boldsymbol{a_3} \cdot \boldsymbol{r} = l \tag{2.11}$$

which can alternatively be written as

$$\boldsymbol{a_1} \cdot (\boldsymbol{s} - \boldsymbol{s_0}) = \boldsymbol{a_1} \cdot \boldsymbol{s} = h\lambda \tag{2.12}$$

$$\boldsymbol{a_2} \cdot (\boldsymbol{s} - \boldsymbol{s_0}) = \boldsymbol{a_2} \cdot \boldsymbol{s} = k\lambda \tag{2.13}$$

$$\boldsymbol{a_3} \cdot (\boldsymbol{s} - \boldsymbol{s_0}) = \boldsymbol{a_3} \cdot \boldsymbol{s} = l\lambda \tag{2.14}$$

Another interpretation of the Laue equations is given by the *Bragg equation*:

$$2 \cdot d_{hkl} \cdot \sin\theta_{hkl} = n \cdot \lambda \tag{2.15}$$

Bragg's interpretation of diffraction is based on selective reflection of the incident X-ray beam from parallel lattice planes, as shown in Figure 2.7.

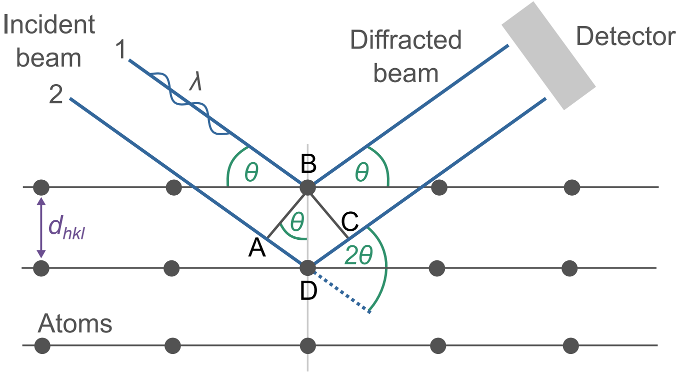

Figure 2.7: Geometric construction of Bragg's equation: Reflection of two X-ray beams from parallel lattice planes. Adapted from Ref. [43].

Two parallel beams are incident onto a sample with parallel lattice planes (hkl) with inter-planar spacing d_{hkl}. The beam that is selectively reflected from the second atomic layer has a path length to the detector that is longer than that of a beam reflected from the topmost layer. Constructive interference occurs at the detector, only if the additional path length is an integer multiple of the wavelength, i.e. the path length $\overline{ADC}$ fulfills $\overline{ADC} = n\lambda$. The Bragg equation can then be derived by considering that $\overline{ADC}$ is a function of d_{hkl} and λ.

The lattice plane spacing depends on the lattice metric of the crystal, i.e. on the lattice parameters a, b and c and the lattice angles α, β and γ. For crystals with tetragonal space group symmetry ($a = b \neq c$ and $\alpha = \beta = \gamma = 90^\circ$) it is

$$\frac{1}{d_{hkl}^2} = \frac{h^2 + k^2}{a^2} + \frac{l^2}{c^2} \tag{2.16}$$

For cubic systems ($a = b = c$) this reduces to

$$\frac{1}{d_{hkl}^2} = \frac{h^2 + k^2 + l^2}{a^2} \tag{2.17}$$

In the following, the measurement modes for the four-circle diffractometer employed in this work are briefly outlined.

2.2.2 Four-circle Diffractometer and Thin Film Characterization

Figure 2.8 shows a schematic of a four-circle diffractometer with an Eulerian cradle used for standard thin film characterization. In this work, a *Bruker* Discover D8 system is used. The first two circles are θ and ω. They lie in the scattering plane perpendicular to the sample plane. In addition, in order to map a larger volume of the reciprocal space, the sample can be rotated (φ) and tilted (χ). Furthermore, the sample can be moved linearly in x, y and z to position it in the X-ray beam.

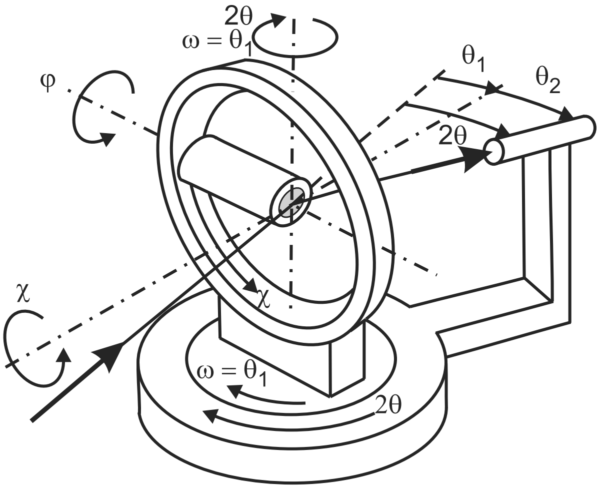

Figure 2.8: Schematic representation of a single-crystal diffractometer with four-circle geometry. Taken from Ref. [43].

In XRD measurements of epitaxial thin films a few points have to be considered that distinguish them from other single crystals. First, the volume of the film is much lower than that of the substrate and well below the penetration depth of the X-ray beam. Therefore, the overall intensity is dominated by the substrate. Secondly, there is only one lattice plane parallel to the surface. This greatly reduces the number of recorded peaks. Furthermore, because the study of epitaxial films looks at very small changes in the lattice parameters due to strain, composition etc. and because of the small differences in lattice constants between substrate and film, epitaxial thin films require a very high angular resolution of the diffractometer. Therefore, diffractometers for high-resolution XRD (HR-XRD) are equipped with additional components to generate highly collimated, monochromatic and parallel beams.

In the *Bruker* Discover D8 setup used in this work, a Göbel mirror is used on the primary beam side. The X-ray beam generated by a Cu anode is naturally divergent. A Göbel mirror is a special multilayer stack of a strong and a weak scatterer shaped in a parabolic fashion that creates a parallel and monochromatic beam. As an additional monochromator, a Ge(004) channel cut monochromator is used. The beam is repeatedly diffracted from a germanium single crystal and an aperture is used to block out the Cu-K_{α_2} radiation in order to only select the more intense Cu-K_{α_1} radiation.

θ-2θ-scans

θ-2θ-scans correspond to a coupled movement of 2θ and $\omega = \theta$. Using the Bragg equation (Equation 2.15) the lattice spacing of the planes parallel to the sample surface, also called the out-of-plane lattice spacing, can be evaluated. Under certain circumstances this allows for direct evaluation of one of the lattice parameters. For instance, for a (001)-oriented sample, for which the (001) peak is the most intense, the out-of-plane lattice parameter c can be calculated as $c = d_{001}$. The uncertainty of the calculated lattice parameter can be estimated from the measurement uncertainty of 2θ as follows:

$$\frac{\Delta c}{c} = -\Delta\theta \cot\theta \tag{2.18}$$

φ-scans

Even if a film appears epitaxial from θ-2θ-scans, it may have a random orientation of grains rotated around the z-axis of the sample. To test this, φ-scans are performed. The angles $\omega = \theta$, 2θ and χ are set to bring the sample into diffraction condition with a plane (hkl) that has a non-zero component in the hk plane. For instance, for a (001)-oriented sample, the $\{102\}$ peaks may be measured. The azimuthal angle φ is then scanned. If a (001)-oriented films grows with a perfect cube-on-cube epitaxial relationship on the substrate, the $\{102\}$ peak is measured four times, each peak corresponding to one of the symmetry-equivalent planes (102), (012), (-102) and (0-12). Thereby, φ-scans allow to probe the in-plane texture of thin films.

X-ray Reflectivity

X-ray reflectivity (XRR) is a technique to accurately quantify the film thickness as well as surface and interfacial roughness of thin film stacks. The technique is based on fundamental optics and the refraction of an X-ray beam from the sample surface is described by the Fresnel equations. A difference in the refractive index between the layers is required, which is usually present. The incidence angle α is very small, typically in the range of $\alpha = \omega < 5^\circ$. The technique can be readily performed in modern XRD setups.

Total reflection of the beam occurs below a critical angle α_c, which is related to sample properties, most importantly the density and atomic weight of the material of the topmost layer. The complex refractive index is

$$n = 1 - \sigma + i\beta \tag{2.19}$$

Herein, σ and β are the dispersion and absorption of the medium. The critical angle is directly related to the dispersion as

$$\alpha_c \approx \sqrt{2\sigma} \tag{2.20}$$

Thereby, the material density can be calculated, as it is related to the dispersion via

$$\rho \approx 2\pi \cdot \frac{M}{r_0 N_A Z \lambda} \cdot \sigma \tag{2.21}$$

Herein, M is the molar mass, r_0 the Bohr radius, N_A Avogadro's constant and Z the atomic number.

Above the critical angle, part of the X-ray beam penetrates the thin film and is reflected again at the interface of substrate and film. For more complex thin film stacks, this process occurs at each interface. Interference of the reflected beams manifests as characteristic oscillations in the recorded beam intensity. Their period allows to calculate the film thickness. By measuring the angular difference between two oscillations of order m and n the thickness can be calculated as [46]:

$$d = \frac{\lambda}{2} \cdot \frac{m - n}{\sin(\alpha_m) - \sin(\alpha_n)} \tag{2.22}$$

For complex film stacks, however, it is more convenient to use available programs for fitting the XRR spectra. In this work, the program Leptos by *Bruker* and the Python module xrayutilities [47] are used.

2.2.3 Six-circle Diffractometer

In this work, structural refinement of XRD data of antiperovskite nitride thin films is performed. The required XRD measurements are performed using a six-circle diffractometer (SIXC). Such systems are usually employed for surface X-ray diffraction studies and operate under grazing incidence [48]. The diffractometer used here is operated in the z-axis mode [49], as shown in Figure 2.9.

This setup has two detector angles γ and δ and three samples angles θ (rotation around the z-axis), ϕ and χ (tilt along and perpendicular to the beam axis). The beam is incident on the sample under $\alpha \approx 1^\circ$. The diffraction angle 2θ has to be calculated from the other angles. The sample is usually aligned and oriented in space by identifying the angles

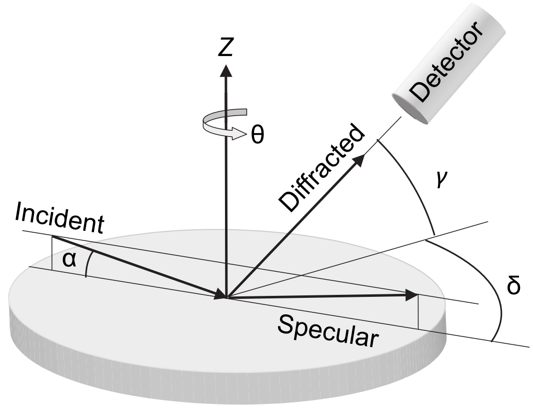

Figure 2.9: Schematic representation of a six-circle diffractometer with z-axis geometry. Taken and adapted from [50].

of two linearly independent peaks and constructing an orientation matrix. This allows to calculate the positions of every peak in reciprocal space and to record the integrated intensities of a number of peaks, which is required for the structural refinement. The refinement procedure is described in detail in Chapter 8.2 (p. 72).

The goniometer can be further equipped with a liquid helium cryostat with a beryllium dome, which is transparent for X-ray radiation. This allows for measurement in vacuum or, more importantly in this work, for temperature-dependent XRD measurements between 4 K and 500 K.

In the SIXC setup a gallium jet X-ray source is used. One important limitation of conventional X-ray Cu anodes is that the beam brilliance is limited by the melting point of the anode material. This issue can be partially circumvented by using rotating anodes. Alternatively, in liquid metal sources the electron beam is focused onto a fine metal jet of Ga or In, for instance. Metal jet sources allow for a finely focused beams with high brilliance that surpasses that of early generation synchrotron sources. Here, a Ga jet source by *Excillium* is used. A positive side effect is that the Ga K_α emission line lies at 1.3 Å, which is slightly smaller than the Cu K_α line at 1.54 Å, thereby increasing the radius of the Ewald sphere slightly. Furthermore, a Montel optics is used to create a highly collimated beam. A photograph of the SIXC setup is shown in Figure 2.10.

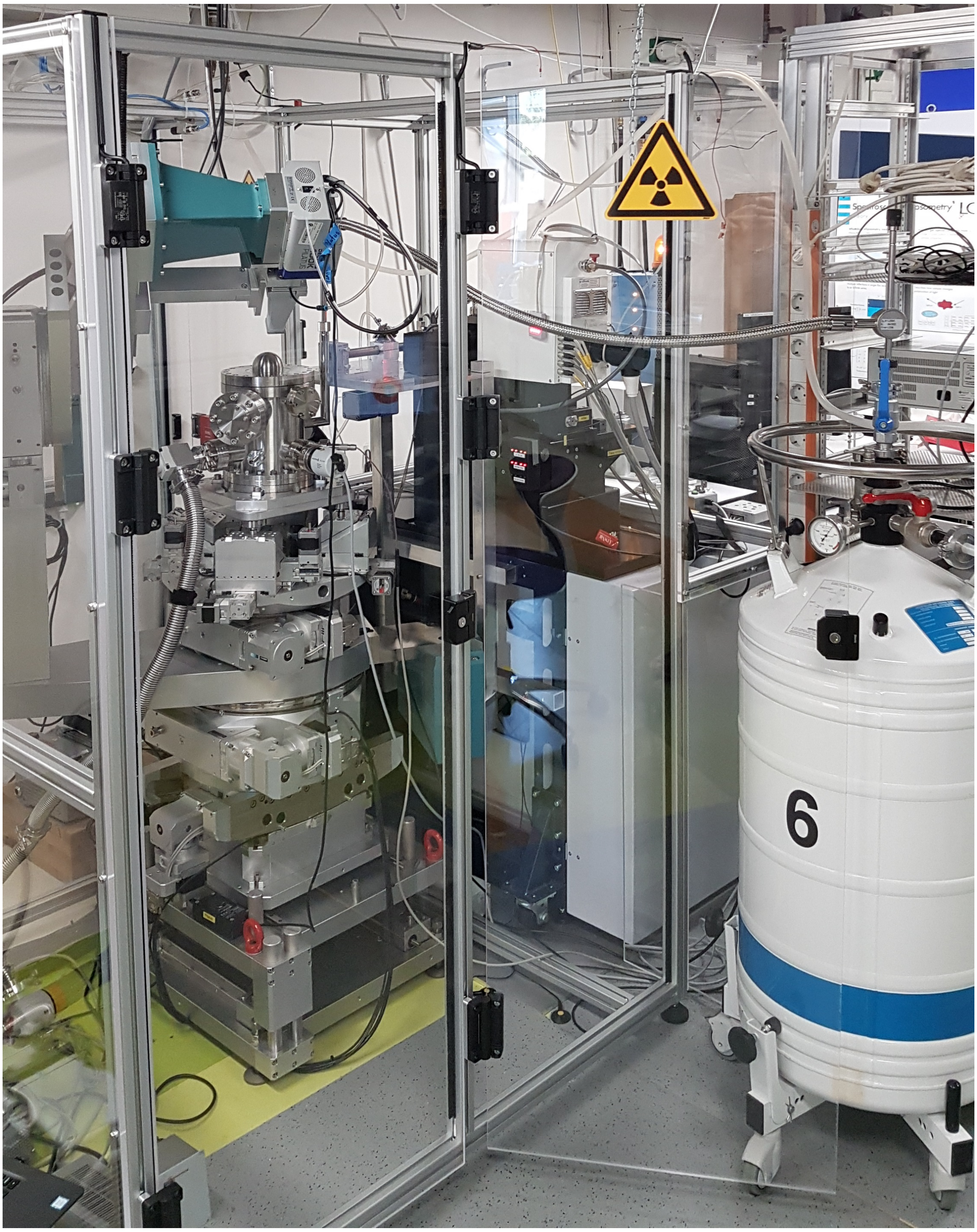

Figure 2.10: Photograph of the six-circle diffractometer used in this work, equipped with a Ga jet X-ray source and a cryostat for temperature-dependent XRD measurements.

2.3 Magnetic Characterization

2.3.1 Vibrating Sample Magnetometry

In this work, in-house magnetic characterization is performed using a Vibrating Sample Magnetometer (VSM) equipped with a Superconducting QUantum Interference Device (SQUID) for magnetic flux sensing. SQUID-VSMs allow to measure samples with very low magnetic moments due to low sample volumes (thin films) or low magnetization (non-collinear antiferromagnets).

SQUID magnetometers are based on two superconducting effects: flux quantization and Josephson tunneling [51, 52]. Superconductors are characterized by two properties. Below a critical temperature T_c, they have a vanishingly small resistivity that is at least 17 orders of magnitude below that of copper at room temperature [52]. Furthermore, they fully expel external magnetic fields from their interior, an effect is known as Meissner effect. The BCS theory by Bardeen, Cooper and Schrieffer explains superconductivity as the result of electron-phonon interaction that causes pairs of electrons to form Bosonic quasiparticles known as Cooper pairs that can travel without scattering.

If a magnetic flux passes through a ring made of a superconducting material that is then cooled below T_c, the magnetic flux is trapped in the interior of the ring. Turning of the external magnetic field causes a DC current to emerge in the ring in order to keep a constant flux in the ring. This magnetic flux Φ through the ring is quantized:

$$\Phi = \frac{2\pi\hbar}{2e} s = \Phi_0 s \tag{2.23}$$

Herein, s is an integer and Φ_0 is the flux quantum $\Phi_0 \approx 2.0678 \times 10^{-15}\,\mathrm{Tm}^2$.

If an insulating barrier is inserted into the ring, a Josephson junction is formed, through which the Cooper pairs can tunnel. In such a Josephson junction, a DC current flows through the junction without an applied electric or magnetic field. The current depends on the phase δ of the Cooper pair wave function in the two superconducting regions: $J = J_0 \sin\delta$. If an additional DC voltage is applied to the junction, an AC current flows through the junction:

$$J = J_0 \sin\left[\delta(0) - \frac{2eV}{\hbar} t\right] \, . \tag{2.24}$$

Most importantly, the oscillation frequency depends on the applied voltage as:

$$\omega = \frac{2eV}{\hbar} \, . \tag{2.25}$$

SQUIDs are based on the macroscopic quantum interference effect that results from flux quantization in superconducting ring with one more (usually two) Josephson junctions, as shown in Figure 2.11(a). The currents passing through the Josephson junctions J_a and J_b interfere, which leads to an oscillating total current through the junction:

$$J_{tot} = 2J_0 \sin\delta_0 \cos\left(\frac{e}{hc}\Phi\right) \, . \tag{2.26}$$

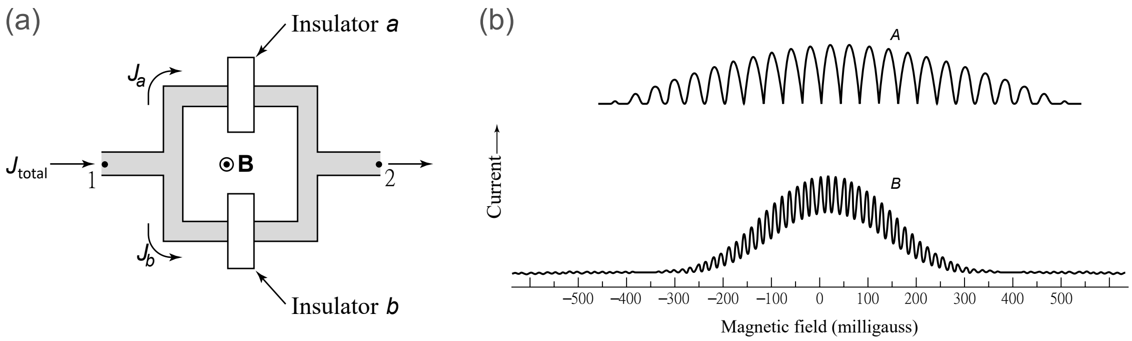
(a)
Insulator a
J_a
J_{total}
1
B
2
J_b
Insulator b
(b)
A
B
Current
−500
−400
−300
−200
−100
0
100
200
300
400
500
Magnetic field (milligauss)

Figure 2.11: (a) Schematic of a SQUID consisting of a superconducting ring with two Josephson junctions. (b) Macroscopic quantum interference in such a SQUID. Taken from Ref. [53].

Most modern SQUID magnetometers use DC-SQUIDs, meaning that the applied current is a DC current. It can be seen that J_{tot} directly depends on the magnetic flux Φ passing through the ring. This oscillatory behavior is shown in Figure 2.11(b). Therefore, the voltage over the SQUID varies periodically with the frequency being proportional to the flux quantum Φ_0, as shown in Figure 2.12(b). This allows for very accurate measurement of the magnetic flux. Using a feedback loop, the SQUID can be locked at a certain point in the V-Φ_0 characteristic and the feedback current is then a measure for the external flux.

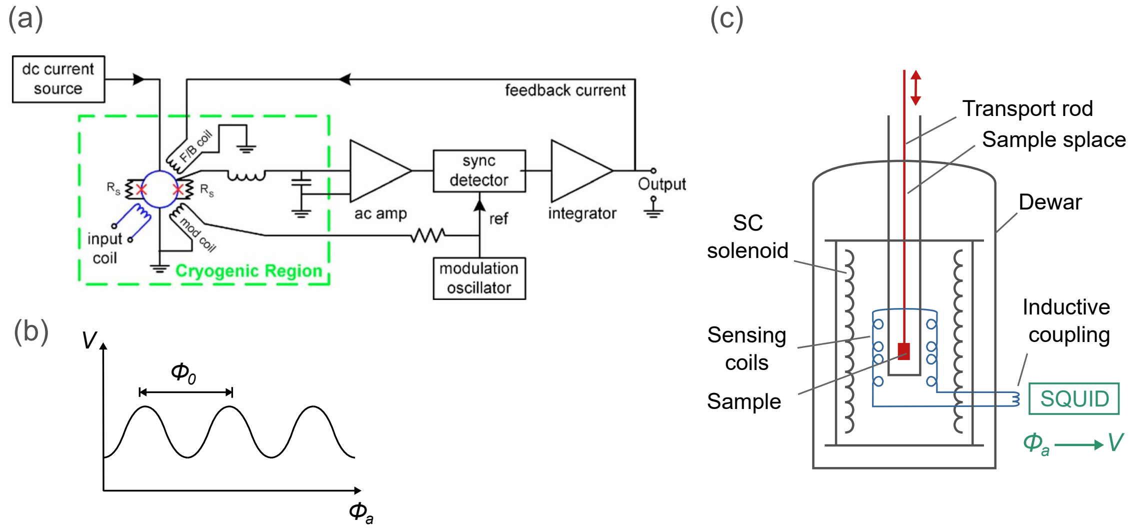
(a)
dc current source
feedback current
F/B coil
R_s
R_s
input coil
mod coil
Cryogenic Region
ac amp
sync detector
ref
integrator
Output
modulation oscillator
(b)
V
Φ_0
Φ_a
(c)
Transport rod
Sample splace
Dewar
SC solenoid
Sensing coils
Sample
Inductive coupling
SQUID
$\Phi_a \longrightarrow V$

Figure 2.12: Components of a SQUID-VSM: (a) Block diagram of the circuit of a DC-SQUID. (b) Oscillating voltage signal due to quantum interference in a SQUID. (c) Schematic of a VSM equipped with a SQUID. Figures taken from Refs. [52], [51] and [41].

Figure 2.12(a) shows a block diagram of a typical DC-SQUID [52] (more details can be found in Ref. [51]). The SQUID is inductively coupled to a set of sensing coils (arranged to form a gradiometer) that pick up the magnetic flux gradient around the sample in the chamber volume, as shown in Figure 2.12(c). The vibrating motion of the magnetic sample through the sensing coils generates a change in flux density, which generates a voltage in the coils, which is transmitted to the SQUID. In the MPMS3 system by *Quantum Design* used in this work, an external magnetic field up to 7 T generated by superconducting coils is applied to the sample. Different sample holders are used, as discussed in Chapter 6.3.1.

2.3.2 X-ray Magnetic Circular Dichroism

X-ray magnetic circular dichroism (XMCD) is a synchrotron technique to measure spin and orbital magnetization and can be used complementary to lab-based techniques such as SQUID-VSM [54, 55].

XMCD is a variant of X-ray absorption spectroscopy (XAS) that analyzes the integral of the unoccupied density of states versus energy. In XAS, core-level electrons are excited into unoccupied states above the Fermi level by incident X-rays. In the compound investigated in this work, Mn_3SnN, the Mn $L_{2,3}$ absorption edge at around 645 eV is probed. The intensity of an X-ray with energy $E = h\nu$ as a function of penetration depth x in a sample is described by the Lambert-Beer law [54]:

$$I(E,x) = I_0(E) \cdot e^{-\mu(E)\cdot x} \tag{2.27}$$

Herein, μ is the photoabsorption coefficient. In the energy range investigated here the photoeffect is the dominating photon-electron interaction. μ is proportional to the absorption cross section σ_{abs} that is given by the transition probability per unit time P_{fi} and the photon flux I_{ph}:

$$\mu \propto \sigma_{\text{abs}} = \frac{P_{\text{fi}}}{I_{\text{ph}}} \tag{2.28}$$

P_{fi} is given by Fermi's Golden Rule:

$$P_{\text{fi}} \propto \sum_{f,i} M_{\text{fi}}^2 \cdot [1 - n(E_f)] \cdot \delta[h\nu - (E_f - E_i)] \tag{2.29}$$

M_{fi}^2 is the transition matrix element, $1 - n(E_f)$ is the density of unoccupied states and the δ-function reflects the energy conservation during absorption. Within the electric dipole approximation, only certain transitions are allowed according to a set of selection rules that concern the differences between the spin and magnetic quantum numbers of the initial and the final state:

$$\Delta m_s = 0,\ \Delta m_l = \pm 1 \tag{2.30}$$

The aforementioned $L_{2,3}$ absorption edges correspond to transitions from $2p$ states to $3d$ states. Because XAS is based on atomic transitions, XMCD is an element-specific technique to measure magnetic moments. In the case of Mn_3SnN only the magnetism at the Mn sites is probed.

In this work, the spectra are recorded in total electron yield mode. The holes left behind by the excited $2p$ electrons are reoccupied by electrons from energetically higher states. This process is accompanied by the emission of either a photon or an Auger electron. Only those Auger and secondary electrons with high enough energy can leave the sample. Therefore, this technique is very surface sensitive and probes only the topmost few nanometers of the sample. The emission current, which is a measure for the absorption coefficient, is measured by grounding the sample and measuring the drain current to the ground.

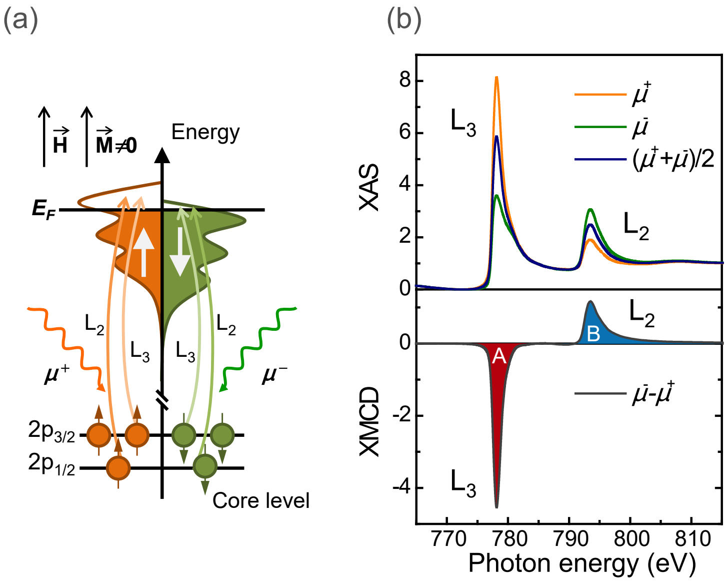

Figure 2.13: (a) The two-step absorption process in X-ray circular magnetic dichroism (XMCD) and (b) exemplary X-ray absorption and XMCD spectra at the Co $L_{2,3}$ edge. Taken from Ref. [55].

In XMCD the incident X-ray photon is circularly polarized. In magnetic materials the spin distribution is anisotropic and the electronic bands are spin-split. As a result, the X-ray absorption process is polarization-dependent, an effect known as dichroism. X-ray *magnetic* circular dichroism can be distinguished from X-ray *natural* circular dichroism that can occur in materials with anisotropic charge distribution lacking a center of inversion.

The absorption process in XMCD is described as a two-step process. First, the transition probability from $2p$ states is considered and, secondly, the polarization of the unoccupied $3d$ final states is probed. Figure 2.13(a) shows the density of states diagram of a typical $3d$ system. The $2p$ core levels are spin-orbit split, i.e. the $2p_{1/2}$ ($J = 1/2$) and $2p_{3/2}$ ($J = 3/2$) have different energy. Furthermore, the $3d$ bands at the Fermi level are spin-split.

The transition probabilities of the different possible transition are given by the Clebsch-Gordon coefficients. For a given helicity of the X-ray photon, the orbital polarization of electrons excited from $2p_{1/2}$ and $2p_{3/2}$ states is the same. In contrast, the spin polarization of the excited electrons is found by summing up all the possible transition weighted by their probabilities. Thereby, it is found that for $2p_{3/2}$ transitions, 62.5 % of the electrons carry a spin $m_s = +1/2$ and only 37.5 % carry a spin $m_s = -1/2$. For $2p_{1/2}$ transitions the respective probabilities are 25 % and 75 % [54]. Therefore, the sign of the spin polarization is opposite for the two different $2p$ transitions.

In a second step, the orbital and spin polarization of the excited electrons probe the polarization of the unoccupied final states. Any imbalance in either spin or orbital magnetization in the final states gives rise to a dichroic effect. In the case of $3d$ metals, this effect is usually dominated by the spin-split bands. Consider again the case shown in Figure 2.13(a). As discussed above, for a positive helicity of the incident X-rays, $2p_{3/2}$ states with $m_s = +1/2$ have a higher excitation probability than those with $m_s = -1/2$. In addition, the density of unoccupied spin-up states is much higher than that of spin-down states. In contrast, if the helicity is negative or, equivalently, if the magnetization is reversed, the much lower density of unoccupied spin-down states is probed.

Therefore, the absorption spectrum at the L_3 edge, shown in Figure 2.13(b) for the case of Co [55], is larger in the case of a positive helicity. The opposite is true of the L_2 edge, because the spin-down electrons have a much higher transition probability from $2p_{1/2}$ initial states, as discussed above. The difference between spectra taken at positive and negative polarization (or at opposite magnetization) is known as the XMCD spectrum, also shown in Figure 2.13(b).

Electrons excited from $2p_{3/2}$ and $2p_{1/2}$ states have a different sign of spin polarization but the same sign of orbital polarization. This allows to distinguish spin and orbital contributions by applying the so-called sum rules [54]. The orbital magnetic moment μ_l and the effective spin magnetic moments μ_s^{eff} per unoccupied final state n_h are given as:

$$\frac{\mu_l}{n_h} = -\frac{2}{3}\frac{q}{r} \cdot \mu_\mathrm{B} \tag{2.31}$$

$$\frac{\mu_s^{\text{eff}}}{n_h} = \frac{2q - 3p}{r} \cdot \mu_\mathrm{B} \tag{2.32}$$

μ_B is the Bohr magneton and p, q and r are given as:

$$p = \int_{L_3} (\mu_+ - \mu_-) dE \tag{2.33}$$

$$q = \int_{L_3+L_2} (\mu_+ - \mu_-) dE \tag{2.34}$$

$$r = \frac{1}{2} \int_{L_3+L_2} (\mu_+ + \mu_-) dE \tag{2.35}$$

Thereby, sum rule analysis allows for quantification of spin and orbital magnetization by integration of the difference and sum spectra of the X-ray absorption spectra taken at opposite helicity or magnetization direction.

Chapter 3

The Anomalous Hall Effect: Theory and Measurement

3.1 Semi-classical Transport Theory

The response of electrons in a solid to an applied electric field is one of the oldest problems in solid state physics [53, 56]. Electrons moving in a ferromagnet have a velocity component perpendicular to electric field and magnetization. A theory for this anomalous velocity was established by Karplus and Luttinger [57]. Berry realized that an electron moving in the Brillouin zone (BZ) acquires a geometric phase, later named after him as Berry phase [58]. The anomalous velocity term is proportional to the cross product of electric field $\boldsymbol{E}$ and the Berry curvature Ω_n, which is the local gauge field of the Berry phase. The velocity $\boldsymbol{v}_n$ of electrons in a Bloch band with index n and wave vector $\boldsymbol{k}$ is then [14, 59]:

$$\boldsymbol{v}_n(\boldsymbol{k}) = \frac{1}{\hbar}\frac{\partial \varepsilon(\boldsymbol{k})}{\partial \boldsymbol{k}} - \frac{e}{\hbar}\boldsymbol{E} \times \Omega_n(\boldsymbol{k}) \tag{3.1}$$

Herein, $\hbar$ is the reduced Planck constant, e the electron charge and ε is energy. The Berry curvature is an intrinsic property of electrons in the solid forming bands with periodic Bloch wave functions $\psi_{n\boldsymbol{k}}$:

$$\Omega_n(\boldsymbol{k}) = i\langle \nabla_{\boldsymbol{k}} \psi_{n\boldsymbol{k}} | \times | \nabla_{\boldsymbol{k}} \psi_{n\boldsymbol{k}} \rangle \tag{3.2}$$

This semi-classical formalism is in agreement with the Kubo formalism, which is a general linear response theory to compute response tensors to external perturbations. Thereby, an equivalent equation for the Berry curvature can be found using the Kubo formalism [14, 59] as (α, β are Cartesian coordinates):

$$\Omega_{n,\alpha\beta}(\boldsymbol{k}) = -2\hbar^2 \,\mathrm{Im} \sum_{m \neq n} \frac{\langle \psi_{n\boldsymbol{k}} | \hat{v}_\alpha | \psi_{m\boldsymbol{k}} \rangle \langle \psi_{m\boldsymbol{k}} | \hat{v}_\beta | \psi_{n\boldsymbol{k}} \rangle}{[\varepsilon_n(\boldsymbol{k}) - \varepsilon_m(\boldsymbol{k})]^2} \tag{3.3}$$

Berry curvature, therefore, is the origin of the intrinsic contribution of the bands to the anomalous Hall effect (AHE), which describes the occurrence of a charge current $\boldsymbol{j}_\alpha$

in response to an electric field $\boldsymbol{E}_\beta$ [15]. The 3×3 matrix relating the two quantities is the AHC tensor $\sigma_{\alpha\beta}$, which satisfies $\boldsymbol{j}_\alpha = \sigma_{\alpha\beta}\boldsymbol{E}_\beta$. It is related to the Berry curvature as:

$$\sigma_{\alpha\beta} = -\frac{e^2}{\hbar}\sum_n \int_{BZ} \frac{d^3\boldsymbol{k}}{(2\pi)^3} f_n(\boldsymbol{k})\Omega_{n,\alpha\beta}(\boldsymbol{k}) \tag{3.4}$$

Therefore, the AHC is proportional to the integral of the Berry curvature over the Brillouin zone (BZ), weighed by the Fermi distribution function f_n summed over all occupied bands n.

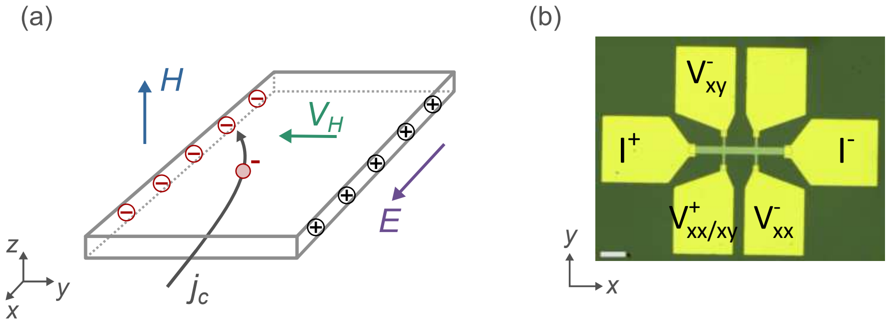

Figure 3.1: (a) Schematic representation of the intrinsic anomalous Hall effect. A non-zero total Berry curvature leads to a Hall voltage V_H perpendicular to an applied electric field E. A magnetic field H is applied out-of-plane. (b) Optical image of a double Hall bar device employed for Hall effect measurements (the scale bar is 50 µm).

A sketch of the AHE and an optical image of a Hall bar device used for Hall effect measurements are shown in Figure 3.1. An electric field and a magnetic field are applied in x-direction and z-direction, respectively, and the Hall voltage is measured along y. This measurement configuration is sensitive to the $\sigma_{yx} = -\sigma_{xy}$ component of the AHC tensor. Double Hall cross devices such as the one shown here allow for simultaneous measurement of the longitudinal (V_{xx}) and transverse (V_{xy}) voltages.

Historically, the AHE was thought to require a net magnetization of the sample and was, therefore, associated with ferromagnets. In contrast, in collinear antiferromagnets (AFs), although magnetic order is present, the anomalous Hall contributions of the two opposing sublattices exactly cancel. As shown in the next section, the AHE is also observed in certain AFs with non-collinear antiferromagnetic (NCAF) order. Semi-classical transport theory shows that the AHE is not, in fact, due to magnetization but due to Berry curvature. Berry curvature and magnetization behave similarly under symmetry transformations like rotation, inversion and time reversal. $\boldsymbol{\Omega}_n$ is also a pseudo-vector and transforms under a time reversal symmetry operation $\hat{T}$ as $\boldsymbol{\Omega}_n(-\boldsymbol{k}) = -\boldsymbol{\Omega}_n(\boldsymbol{k})$. As such, Berry curvature is often considered as a fictitious magnetic field in k-space.

3.2 Anomalous Hall Effect in Cubic Non-collinear Antiferromagnets

The symmetries present in a given material determine which tensor components of the AHC tensor are zero or interdependent. Here, the case of cubic antiperovskites with non-collinear antiferromagnetic structures is considered. As elucidated further in Chapter 4.2.2 (p. 33), these materials host triangular magnetic spin textures characterized by different in-Kagome-plane spin angles. Two irreducible representations can be distinguished, which are denoted Γ^{5g} and Γ^{4g} and which correspond to the magnetic space groups (SGR) $R\bar{3}m$ and $R\bar{3}m'$. Graphical representations of the corresponding spin textures are shown in Figure 3.2. For the shape of the AHC tensors, however, only the magnetic Laue groups (LGR) have to be considered. The magnetic LGR are $\bar{3}1m$ (Γ^{5g}) and $\bar{3}1m'$ (Γ^{4g}). The symmetry-imposed shapes of the AHC tensors (the odd part of the charge conductivity tensor) can be found from Ref. [60]. Tab 3.1 shows the AHC tensors in the Γ^{5g} and Γ^{4g} configuration.

Table 3.1: Anomalous Hall conductivity tensors in the Γ^{5g} and Γ^{4g} spin configurations in two different coordinate systems, corresponding to samples grown with (111)- and (001)-orientation [60,61].

IRep	PGR	$\sigma^{(111)}$	$\sigma^{(001)}$
Γ^{5g}	$\bar{3}1m$	$\begin{pmatrix} 0 & 0 & 0 \\ 0 & 0 & 0 \\ 0 & 0 & 0 \end{pmatrix}$	$\begin{pmatrix} 0 & 0 & 0 \\ 0 & 0 & 0 \\ 0 & 0 & 0 \end{pmatrix}$
Γ^{4g}	$\bar{3}1m'$	$\begin{pmatrix} 0 & \sigma_{xy} & 0 \\ -\sigma_{xy} & 0 & 0 \\ 0 & 0 & 0 \end{pmatrix}$	$\begin{pmatrix} 0 & \sigma'_{xy} & -\sigma'_{xy} \\ -\sigma'_{xy} & 0 & \sigma'_{xy} \\ \sigma'_{xy} & -\sigma'_{xy} & 0 \end{pmatrix}$

In the left column, the three-fold symmetry axis $\bar{3}$ is parallel to the z-axis. This coordinate system exactly corresponds to a thin film sample grown with (111)-orientation. Axis transformation to a coordinate system in which $\bar{3}$ is along the [111] axis (in Cartesian coordinates) yields $\sigma^{(001)}$ (right column), which corresponds to a (001)-oriented thin film sample.

It is found that no AHE is allowed by symmetry in the Γ^{5g} case, while it is allowed in both growth orientations in the Γ^{4g} case. Marked in red are the tensor components that are measured in the measurement configuration shown in Figure 3.1(b). A non-zero AHC is expected when the charge current has a component within the (111) Kagome plane and is at a maximum, when it is exactly within the Kagome plane. This is in contrast to the hexagonal Mn_3Sn, in which the AHC vanishes if the current is in the (0001) Kagome plane and an out-of-plane AHE current can only be generated by an in-plane field [29]. The symmetry of $\sigma_{\alpha\beta}$ is determined by the symmetry of the Berry curvature (Equation 3.4). $\boldsymbol{\Omega}_n$ is odd under time reversal: $\boldsymbol{\Omega}_n(-\boldsymbol{k}) = -\boldsymbol{\Omega}_n(\boldsymbol{k})$. Therefore, the integral of the Berry curvature over the Brillouin zone and, thereby, $\sigma_{\alpha\beta}$ are zero in the presence of time reversal symmetry, which is the case non-magnetic materials. Similarly, the total Berry curvature also vanishes, if there is a symmetry operation $\hat{A}$ that transforms $\boldsymbol{k}$ as $\boldsymbol{k}' = \hat{A}\boldsymbol{k}$ such that $\hat{A}\boldsymbol{\Omega}_n(\boldsymbol{k}) = -\boldsymbol{\Omega}_n(\boldsymbol{k})$.

As shown in Figure 3.2, although the Γ^{5g} configuration breaks time reversal symmetry $\hat{T}$, there are $\hat{M}$ mirror symmetries perpendicular to $[\bar{1}10]$-type axes. Under these $\hat{M}$

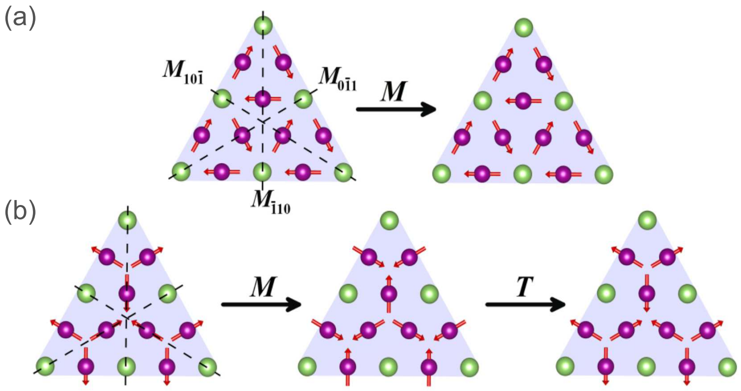

Figure 3.2: The effect of mirror and time reversal symmetry operations on the non-collinear spin textures corresponding to the (a) Γ^{5g} and (b) Γ^{4g} configuration. Taken from Ref. [61].

operations, the original magnetic structure is preserved, because spin is a pseudo-vector. Therefore, the AHC vanishes. Symmetry operations restricting the Berry curvature are tabulated in Ref. [62]. The case is different in the Γ^{4g} configuration (magnetic LGR $\bar{3}1m'$), which breaks $\hat{M}$ symmetry by reversing all spins. In contrast, the combined $\hat{M}\hat{T}$ symmetry operation preserves the original structure. This makes $\mathbf{\Omega}_n$ an even function of $\boldsymbol{k}$. Thereby, the integral over the Brillouin zone in Equation 3.4 and, therefore, the AHC can be non-zero [61].

The device fabrication of actual Hall bar devices is described in Chapter 7.1. Experimental evidence for the AHE in NCAFs is discussed further in Chapter 10.3. The next part of this work discusses a group of materials that host such NCAF textures in more detail, namely Mn-based nitrides with an antiperovskite crystal structure.

Part II

Identification of Promising Antiperovskite Nitrides

Chapter 4

Mn-based Antiperovskite Nitrides

4.1 Chemistry and Crystal Structure

Perovskites are frequently encountered in spintronics, not only because many of the oxides used as thin film substrates such as $SrTiO_3$ are perovskites, but also because many transition metal oxides with interesting and technologically relevant properties crystallize in this structure [63–65]. A less common structure that can be derived from the perovskite structure is the inverse perovskite or antiperovskite structure, which can be found in ternary compounds such as transition metal carbides, nitrides or fluorides with generic formula X_3AB. In antiperovskites the X site is occupied by cations and the A and B sites are occupied by anions. X are typically alkaline, earth-alkaline or transition metal elements, A are typically (post-)transition metals or metalloids and B are reactive non-metals. As can be seen from Figure 4.1, a large portion of the periodic table can be hosted in the antiperovskite structure, resulting in a plethora of interesting properties and potential applications [13, 66].

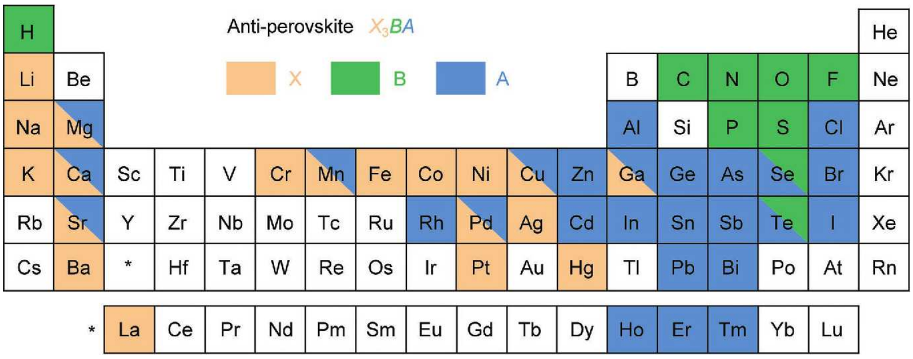
Anti-perovskite X_3BA
X
B
A
H He
Li Be B C N O F Ne
Na Mg Al Si P S Cl Ar
K Ca Sc Ti V Cr Mn Fe Co Ni Cu Zn Ga Ge As Se Br Kr
Rb Sr Y Zr Nb Mo Tc Ru Rh Pd Ag Cd In Sn Sb Te I Xe
Cs Ba * Hf Ta W Re Os Ir Pt Au Hg Tl Pb Bi Po At Rn
* La Ce Pr Nd Pm Sm Eu Gd Tb Dy Ho Er Tm Yb Lu

Figure 4.1: Periodic table of elements showcasing the elements which form compounds with antiperovskite structures. Taken and adapted from Ref. [13].

An antiperovskite crystal can be viewed as a 3D network of corner sharing BX_6 octahedra, where B occupies the interstitial sites, as shown in Figure 4.2(a). This picture is commonly applied to understand the magnetic properties of oxide perovskites, wherein the magnetic exchange is dominated by indirect exchange interaction of transition metal cations inside the octahedra, mediated by the oxygen ions (B-O-B exchange) [68]. While

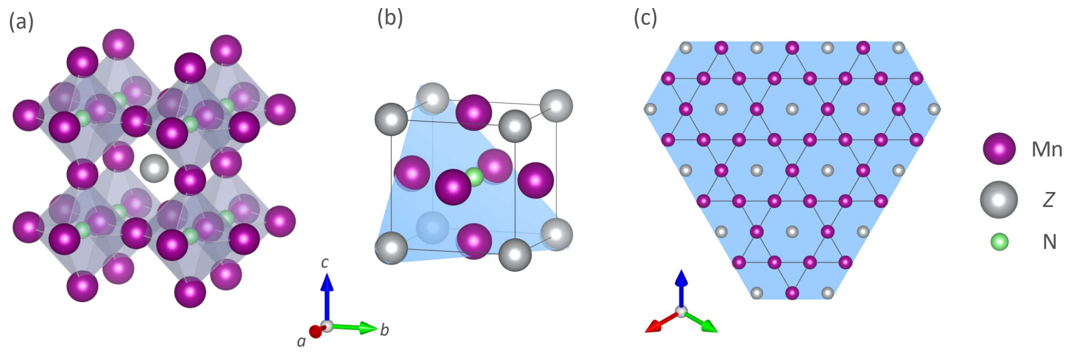

Figure 4.2: Crystal structure representations of cubic Mn-based antiperovskites. (a) 3D network of corner-sharing Mn_6N octahedra. (b) Single unit cell of Mn_3ZN with (111) plane shaded in blue. (c) Extended view of the (111) plane showing the Kagome lattice formed by the Mn atoms. Made with VESTA 3 [67].

this exchange mechanism is also active in Mn-based antiperovskites, an important difference is that the magnetic Mn atoms occupy the octahedron corners and it can be assumed that direct Mn-Mn exchange is much stronger due to increased orbital overlap.

The structure can also be viewed as being related to the Cu_3Au-type structure, with the octahedral vacancies fully occupied by B. This picture alludes to similarities between the crystal and magnetic structures of some Mn-based antiperovskites to Mn-based compounds with a Cu_3Au-type structure such as Mn_3Ir and Mn_3Pt that show non-collinear antiferromagnetic (NCAF) spin textures. It also stresses the importance of geometric frustration of magnetic moments caused by the triangular arrangement of Mn atoms in the Kagome lattices in the (111) planes. Figure 4.2(b) shows a single unit cell of a Mn-based transition metal antiperovskite nitride Mn_3ZN with the (111) plane shaded in blue. Figure 4.2(c) shows an extended view of the (111) plane showing the Kagome pattern. Materials with this kind of lattice are known to host interesting physical phenomena such as quantum spin liquid states [69, 70] and NCAF order, as discussed in this work.

Some compounds deviate from the ideal cubic structure. In these cases, the notation of Fruchart and Bertaut is used to refer to tetragonally contracted or elongated antiperovskite structures as T_1^- and T_1^+ [71, 72]. A tetragonal superlattice structure comprising of four perovskite blocks comparable to the U_3Si-type structure is denoted T_4. The different crystal structures and symmetries are summarized in Table 4.1.

Table 4.1: Labeling of crystallographic structures found in Mn-based antiperovskites following the notation of Fruchart and Bertaut [72]. The corresponding space groups (SGR) are given in Hermann-Mauguin (HM) and Schoenflies notation.

Abbr.	Crystal system	Space Group Symmetry			Lattice parameters
		SGR	HM	Schoenflies	
C	cubic	221	$Pm\bar{3}m$	O_h^1	
T_1^+	tetragonal	123	$P4/mmm$	D_{4h}^1	$c > a$
T_1^-	tetragonal	123	$P4/mmm$	D_{4h}^1	$c < a$
T_4	tetragonal	140	$I4/mcm$	D_{4h}^{18}	

4.2 Magnetism

4.2.1 Overview

Mn-based antiperovskite nitrides exhibit rich magnetic phase diagrams and can host a plethora of collinear and non-collinear magnetic structures that render them interesting for spintronic applications. Pioneering work on the crystallographic and magnetic phases of antiperovskite nitrides was done by Fruchart, Bertaut *et al.* in the 1960s and 1970s, which laid the foundation for subsequent work over the following decades [12, 71–103]. Figure 4.3 shows the crystallographic and magnetic phases of some Mn_3ZN compounds and graphical representations of these compounds are presented in Figure 4.4 (the numbering of the types of magnetic order follows the appearance in the text).

This chapter focuses on the role of the Z site atoms in antiperovskite nitrides, although substitution of N by C also impacts the properties of the compounds [12, 72, 91].

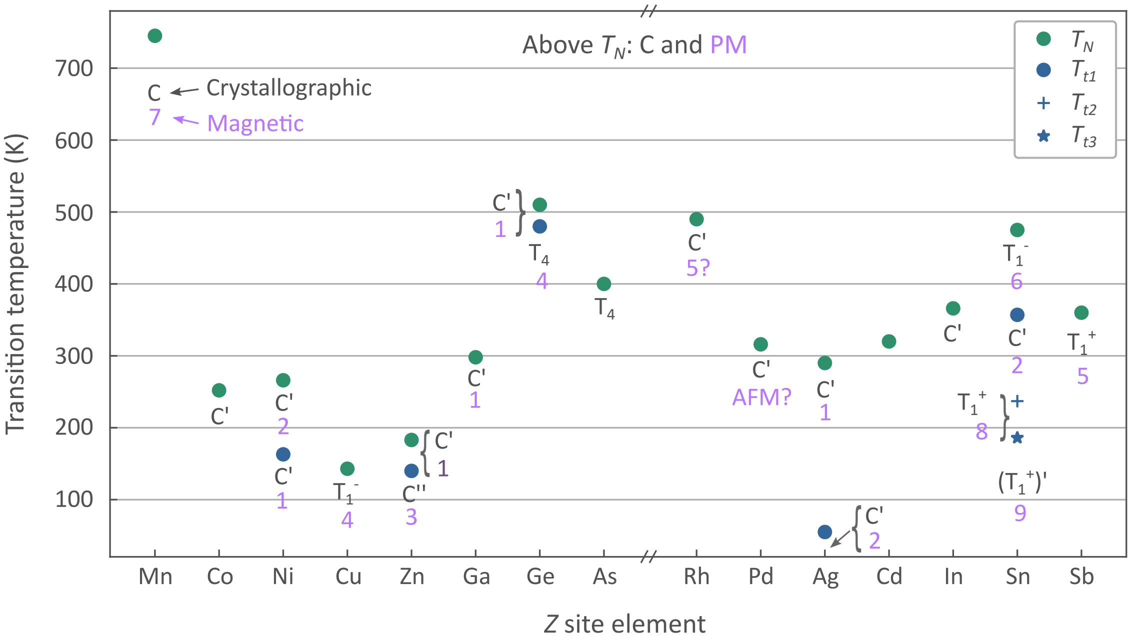

Figure 4.3: Crystallographic and magnetic phases with corresponding phase transition temperatures of antiperovskite nitrides with different Z-site elements. Crystallographic phases are labeled in gray following the notation in Table 4.1. Magnetic phases (graphical representations are shown in Figure 4.4) shown in magenta. Values taken or read out from Refs. [12, 71–103].

4.2.2 Triangular Magnetic Structures

In Mn_3ZN (Z = Ni, Zn, Ga, Ag, Sn) frustration of magnetic moments on the Kagome lattice causes non-collinear, triangular magnetic ordering, in which the spins lie in the (111) plane at an angle of 120° with respect to each other, as shown in Figure 4.4. In this phase, the crystal has cubic SGR symmetry $Pm\bar{3}m$ (labeled with C in Figure 4.3). Group theoretical analysis shows that with cubic symmetry and wave vector $\vec{k} = [000]$ three irreducible representations of the magnetic SGR are allowed [72]. The two irreducible representations that correspond to the NCAF spin textures are denoted Γ^{5g} and

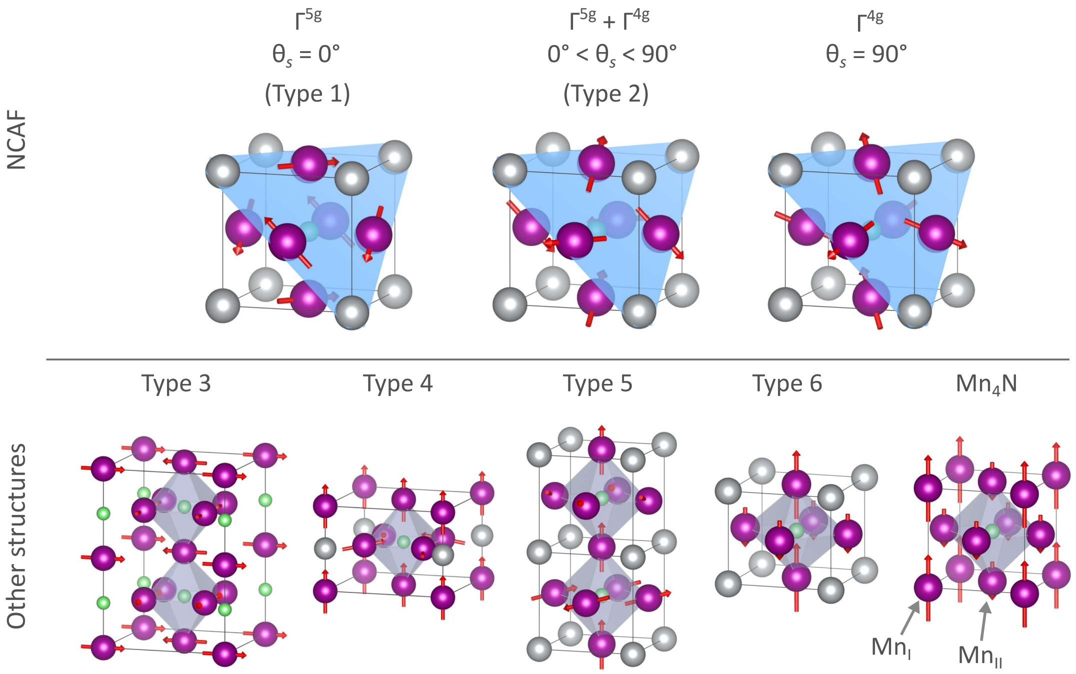

Figure 4.4: Schematic representations of some crystal and magnetic structures found in Mn-based antiperovskite nitrides.

Γ^{4g}, following Fruchart and Bertaut. The Γ^{4g} irreducible representation also allows for ferromagnetic ordering. The NCAF Γ^{5g} and Γ^{4g} spin textures differ in the angle at which the magnetic moments lie in the (111) plane with respect to the crystallographic axes. The in-plane spin angle, θ_s, is 0° with respect to the [1-10] direction for the Γ^{5g} and 90° for the Γ^{4g} configuration. The magnetic SGR are $R\bar{3}m$ (Γ^{5g}) and $R\bar{3}m'$ (Γ^{4g}). With the exception of Mn_3SnN, which is discussed below, the triangular spin textures are formed in the highest temperature magnetic phase below the Néel temperature T_N. The magnetic phase transitions are accompanied by 1st order cubic-to-cubic phase transition with strong lattice expansion with decreasing temperature at T_N.

In the following, a few notable antiperovskites with triangular non-collinear spin textures are discussed in further detail.

Mn_3ZnN [82] and **Mn_3GaN** [79] show stable Γ^{5g} configuration in certain temperature windows, denoted here as type 1 ordering. According to Fruchart *et al.*, Mn_3ZnN transitions to a type 3 multi-sublattice collinear AF order at lower temperatures. However, Sun *et al.* recently found a collinear ferrimagnetic structure [97].

In **Mn_3NiN**, **Mn_3AgN** and **Mn_3SnN** Fruchart *et al.* find spin rotational phases (type 2 ordering), in which the triangular structure gradually rotates within the (111) plane from one irreducible representation to the other as a function of temperature. The evolution of the Γ^{4g} configuration is typically accompanied by a gradual development of a symmetry-allowed weak moment in the [111] direction. A pure Γ^{4g} phase in a wide temperature range is not found in any of these compounds.

In **Mn_3NiN** the rotation is from Γ^{4g} to Γ^{5g} with decreasing temperature. At lower temperatures, the structure remains in the Γ^{5g} configuration. However, reports differ in the details of the spin rotation in Mn_3NiN. Fruchart *et al.* [83] report full rotation by 90° from Γ^{4g} at $T_N = 266\,K$ to Γ^{5g} at 163 K, below which it remains in Γ^{5g} (these values are plotted in Figure 4.3). In contrast, Wu *et al.* [99] find a rotation from Γ^{4g} at $T_N = 260\,K$ by 50° towards Γ^{5g} configuration. The structure remains in the type 2 ordered phase and θ_s reaches its minimum of about 40° at 120 K. Boldrin *et al.* [101] report yet another temperature-dependent rotation. At $T_N = 262\,K$ they find $\theta_s = 45°$ and rotation to Γ^{5g} ($\theta_s = 0°$), which is reached at 220 K. These discrepancies may be explained by differences in the sample preparation, thus potentially hinting at the sensitivity of the magnetic structure of Mn_3NiN on the exact composition.

In **Mn_3AgN** a similar spin-rotational phase is found [90]. Interestingly, the sense of spin rotation as a function of temperature is opposite to that of Mn_3NiN and Mn_3SnN. Mn_3AgN transitions from PM to the Γ^{5g} configuration at $T_N = 290\,K$ and starts rotating towards Γ^{4g} at 55 K. The rotation is accompanied by the evolution of a relatively large magnetic moment per Mn atom along [111] of $\approx 0.3\,\mu_B$/Mn at 4.2 K. In comparison, the weak moments of Mn_3NiN and Mn_3SnN are in the order of $1\,m\mu_B$/Mn.

Following the experimental discovery of spin rotation in Mn_3NiN, Bertaut and Fruchart studied the phenomenon theoretically [86] and concluded that an additional anisotropy arises from anisotropic exchange interaction in this material. Gomonaj and L'Vov elaborated on the spin rotation in Mn_3AgN in two phenomenological studies [104, 105] and agree that the low weak moment in Mn_3ZN (Z = Ni, Sn) can indeed be explained by the presence of Dzyaloshinskii-Moriya interaction. For Mn_3AgN, however, they argue that the spin-rotational phase transition is of different nature. It is not governed by temperature-dependent anisotropy constants but by a sign change of the exchange parameter itself. The type 2 phase in Mn_3AgN may, therefore, be considered a non-collinear ferrimagnetic phase with moment along [111]. This is also in agreement with field-dependent magnetization data at low temperatures [90]. It has been speculated based on magnetization measurements that Mn_3IrN has similar magnetic structure [100].

Mn_3SnN (MSN) displays a rich phase diagram, which is shown in Figure 4.5 [92]. Schematic representations of the structures are presented in Figure 4.5. The high-temperature phase (type 6) is collinear antiferromagnetic (AF), the lattice is tetragonally distorted with $c < a$ (T_1^-). The cubic, triangular spin-rotational phase has the same sense of rotation as in Mn_3NiN, starting in the Γ^{4g} configuration and rotating to Γ^{5g} with decreasing temperature. At lower temperatures, there are two phase transitions. In both phases the lattice is tetragonally elongated ($c > a$, T_1^+) with different lattice parameters in the two phases. In this temperature range, MSN exhibits a complex ferroic ordering characterized by Mn moments varying sinusoidally along the [001] direction with wave vector $\vec{k} = [00k_z]$ (the value of k_z is different in the two phases).

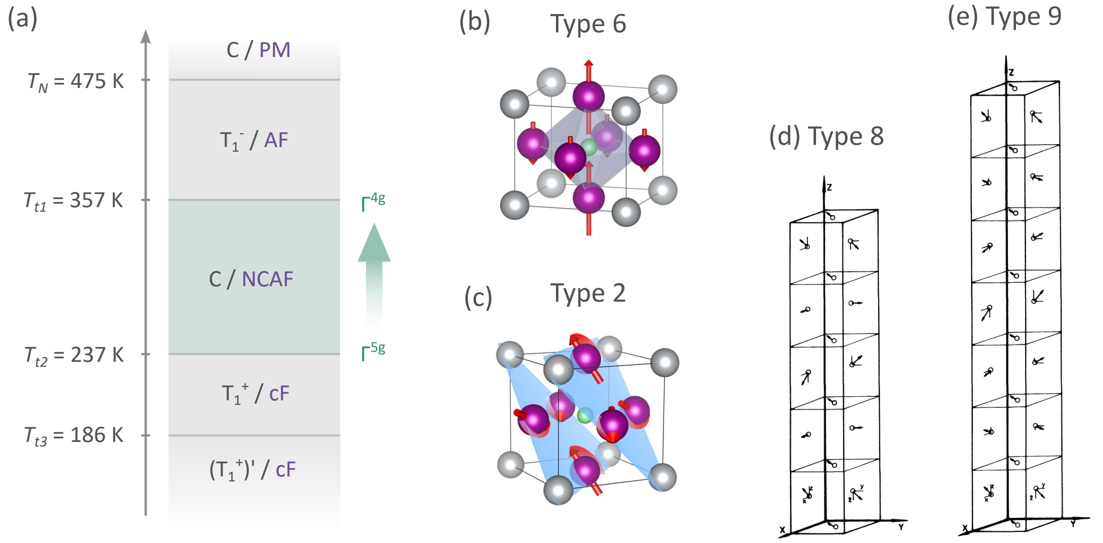

Figure 4.5: (a) Crystallographic and magnetic phases of Mn_3SnN bulk samples according to powder neutron diffraction experiments [92]. Crystallographic phases are as follows. C: cubic; T_1^-: tetragonally contracted; T_1^+, $(T_1^+)'$: tetragonally elongated with different lattice parameters. Magnetic phases are as follows. PM: paramagnetic; AF: collinear antiferromagnetic, shown in (b); NCAF: non-collinear antiferromagnetic, spin-rotational phase schematically depicted in (c); cF: complex ferroic, shown in (d), (e) and taken from Ref. [92].

The spin-rotational phases in Mn_3ZN (Z = Ni, Ag, Sn) are the result of temperature-dependent magnetic anisotropy. The temperature dependence of the in-plane spin angle θ_s can be written as [104]:

$$\sin[\theta_s(T)] = \frac{T - T_2}{T_1 - T_2} \text{ with } \begin{cases} T_1 < T_2 & \text{in } Z = \text{Ni, Sn} \\ T_1 > T_2 & \text{in } Z = \text{Ag} \end{cases} \tag{4.1}$$

Herein, T_1 and T_2 are the transition temperature from Γ^{5g} to spin-rotational and from spin-rotational to Γ^{4g}, respectively. In contrast, the triangular magnetic structures of the closely related cubic Mn_3Z (Z = Rh, Ir, Pt) have a magnetic structure that correspond to the Γ^{4g} irreducible representation [106–109].

The spin rotation in antiperovskite nitrides has important implications for their transport properties. It is shown in Chapter 3.2 (p. 26) that the anomalous Hall conductivity is zero in the Γ^{5g} but not in the Γ^{4g} configuration. Spin textures that can be described as combinations of the two irreducible representations have magnetic Laue group symmetry $\bar{3}$. Herein, the same AHC components as in the Γ^{4g} case are allowed, but the values of the tensor components depend on the in-Kagome-plane spin angle, as shown in Figure 4.6 taken from Ref. [110].

The authors of that work consider different antiperovskites Mn_3ZN (Z = Ni, Zn, Ga, Ag) and calculate first the magneto-crystalline anisotropy energy (MAE), shown in Figure 4.6(a). For instance, in Mn_3NiN the lowest energy state is found for an in-plane spin angle θ_s of 90°, which corresponds to the Γ^{4g} configuration. In all other materials, the Γ^{5g} is

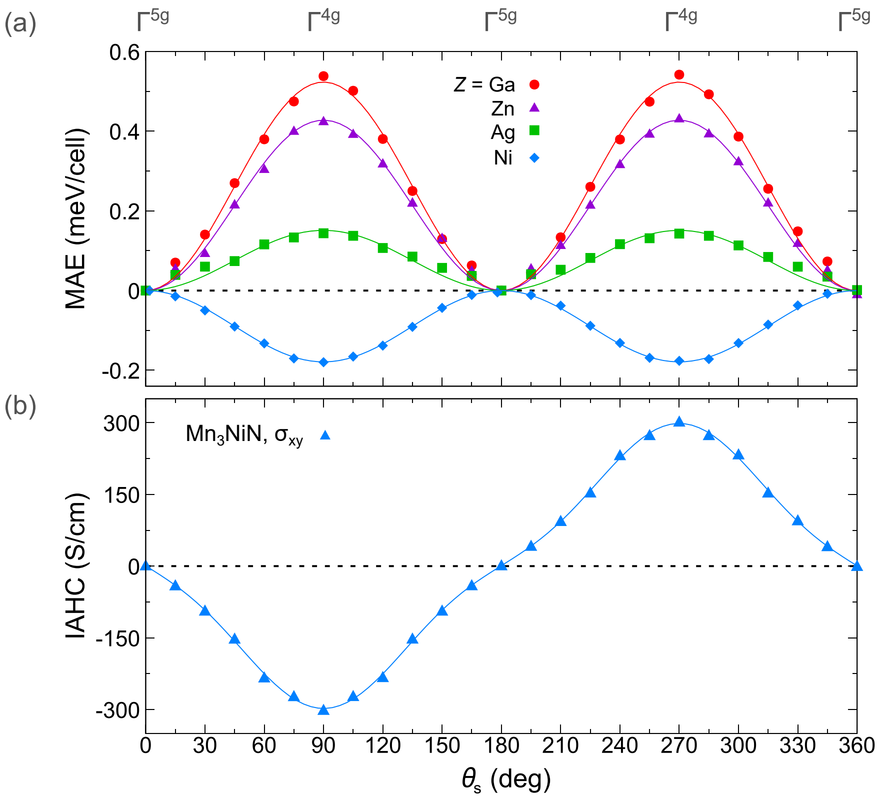

Figure 4.6: The effect of a varying in-plane spin angle on the magnetic anisotropy and the anomalous Hall effect in NCAFs with antiperovskite structure. Spin angle dependence of (a) magnetocrystalline anisotropy energy (MAE) of several Mn_3ZN (Z = Ni, Zn, Ga, Ag) compounds and of (b) the intrinsic anomalous Hall conductivity (IAHC) of Mn_3NiN. Taken and adapted with permission from Ref. [110].

found to be the lowest energy configuration. Although these calculation do not properly reflect the spin configurations found experimentally in Mn_3NiN and Mn_3AgN, they show that the MAE is bi-stable with respect to rotation of the spins within the Kagome plane. Furthermore, the intrinsic AHC σ_{xy} was calculated and it was found to depend roughly sinusoidally on the in-Kagome plane spin angle. The same result was obtained in Ref. [111] and is in agreement with the observation that the AHC is odd under time reversal, since $\theta_s(90^\circ) = -\theta_s(270^\circ)$.

4.2.3 Chirality in Triangular Magnetic Structures

The triangular spin textures observed in Mn_3ZN (Z = Ni, Zn, Ga, Ag, Sn) have a certain handedness or chirality. Both the Γ^{5g} and the Γ^{4g} configuration have right-handed chirality. Figure 4.7(b) shows a single (111) Kagome plane in the case of the Γ^{5g} magnetic structure, which is found in Mn_3GaN, for instance. When moving in a circle clockwise through the three Mn atoms, one can find that the spins rotate clockwise. In contrast, the sense of spin rotation in the case of the spin texture shown in Figure 4.7(a) is opposite.

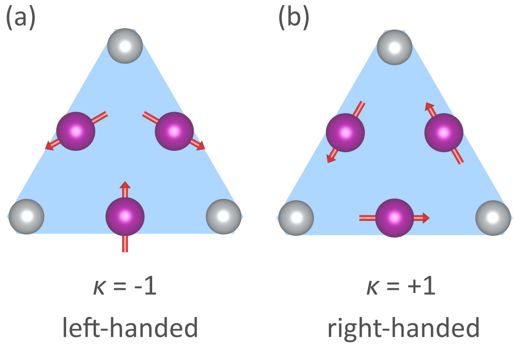

Figure 4.7: Examples of non-collinear coplanar spin textures with (a) left-handed and (b) right-handed vector spin chirality.

This spin texture has left-handed chirality. For non-collinear, coplanar spin textures, the handedness is parametrized by the vector spin chirality κ, defined as [112]:

$$\kappa = \frac{2}{3\sqrt{3}} \sum_{<ij>} \left[\vec{S}_i \times \vec{S}_j\right]_z = \begin{cases} +1 & \text{right-handed} \\ -1 & \text{left-handed} \end{cases} \tag{4.2}$$

Herein, the sum runs over all combinations of spins S_{ij}. The spin textures in the cubic materials Mn_3ZN (Z = Ni, Zn, Ga, Ag, Sn) and Mn_3Z (Z = Ir, Pt) have right-handed chirality, while those in the hexagonal Mn_3Z (Z = Ge, Sn) have left-handed chirality.

4.2.4 Other Magnetic Structures

Mn-based antiperovskites can host other complex spin textures. In many of these materials, the formation of the magnetically ordered state is accompanied by a lattice distortion, usually lowering the symmetry to tetragonal.

Mn_3CuN is tetragonally distorted (T_1^-) below 143 K and shows a complex non-collinear magnetic order of type 4 with a net moment along the [001]-direction [72].

Mn_3GeN shows type 1 (Γ^{5g}) ordering in a small temperature window at elevated temperatures. At room temperature, however, it has T_4 tetragonal symmetry and type 4 magnetic ordering similar to Mn_3CuN [72].

Fruchart and Bertaut describe another complex non-collinear magnetic structure, denoted here as type 5 ordering. It is found in T_1^+-distorted **Mn_3SbN**. Similar to the type 4 ordering found in Mn_3CuN, it corresponds to multi-sublattice ordering with a net ferromagnetic moment [72].

Lastly, **Mn_4N** can be viewed as an antiperovskite $(Mn_{II})_3Mn_IN$, with Mn_I occupying the corner sites, as shown in Figure 4.4. In contrast to all other compounds discussed above, the Mn on the Z site has a lower valence electron count and strong magnetic moment. As a result, the magnetic properties are very different. Mn_4N is a cubic, collinear ferrimagnetism with a high transition temperature of $T_N = 745\,K$ and saturation magnetization of $M_s = 1.14\,\mu_B$ at 77 K [74]. Although having a simple collinear magnetic structure, Mn_4N may be interesting for spintronics, because (001)-oriented Mn_4N thin films have perpendicular magnetic anisotropy (PMA), thereby rendering them potentially interesting for efficient domain wall motion [113].

4.3 Electronic Structure and Exchange

4.3.1 Valencies in Mn_4N

The valence states of antiperovskite nitrides have been investigated experimentally in a number of studies. Abe *et al.* [114] performed NMR studies on Mn_4N and found that the N atom is almost neutral. Later, it was found by electron diffraction [115] that in the closely related Ni_4N the valence state of N is -0.2 ± 0.2, thus is slightly negative. Barberon *et al.* [80] investigated solid solution of Mn_4N and Mn_3GaN, $Mn_3Mn_{1-y}Ga_yN$, as a function of y by X-ray diffraction. They determined the atomic form factors of N in the solid solutions and compared them to theoretical values for N in different oxidation states. They, too, find an oxidation state close to zero. Based on this finding, the electron configuration of Mn on the two sites is assumed to be for Mn_I: $[Ar]3d^{6.1\pm0.1}4s^{0.7\pm0.1}$ and for Mn_{II}: $[Ar]3d^{6.0\pm0.1}4s^{0.9\pm0.1}$.

4.3.2 Band Structure

Following the works of Fruchart *et al.* a tight binding model was established by Jardin and Labbé [116, 117]. Based on the observation that in some compounds, such as Mn_3SnN, the transitions from magnetically ordered to PM are not ideal Curie-Weiss-type order-disorder transitions but rather resemble the disappearance of individual local magnetic moments, the authors propose that the conduction electrons must be taken into consideration and the band structure at the Fermi level be studied in detail. Their theory is based on the mixing of N-$2p$ and Mn-$3d$ states. This hybrid band is superimposed by a much broader Mn-$4s$ band and the valence band of the Z site atom. The $3d$ states are crystal field-split into well separated subbands.

Jardin and Labbé find singularities in the density of states (DOS) at the Fermi level, the positions of which with respect to E_F are important for the observed physical properties and the magnetic structure. However, it was pointed out that such features are not found in modern DFT calculations and that the model only considers nearest-neighbor interaction [118].

DFT calculations of Mn_4N by Yu *et al.* [119] confirm the presence of N-p-Mn-d hybrid bands, which correspond to strong Mn-N bonds. As the authors find a charge transfer from Mn to N of 0.6, they propose that these bonds are covalent in nature. However, this is not in agreement with the experimental results discussed in the previous section.

Chen *et al.* further computed the DOS of various Mn_3ZN compounds [120] and found that they fall into two categories. First, those compounds with Z = Ni, Cu, Rh and Pd, which have a strong contribution of Z-$3d$ orbitals to the DOS around the Fermi level, superimposed by the Mn-$3d$ states. And secondly, those with Z = Zn, Ga, As, Ag, In, Sn and Sb, in which the Fermi level is dominated by Mn-3*d* orbitals, while the valence states of *Z* lie well below the Fermi level. It should be noted, however, that for the calculations incorrect magnetic structures were assumed for most compounds. Nevertheless, comparison to DFT calculations of Mn_3CuN using the correct magnetic structure [121] suggests that the general features are captured correctly.

4.3.3 Magnetic Exchange

Because of the presence of complex hybrid bands, different kinds of chemical bonds, a wide range of complex magnetic configurations and the important influence of the *Z* site atom, the nature of the magnetic interactions present in Mn_3ZN compounds is far from disclosed.

First, the plausible interactions in this class of materials are considered. Because of the absence of ionicity, indirect exchange mechanisms such as superexchange or double exchange may be discarded. Instead, it can be expected that conduction electrons play an important role. For the ferromagnetic or ferrimagnetic compounds, itinerant electron magnetism can be anticipated. Most notably, a band model for the collinear ferrimagnetic Mn_4N was proposed [122]. For other Mn_3ZN compounds, and especially for those with triangular magnetic configurations, the situation may be more complex. Fruchart and Bertaut argue based on PM susceptibility measurements that Ruderman-Kittel-Kasuya-Yosida (RKKY) interaction is an important exchange mechanism [72]. In the following, two reports concerning the evolution of triangular magnetic structures in Mn_3ZN are discussed.

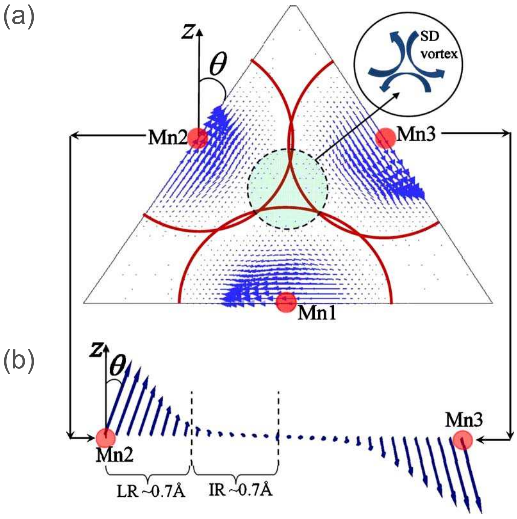

Figure 4.8: Results of spin density calculations by Lukashev and Sabirianov. (a) Spin density distribution (blue arrows) in the (111) plane in the case of Γ^{5g}-type NCAF structure in Mn_3ZnN. (b) Magnetization distribution between the Mn_2 and Mn_3 atoms (red) in the (111) plane. Taken from Ref. [123].

Lukashev and Sabirianov theoretically studied Mn_3ZnN as a model material [123]. They calculate the spatially resolved spin density distribution in the Γ^{5g} phase, shown in

Figure 4.8. They find that both direction and magnitude of the local spin density vary in the interstitial region between Mn atoms and form magnetization vortices in the center of the triangles in the (111) plane. The local regions close to the Mn atoms are dominated by 3*d* electrons, while the interstitial regions are predominantly occupied by delocalized *s*- and *p*-electrons. The results prove an important role of conduction electrons in mediating the magnetic moments between Mn in a RKKY-type manner. Also, the results suggest that a quasi-spin approximation, which assumes that the direction of spin density around an atom can be taken as constant, may not be applicable to Mn-based antiperovskite nitrides.

Interestingly however, this exact approach is taken by Mochizuki *et al.* [124], who propose a spin model for the triangular magnetic order. They employ replica-exchange Monte Carlo simulations to successfully replicate the structure of Mn_3ZN (Z = Ni, Zn, Ga, Ge, Ag). The work is based on a three sublattice model of magnetic moments located at the Mn sites, coupled by exchange interaction. The coupling is described using a classical Heisenberg Hamiltonian. The Mn-4*s* conduction electrons move under the influence of the Mn-3*d* potential mediated by *s*-*d* coupling. To recreate the spin textures observed experimentally, the degeneracy of the frustrated spins on the Kagome lattice must be lifted. To that end, exchange interaction and magnetic anisotropy are introduced.

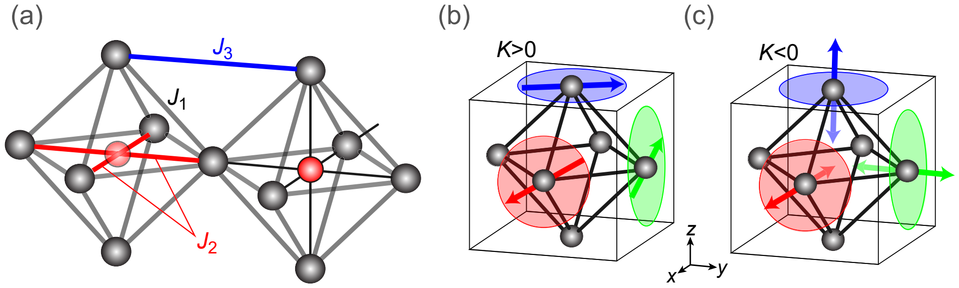

Figure 4.9: Three-sublattice model of NCAF order by Mochizuki *et al.* (a) Definitions of exchange constants for nearest-neighbor and next-nearest-neighbor interactions. (b) Easy plane ($K > 0$) and (c) easy axis ($K < 0$) magnetic anisotropy. Taken from Ref. [124].

Figure 4.9(a) shows the exchange interaction considered in the model. Next-nearest-neighbor interaction is either direct (J_3) or via N (J_2) and must be ferromagnetic ($J_{2,3} < 0$). Nearest-neighbor interaction is either parallel ($J_1 < 0$) leading to ferromagnetic order or antiparallel ($J_1 > 0$) leading to AF order. The sign of J_1 is governed by the Z site species.

In addition to magnetic exchange, easy-plane ($K > 0$) and easy-axis ($K < 0$) anisotropy are considered, as depicted in Figures 4.9(b) and (c). Again, the sign of K depends on the Z site species. This is explained on the basis of an energy-level scheme. Depending on the crystal field strength of Z relative to that of N the details of the splitting of the Mn-3*d* sub-bands are different and the highest occupied orbital points are either in-plane or out-of-plane. In the energy-level scheme it is assumed that the Mn atoms are in 3+ oxidation state, whereas experiment suggests that Mn is neutral. Nevertheless, the model is capable of recreating the experimentally found triangular structures.

Replica-exchange Monte Carlo simulations of a Heisenberg Hamiltonian based on the above assumptions allow to construct magnetic phase diagrams of Mn_3ZN for different values of J_i and K. It is found that for $J_1 < 0$ ferromagnetic order and for $J_1 > 0$ triangular order is established. Specifically, the latter is Γ^{5g} for $K > 0$ and Γ^{4g} for $K < 0$. The ferromagnetic order, on the other hand, is non-trivial as a result of competing ferromagnetic coupling and magnetic anisotropy. This observation is generally in agreement with experiment, e.g. the complex ferromagnetism of Mn_3CuN.

An important discovery of the work of Mochizuki *et al.* is that magnetic exchange interaction, parametrized by J_1, as well as magnetic anisotropy (K) are not independent of each other but closely related via the electronic structure and by the two competing crystal fields of Z and N [124].

Comparison of the works of Lukashev and Sabirianov and Mochizuki *et al.* shows that it is possible to approach Mn-based antiperovskite nitrides both from a purely metallic and a purely ionic viewpoint. This reflects the complex competing interactions resulting from the covalent bonding of the nitrides. From the discussion above one can summarize the role of the Z site species for the electronic and magnetic structure of Mn_3ZN compounds. Firstly, it acts as an electron donor and, therefore, changes the details of the band structure at the Fermi level. In addition, it affects the magnetic exchange interaction as well as the magnetic anisotropy due to competition of its crystal field strength with that of N.

4.4 Implications

An important observation is that triangular magnetic phases are hosted only in cubic lattices. In contrast, with the exception of Mn_3ZnN, all magnetic phases are accompanied by tetragonal lattice distortions. This suggests that triangular spin configurations are energetically favorable only when the bond lengths between the Mn atoms are the same, or, equivalently, when the Mn atoms form equilateral triangles on an undistorted Kagome lattice. Temperature-induced symmetry lowering of the crystal lattice leads to a lifting of this degeneracy and the emergence of other complex magnetic textures, as demonstrated in Figure 4.4.

In thin films, a lattice mismatch of the substrate and film material often leads to tetragonal distortion of the film material along the film normal [38]. Tetragonal distortions are also often assumed to occur in antiperovskite nitride thin films and cited as the mechanism allowing for domain structure control in these samples, thereby enabling the observation of intrinsic transport effects such as the anomalous Hall effect (AHE) [27,33,34]. Therefore, these effects should absent in unstrained thin films.

This is one of the questions addressed in this work. In the next part of this work, the absence of tetragonal distortions in Mn_3SnN thin films and the observation of displacements of the Mn atoms away from high symmetry lattice sites are discussed. Mn_3SnN was chosen as the studied material, as it shows a rich phase diagram in the bulk and is largely unexplored in thin film form. The atomic Mn displacements substitute tetragonal distortion as the mechanism for strain relaxation and NCAF domain structure control in Mn_3SnN thin films. Furthermore, they appear to stabilize the NCAF phase in a much wider temperature range as compared to bulk samples. Furthermore, in Part IV it will be shown that Mn displacements are not unique to Mn_3SnN and that they can also be found in other NCAF antiperovskite nitrides.

Part III

Crystallography, Magnetism and the Anomalous Hall Effect in Mn_3SnN

Chapter 5

Lead-in

The following part of this work presents experimental results of structural, magnetic and magneto-transport measurements of Mn_3SnN thin films. Chapter 6 discusses the optimization procedure of the thin film deposition parameters and presents results of thin film characterization addressing film composition, morphology, crystal structure and magnetic properties. Afterwards, anomalous Hall effect measurements performed on (001)- and (111)-oriented Mn_3SnN (MSN) thin films are discussed.

It is found that the anomalous Hall conductivity in (001)-oriented MSN is non-zero. This is in spite of the observation that these films appear as cubic in standard structural characterization by X-ray diffraction (XRD). In this case, a finite Anomalous Hall Effect (AHE) is unexpected. This observation motivated advanced XRD experiments using a six-circle diffractometer (SIXC) and structural refinement analysis including higher-order structural disorder. It is found that the crystal symmetry is not, in fact, cubic. Instead, it exhibits structural symmetry lowering characterized by statistical displacements of the magnetic manganese atoms away from the high symmetry lattice sites (Chapter 8). These manganese displacements lead to spin canting away from the perfectly compensated triangular magnetic structure observed in bulk samples, thus giving rise to a small net moment. In analogy to Mn_3Sn, which has an intrinsic spin canting due to magneto-crystalline anisotropy, this net moment coupled to the magnetic structure allows for control of the antiferromagnetic domain structure by magnetic field. This then leads to a domain imbalance when a magnetic field is applied, which enables the observation of a net AHE. The correlation of manganese displacements and the AHE in (001)-oriented Mn_3SnN is discussed in Chapter 9.

Furthermore, the (001)-oriented MSN thin films display an unusual temperature dependence. A model is developed to explain this observation on the basis of coherent spin rotation of the spins within the Kagome plane found in bulk MSN, as discussed in the Section 4.2.2. Because of the dependence of the anomalous Hall conductivity on the in-Kagome-plane angle, this spin rotation manifests in a temperature dependence of the AHE. This was the first observation of spin rotation through an indirect magneto-transport measurement in an antiperovskite nitride with non-collinear antiferromagnetic structure [36].

Chapter 6

Mn_3SnN Thin Films

6.1 Growth Procedure

The thin films growth comprised of two steps. First, the substrates were prepared by wet chemical processes to achieve reproducible substrate surfaces with terraces of single unit cell step height, on which Mn_3SnN (MSN) films were subsequently deposited. All films discussed in this part were grown on pyrolytic carbon substrates for Rutherford Backscattering Spectroscopy (RBS), $SiO_x(001)$ for X-ray Reflectivity (XRR) and otherwise on differently oriented $SrTiO_3$ (STO) single crystals for epitaxial thin film growth. The substrate preparation of STO is introduced in the first section and the general procedure for finding optimal growth parameters for MSN on STO is outlined afterwards.

6.1.1 Substrate Preparation of $SrTiO_3$

Single-side polished STO substrates with (001)- and (111)-orientation were purchased from Crystec GmbH, Berlin (Germany), and SurfaceNet GmbH, Rheine (Germany). The cleaning and etching procedures employed were based on standard procedures, as reviewed in Ref. [125].

The substrates were cleaned for 10 min in acetone in an ultrasonic bath and subsequently rinsed in deionized water and dried with a dry nitrogen gun. The same step was repeated for 10 min in ethanol. (111)-oriented substrates were afterwards soaked in deionized water for 4 min in an ultrasonic bath and dried with nitrogen. The surfaces were then etched by immersing the substrates in buffered hydrogen fluoride (BHF) solution of NH_4F and HF with a ratio of 7:1. (001)-oriented substrates were etched for 20 s and (111)-oriented samples were etched for 25 s. The etching was terminated by quenching the substrates in deionized water and drying them with nitrogen. Lastly, the substrates were annealed at 930 °C for 2.5 h (heating and cooling rate $<5\,^{\circ}\mathrm{C/min}$) under pure oxygen flow in a tube furnace.

The surface quality was confirmed for each substrate by atomic force microscopic (AFM) measurements of the surface. Representative AFM images of (001)- and (111)-oriented STO are presented in Figure 6.1. Substrates suitable for thin film growth show

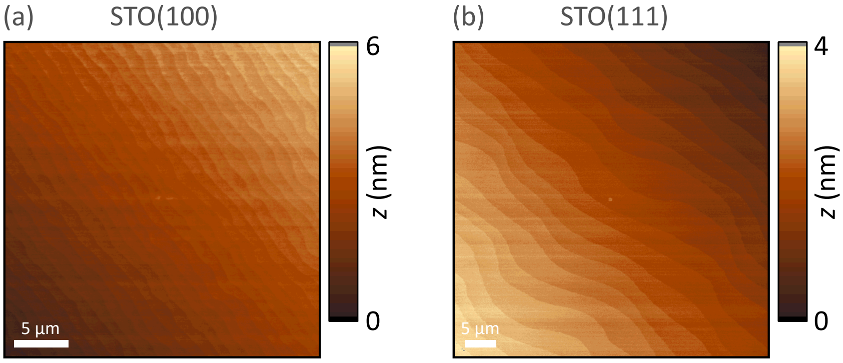

Figure 6.1: Atomic force microscopic (AFM) images of surfaces of (a) (001)-oriented and (b) (111)-oriented $SrTiO_3$ after substrate preparation.

clear terraces with a typical step length of 50 nm to 200 nm, depending on the miscut angle. The steps height in (001)-oriented STO corresponds to the lattice parameter of 3.905 Å. For (111)-oriented STO, it corresponds roughly to the (111) lattice spacing of 2.254 Å.

6.1.2 Growth Parameter Optimization

All Mn_3SnN thin films were grown in the MANGO sputtering system at the Max Planck Institute of Microstructure Physics by co-sputtering from Mn and Sn targets in Ar/N_2 background atmosphere. The typical base pressure of the system was $<1 \times 10^{-9}$ mbar.[1]

First, the thin film composition was optimized. The initial parameters were based on previously optimized parameters of Mn_3Sn. A series of films was grown on pyrolytic carbon substrates and the Mn and Sn sputtering powers as well as $Ar{:}N_2$ gas flow ratio varied. Pyrolytic carbon was used to allow for quantification of the N peak in the RBS spectra. The MSN layers were sandwiched between a few nanometers of Pt, a heavy scatterer that facilitates the fitting of the RBS spectra. All samples were deposited at room temperature. It should be noted that the composition of films grown at elevated temperatures may vary as a result of temperature-dependent sticking coefficients. The optimized parameters result in films with compositions of Mn_3SnN within the error margin, which are typically 0.5 % for Mn and Sn and 2 % for N [126]. Within this accuracy, the Mn_3SnN film are stoichiometric. The composition was confirmed in regular intervals and after loading new sputtering targets and the parameters adapted accordingly to give stoichiometric films.

The growth rate was calculated from thickness measurements by XRR of thin films on Si(001) substrates at room temperature. Afterwards, the substrate temperature during growth was varied and the films investigated by AFM, XRD, XRR and AHE measurements. All samples were capped with 3 nm thin TaN layers (deposition parameters in Table 6.1). Higher growth temperatures generally lead to higher crystallinity, as observed from an increased intensity of the main XRD peak in θ-2θ scans, but also higher surface and interface roughnesses (from AFM and XRR). Furthermore, in films grown on

---

[1] Binoy Krishna Hazra is greatly acknowledge for growing the samples and for discussion about the growth parameters and interpretation of the film characterization.

STO(111) higher growth temperatures lead to the evolution of growth facets other than (111). Therefore, the optimized deposition temperature of MSN(111) is 350 °C, compared to 500 °C in MSN(001). The optimized deposition parameters, the compositions from RBS and the calculated growth rates of the samples presented in this part are summarized in table 6.1.

Table 6.1: Optimized deposition parameters for Mn_3SnN thin films presented here. Composition obtained from RBS spectra and growth rates from XRR curves.

Parameter	Unit	Mn_3SnN (001) / (111)	TaN
Temperature	°C	500 / 350	80
Mn power	W	45	
Sn power	W	8	
Ta power	W		20
Atmosphere		Ar : N_2	Ar : N_2
Gas flow	sccm	25	25
Flow ratio		80 : 20	88 : 12
Pressure	mbar	4×10^{-3}	4×10^{-3}
Composition		3 : 1 : 0.96	1 : 1
Growth rate	Å/s	0.895	0.175

6.2 Thin Film Characterization by XRD, AFM and TEM

In the following chapters, exemplary experimental data of two differently oriented, 20 nm thin MSN films are presented. Except for the transmission electron microscopic (TEM) images, for which additional samples were prepared, all the results presented in the following chapters were obtained from the exact same two samples. Furthermore, additional samples were regularly deposited and measured to confirm the reproducibility of the results.

The crystallographic properties of the thin films were investigated by XRD and XRR. Figure 6.2(a) shows a specular θ-2θ scan of two 20 nm thick films grown on (001)- and (111)-oriented STO. One can observe that deposition with the optimized parameters presented above yields epitaxial thin films with the same out-of-plane lattice orientation as the substrates. The specular peak positions correspond to the bulk values of MSN. The lattice mismatch of (001)-oriented MSN on STO is 3.9 %. Therefore, a large compressive strain is expected in the thin film, which is expected to lead to a tetragonal elongation of the films out-of-plane and a resulting shift of the specular peaks, such as 002, towards lower angles. The observation that the peak positions correspond to the bulk values indicates that the films are fully relaxed. The peak intensities of the (111)-oriented sample are generally lower than for the (001)-oriented counterpart. This indicates a lower degree of crystallinity in the film, which may be result from the lower growth temperature.

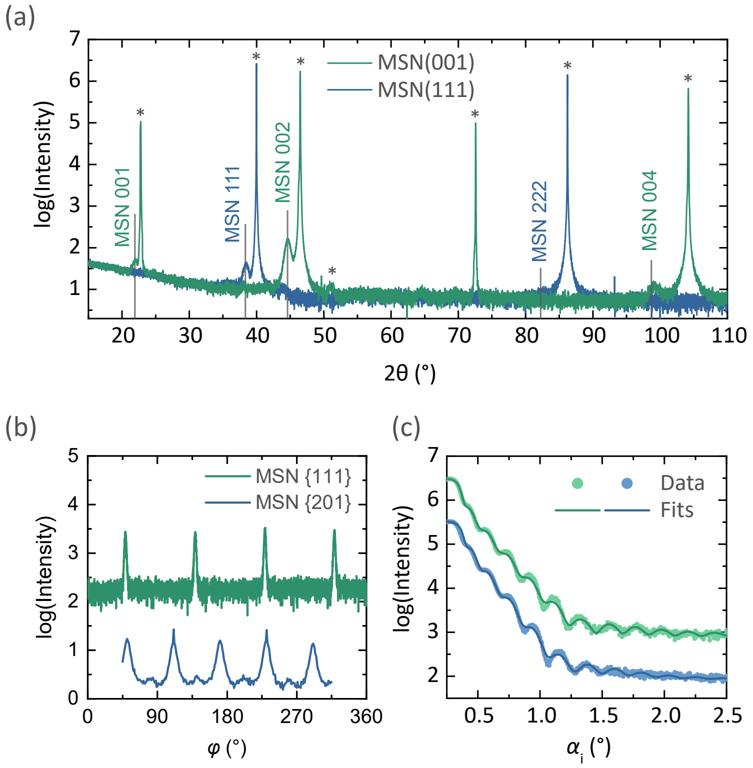

Figure 6.2: Results of standard structural XRD characterization of 20 nm thin MSN films on (001)- and (111)-oriented STO. (a) Specular θ-2θ XRD scan. Asterisks indicate substrate peaks and gray vertical lines indicate the angular positions of the respective peaks in bulk MSN. The films grow epitaxially on STO with the respective growth orientation. No other MSN peaks are observed in the films. A small peak at approx. 51° is due to the STO substrate as confirmed by a reference measurement of a bare STO substrate. (b) In-plane φ-scans of the MSN $\{111\}$ peaks in case of the (001)-oriented sample and $\{201\}$ peaks of the (111)-oriented sample. (c) Experimental XRR curves (scatters) and fitted curves (lines) of the same MSN samples. The data and fit of the (001)-oriented sample are shifted by one order of magnitude for clarity.

To further probe the epitaxial relationship of the substrates and films, in-plane φ-scans were recorded, presented in Figure 6.2(b). For the (001)-oriented sample, the MSN $\{111\}$ peaks were measured using the *Bruker* D8 system. A 4-fold symmetry can be observed, in agreement with the $Pm\bar{3}m$ space group. For the (111)-oriented sample, the $\{201\}$ peaks were measured. Because of the lower degree of crystallinity compared to the (001)-oriented samples and because of the lower intensity of the $\{201\}$ peak compared to $\{111\}$, these peaks could not be resolved using the *Bruker* D8 system. Instead, the six-circle diffractometer was used for these measurements.[2] For the $\{201\}$ planes, three peaks are expected every 120°. However, a 6-fold symmetry is found in this sample. This can be explained by the formation of crystal twins during growth, which have the same formation energy on the STO(111) surface. Additional peaks with an intensity by a factor 10 lower than the main peaks are found shifted by 30° from the main peaks. This indicates the presence of a minority phase rotated by this angle.

---

[2] In the six circle geometry the rotation angle of the sample around the surface normal is denoted θ rather than φ [49].

From the θ-2θ and φ-scans it is found that MSN grows epitaxially on STO in different growth orientations. (001)-oriented MSN shows a cube-on-cube epitaxial relationship with STO. In (111)-oriented MSN crystal twins are formed during growth, but the out-of-plane orientation follows that of the substrate.

XRR curves of the two samples are presented in Figure 6.2(c). Clear oscillations are observed that indicate smooth growth of the MSN and TaN layers. The curves are fitted using the program Leptos by *Bruker*. The layer thicknesses obtained from the fits are presented in Table 6.2. For MSN and TaN, they are close to 20 nm and 3 nm for both growth orientations and the samples are, therefore, referred to in the text as 20 nm thick films. The low roughness of both films is confirmed by AFM imaging of the deposited samples, presented in Figure 6.3.

Table 6.2: Layer thicknesses of MSN and TaN, t_{MSN} and t_{TaN}, obtained from XRR fitting and root-mean-square surface roughnesses, R_q, obtained from AFM.

	XRR		AFM
Orientation	t_{MSN} (nm)	t_{TaN} (nm)	R_q (nm)
(001)	20.5	3.1	0.86
(111)	19.9	3.4	0.74

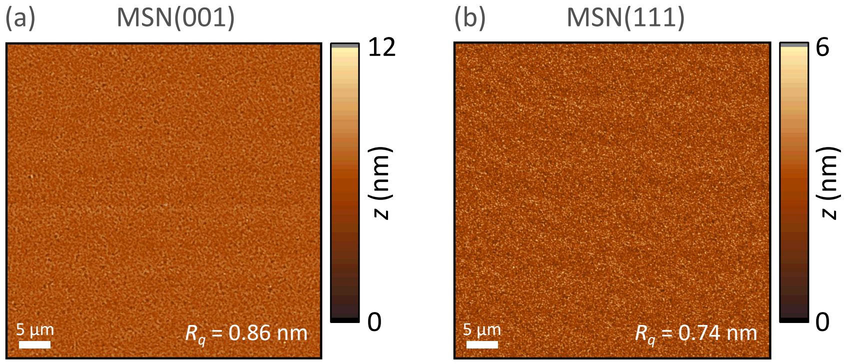

Figure 6.3: Atomic force microscopic (AFM) images and root-mean-square roughnesses R_q of surfaces of 20 nm thin Mn_3SnN films with (a) (001)- and (b) (111)-growth orientation.

To image the films along the growth direction TEM was employed.[3] Figures 6.4(a) and (b) show cross-sectional high resolution (HR) TEM images of the two differently oriented films. The cube-on-cube epitaxial relationship of STO(100) and MSN(001) is confirmed and the sample shows a very high degree of crystallinity. This is also evidenced by fast Fourier transform (FFT) images of the HR-TEM images in the STO and MSN regions in the vicinity of the interface, presented in Figures 6.4(d) and (e). The FFT image in the MSN region is nearly as clear as in the single-crystalline STO.

In the (001)-oriented sample, the signal appears to have slightly lower intensity in the first atomic layer of MSN. A similar effect has been observed in Ref. [127] in (001)-oriented Mn_3GaN films and was attributed to Mn deficiency as a result of chemical poten-

---

[3] Norbert Schammelt and Hakan Deniz are highly acknowledged for performing the TEM sample preparation and imaging and for their support in interpreting the data.

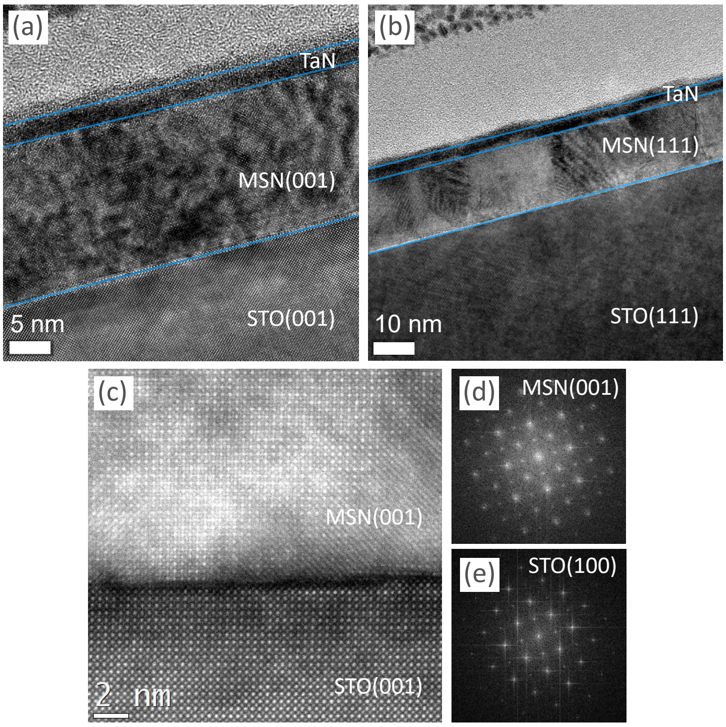

Figure 6.4: (a), (b) High resolution (HR) TEM images of (001)- and (111)-oriented MSN films. Blue lines indicate the positions of the interfaces of STO, MSN and TaN. The viewing direction is [100]. (c) Scanning TEM image of the (001)-oriented film in the vicinity of the interface with STO. (d), (e) Fast Fourier transform images obtained from the HR-TEM image of the (001)-oriented sample in the film and substrate regions, proving evidence for a high degree of crystallinity of the (001)-oriented film.

tial mismatch at the interface of the oxide substrates (STO and LSAT in that work) with the nitride film.

The (111)-oriented film shows much smaller grains of tens of nanometers size. While the crystal orientation cannot be resolved from the TEM images, these grains likely correspond to crystal twins, as indicated by the φ-scans discussed above. Furthermore, there are regions with no crystalline order. The lower degree of crystallinity of the (111)-oriented sample, as compared to the (001) counterpart, can be explained by the lower growth temperature. However, as discussed above, this is necessary to suppress the evolution of other growth facets during growth. It can be concluded that the (001) growth facet grows more readily than the (111) facet.

6.3 Magnetic Properties

Careful magnetometric characterization of the films was carried out using in-house SQUID-VSM (Superconducting Quantum Interference Device Vibrating Sample Magnetometry) and XMCD (X-ray Circular Magnetic Dichroism) measurements, performed at the VEKMAG end station at BESSY II at the Helmholtz Zentrum für Energie und Materialien Berlin.[4]

6.3.1 SQUID-VSM

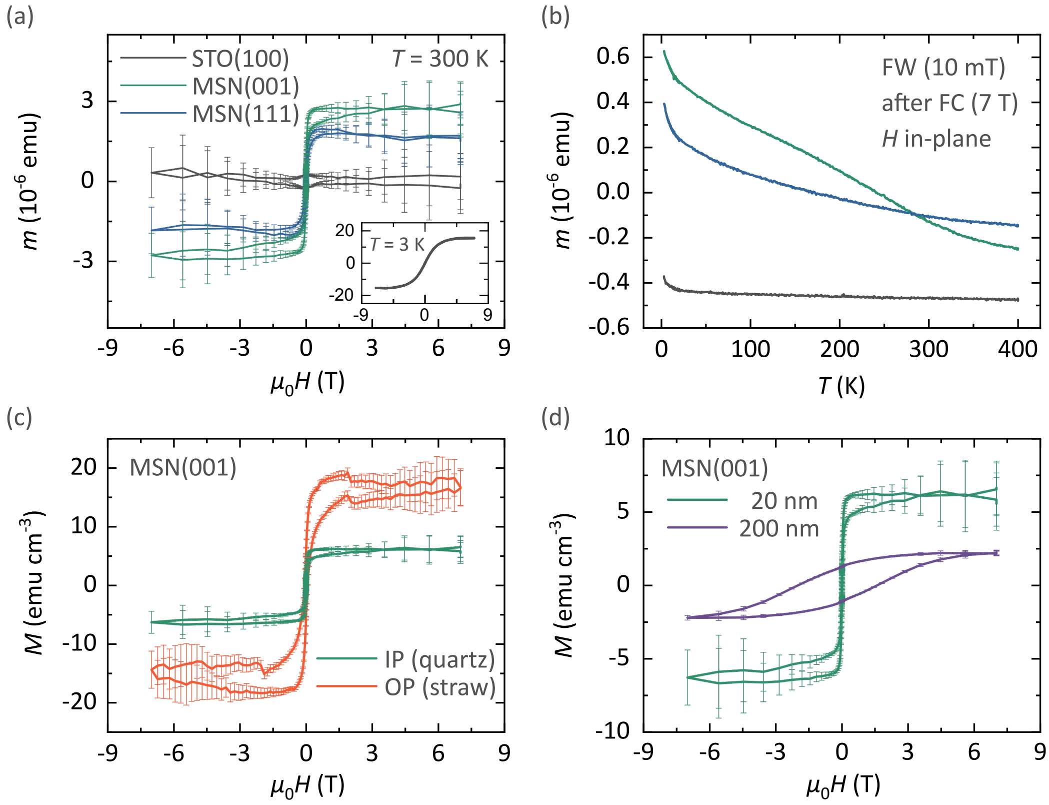

Figure 6.5: Results of magnetometric characterization of (001)- and (111)-oriented MSN thin films by SQUID-VSM. (a) Magnetic hysteresis loops at 300 K with magnetic field applied in-plane of MSN films and a bare STO substrate for reference. Linear background contributions were subtracted by linear interpolation of high-field data (also for the diamagnetic STO substrate). Inset: magnetization loop of the STO substrate at 3 K. (b) Temperature dependence of the magnetic moments of the three samples measured upon warming (FW) in a field of 10 mT after field cooling (FC) in 7 T. (c) Effect of using different sample holders on the apparent magnetization: quartz rod for in-plane (IP) and plastic straw for out-of-plane (OP) measurement. (d) Comparison of the M(H) loops of 20 nm and 200 nm thick (001)-oriented MSN.

Comparison of Samples with Different Growth Facets In-house magnetic measurements of the films were performed using a *Quantum Design* MPMS3 SQUID-VSM, operated in VSM mode. Figure 6.5(a) shows hysteresis loops at room temperature of 20 nm thin (001)- and (111)-oriented MSN films as well as of a bare STO substrate as references. The sample size of all three samples was approx. 5×5 mm and the figures shows magnetic moments *m*. The diamagnetic contributions from the STO substrate were subtracted by linear interpolation of the data at high fields.

---

[4] Support with the measurements and analysis by Florin Radu, Fred Chen, James Taylor, Amilcar Bedoya-Pinto and Pedram Bassirian is greatly appreciated.

This procedure was also performed for the bare STO substrate. Accordingly, the remaining magnetization is zero within the measurement error. This demonstrates that, at high enough temperatures, there is no magnetic signal other than that due to diamagnetism arising from the STO substrates, the quartz sample holder or the varnish used to glue the sample onto the holder. Therefore, the measured magnetic signal is assumed to arise from the films. The inset in Figure 6.5(a) shows an M(H) loop of the STO substrate at 3 K. The S-shaped magnetization loops indicates paramagnetism, which is likely due to defects in the substrate that become paramagnetic at low temperatures [128]. Therefore, paramagnetism from the STO substrate has to be considered at low temperatures.

By comparing the characteristic values of magnetization at remanence, M_r, and saturation, M_s, as well as the coercive fields, H_c, of the two differently oriented MSN films shown in Table 6.3, it is found that they are comparable in both orientation. The magnetic moments are close to the limits of detection of the SQUID-VSM, which manifests as relatively large measurement errors. Accordingly, the magnetization of the samples is very low. The saturation magnetization of the (001)- and (111)-oriented sample is $0.045\,\mu_\mathrm{B}/\mathrm{f.u.}$ and $0.030\,\mu_\mathrm{B}/\mathrm{f.u.}$ (see Table 6.3). For comparison, the weak magnetization due to canting in $\mathrm{Mn_3Sn}$ is $0.006\,\mu_\mathrm{B}/\mathrm{f.u.}$ [29]. The low coercivity of $<10\,\mathrm{mT}$ indicates weak in-plane magnetism.

Table 6.3: Summary of magnetic characterization by SQUID-VSM of $\mathrm{Mn_3SnN}$ thin films with different orientation and thickness. Measurements performed at 300 K with field in-plane using a quartz rod as sample holder. Remanent magnetization, M_r, and saturation magnetization, M_s (in units of $\mathrm{emu\,cm^{-3}}$ and $\mathrm{m}\mu_\mathrm{B}/\mathrm{f.u.}$) and coercive field $\mu_0 H_c$.

Film	M_r		M_s		$\mu_0 H_c$
	($\mathrm{emu\,cm^{-3}}$)	($\mathrm{m}\mu_\mathrm{B}/\mathrm{f.u.}$)	($\mathrm{emu\,cm^{-3}}$)	($\mathrm{m}\mu_\mathrm{B}/\mathrm{f.u.}$)	(T)
20 nm (111)	0.7	5.0	4.2	30.0	10.1×10^{-3}
20 nm (001)	0.9	6.7	6.2	44.7	9.3×10^{-3}
200 nm (001)	1.2	8.5	2.2	15.5	1.8

Figure 6.5(b) shows m vs. T scans of the three samples measured in a field of 10 mT upon warming from 5 K to 400 K after cooling from 400 K in a field of 7 T. The magnetization of the two MSN samples is low at all temperatures with a slight increase at low temperatures, which can be explained by the paramagnetic signal arising from the STO substrates. There is no indication of a phase transition over the entire measurement range.

The Effect of Sample Holders As sample holders, plastic straws and high purity quartz rods were used. However, *Quantum Design* advises against using plastic straws as sample holders in VSM mode because of the low rigidity of the straws, which can lead to artifact signals [129]. However, with quartz rods, only in-plane (IP) measurements can be performed and plastic straws have to be used for out-of-plane (OP) measurements. The issue of artifact voltages due to wrong choice of the sample holder is particularly pronounced in samples with very low magnetic moments, as demonstrated in the following.

Figure 6.5(c) show M vs. H magnetization loops of pieces of the 20 nm MSN(001) sample using different sample holders. For the IP measurement on a quartz rod the sample size was approx. 5×5 mm and for the OP measurement using a straw, the sample was cut in half and the sample size was approx. 2.5×5 mm. The measurement parameters (sample acceleration, averaged number of data points per field etc.) were identical for both measurements.

The magnetization plotted in the figure is calculated from the measured moment normalized to the film volume. It is observed that the apparent saturation magnetization of the sample measured in OP orientation with a straw rod is by a factor of 2 larger than in case of the IP measurement. This is unexpected, since the saturation magnetization should be identical regardless of measurement orientation. Furthermore, the error bars, calculated from the standard deviation of the averaged data points at each field are larger in case of the straw. This effect likely also results from the overall lower moment of the sample due to its lower volume. Nevertheless, it becomes evident that, indeed, for such low magnetic moments, plastic straws are not appropriate sample holders. Therefore, if not stated otherwise, all SQUID-VSM measurements in this work were performed using a quartz rod in IP configuration.

Origin of the Weak Magnetic Moments There are several effects that could give rise to the magnetic moments observed in the MSN films:

(I) Magnetic impurities from atomic defects in the bulk or at grain boundaries as well as interfacial defects at the interfaces with STO or TaN

(II) From the weak moment allowed by symmetry in the Γ^{4g} configuration pointing along the [111] direction

(III) From the canted moment induced by Mn displacements discussed in Chapter 8

In order to resolve the origin of the weak magnetization measured in the MSN films, samples with larger film thickness were grown. Figure 6.5(d) shows the magnetization loops of (001)-oriented MSN with 20 nm and 200 nm film thickness. The most notable difference is that in the 200 nm film, the magnetization loop exhibits much larger coercivity and is non-saturating, similar to the anomalous Hall effect loops in both samples, discussed in the next chapter. Furthermore, the remanent magnetization is much lower than in the thin sample (the smaller error bars are explained by the overall larger volume of the sample). Comparison of the magnetization data of the two films allows several conclusions. First, in the 20 nm film, the magnetization is defect-dominated. This explains the different shapes of anomalous Hall conductivity (AHC) and magnetic hysteresis in this sample. Comparison with the (111)-oriented sample, which has a similar magnetization but zero AHC, shows that this defect-driven magnetization does not give rise to an AHE. In the 200 nm thick film, on the other hand, defects are not the dominating contributor to the magnetization. This indicates that defects are not distributed evenly throughout the bulk of the films, and instead are located near the interfaces. Lastly, in the 200 nm film, the observation that both the AHC and the magnetic hysteresis are non-saturating indicates that they arise from the same physical phenomenon.

A summary of the magnetic properties of the MSN films at room temperature obtained by SQUID-VSM is presented in Table 6.3. The magnetization data presented here does not allow to unambiguously identify non-collinear antiferromagnetism in the entire temperature range, since the samples could, in principle, be collinear antiferromagnetic. Nevertheless, pronounced ferroic order (ferro- or ferrimagnetic) can certainly be excluded. This has two important implications. Firstly, it is a strong indication that the magnetic phase diagram of MSN thin films is very different from that of previously reported bulk samples, in which complex ferroic phases were observed at low temperature [see Figure 4.3 (p. 33)]. Secondly, it means that the AHE observed in (001)-oriented MSN, discussed in the next chapter, cannot be attributed to ferromagnetism.

6.3.2 XMCD

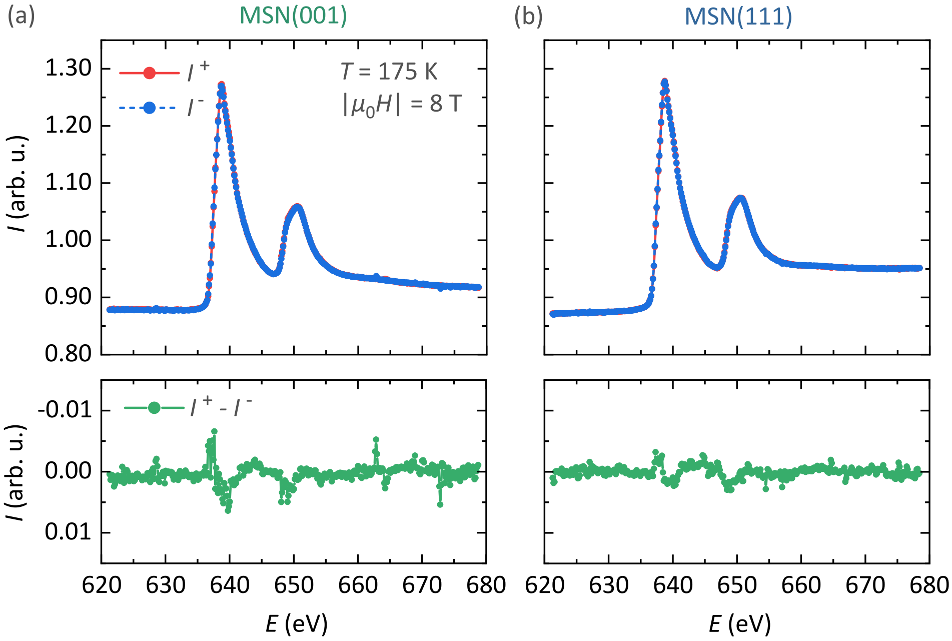

Figure 6.6: XMCD measurement of 20 nm thin (a) (001)-oriented and (b) (111)-oriented MSN films at 175 K with the beam under grazing incidence (GI). Top: measured intensities for positive (I^+) and negative (I^-) magnetic fields with a magnitude of 8 T. Bottom: difference spectra $I^+ - I^-$.

X-ray magnetic circular dichroism (XMCD) measurements were performed at the Mn $L_{2,3}$ edge to confirm the vanishingly small magnetization in the differently oriented MSN films. Figure 6.6 shows the X-ray absorption spectra (XAS) measured in total electron yield mode of the (001)- and (111)-oriented film under application of fields of ± 8 T. The X-ray beam had positive circular polarization and was under grazing incidence (GI, 20° with respect to the sample surface). The presented data is taken at 175 K. At this temperature a large anomalous Hall resistivity is found (Chapter 7). If the AHE is due to the magnetization of the sample, a high XMCD is also expected at this temperature.

The XMCD signal is very low, indicating low net spin and angular momenta at the Mn sites. The normalized XMCD signal is smaller than the standard deviation of the measured difference spectrum $I^+ - I^-$ divided by the edge jump of the absorption curve. This value is $< 0.42\,\%$ for the (001)-oriented sample. XMCD sum rule analysis cannot be performed, because the lineshape is not clearly resolved.

To obtain an upper estimate of the magnetic moment per Mn atom in the (001)-oriented MSN film (which shows a non-zero AHE), the normalized XMCD signal is compared to the values found in previous measurements of Mn_3Sn and Mn_3Ir thin films of similar thickness, for which sum rule analysis was possible [130, 131]. The reported normalized XMCD values and magnetic moments (per formula unit and per Mn atom) are presented in Table 6.4. The ratio of m_s^{eff} (in $\mu_\mathrm{B}/\mathrm{Mn}$) and XMCD (in %) is then calculated. The XMCD signal measured in MSN and the moment per XMCD ratio found in Mn_3Sn are used to estimate the moment per Mn in the (001)-oriented MSN. Thereby, it is found that the magnetization is $<0.024\,\mu_\mathrm{B}/\mathrm{Mn}$. This is only a rough estimate of the magnetization of the (001)-oriented MSN film. Nevertheless, it confirms the low magnetization of the order of magnitude of few tens of $\mathrm{m}\mu_\mathrm{B}/\mathrm{f.u.}$ found by SQUID-VSM measurements (see Table 6.3).

Table 6.4: Normalized XMCD values (estimates from the cited references) and (reported or calculated) effective spin moments per formula unit and per Mn atom of different NCAFs. The ratio $m_s^{\mathrm{eff}}/\mathrm{XMCD}$ of Mn_3Sn is used to estimate the spin moment per Mn in the Mn_3SnN films.

Material		XMCD (%)	m_s^{eff} ($\mu_\mathrm{B}/\mathrm{f.u.}$)	m_s^{eff} ($\mu_\mathrm{B}/\mathrm{Mn}$)	$m_s^{\mathrm{eff}}/\mathrm{XMCD}$ ($\mu_\mathrm{B}/\mathrm{Mn}/\%$)
Mn_3Sn	[130]	1.60	0.279	0.093	0.058
Mn_3Ir	[131]	0.50	0.06	0.02	0.040
Mn_3SnN		0.42	0.07	0.024	

Chapter 7

Anomalous Hall Effect Measurements

Before presenting the results of anomalous Hall effect measurements of Mn_3SnN (MSN) thin films, the starting point of the discussion is briefly outlined. In powder form, MSN was found, by neutron diffraction, to have a non-collinear antiferromagnetic (NCAF) phase between 237 K and 357 K [72, 92]. Moreover, this phase displays temperature-dependent spin rotation and the spins rotate coherently within the (111) Kagome plane as a function of temperature between two spin configuration that correspond to two irreducible representations. Following the notation of Bertaut, Fruchart *et al.* they are denoted Γ^{5g}, if the in-plane spin angle θ_s is 0° or 180° and Γ^{4g}, if θ_s is 90° or 270° (see Chapter 4.2.2).

These magnetic configurations can give rise to a non-zero total Berry curvature of the electronic bands, which results in a finite anomalous Hall conductivity, despite the absence of significant magnetization. The AHC is roughly proportional to the sine of the in-plane spin angle θ_s [110]. Therefore, it is zero in the Γ^{5g} and at a maximum in the Γ^{4g} configuration. Furthermore, the magnitude of the AHC depends on the relative orientation of electric field, magnetic field and crystal axes. The maximum AHC is measured when the current passes within the Kagome plane and the field is applied perpendicular to it [61]. Furthermore, the presence of multiple magnetic domains can cancel the AHE in a real sample. Magnetic domains related by a spin rotation of the spins by 180° are degenerate [110]. This symmetry operation is equivalent to time reversal. Since the AHC is odd in Berry curvature and Berry curvature is odd under time reversal, the sign of the AHC is exactly opposite in two domains related by spin rotation [14, 16, 17, 61, 110]. Therefore, in the absence of any mechanism that allows to set a preponderance of one domain type over the other or a single domain state, the anomalous Hall current contributions of the different domain exactly cancel.

In the previous chapter, the growth of single-crystalline epitaxial MSN thin films with (001)- and (111)-orientation was demonstrated. The films grow smoothly and epitaxially on the differently oriented STO substrates. Careful magnetometric characterization shows that the films have very low magnetization, which is dominated by defects in the 20 nm thin films. Most importantly, the (001)-oriented films have a bulk-like cubic lattice metric with $a = b = c = 4.060(7)$ Å. Therefore, it is expected that (001)-oriented MSN does not exhibit an AHE, since there should be no mechanism for domain control. In the following chapter, it will be demonstrated that, nevertheless, an AHC with an unusual temperature dependence is measured in this growth orientation. This discrepancy will be resolved in Chapter 9 by the observation of Mn displacements, which give rise to spin canting and a resulting net moment, which allows for domain control by magnetic field.

7.1 Hall Effect Measurements

7.1.1 Facet Dependence

For the transport measurements, MSN thin films were patterned into Hall bar devices using photo-lithography.[1] The devices were etched by Ar ion beam milling and a metallic bilayer consisting of Ti (2 nm) /Au (100 nm) was used for contact pads. A microscopic image of a fabricated Hall bar device with the bonding scheme employed for longitudinal and transversal voltage measurements is shown in Figure 7.1(a). All transport measurements were performed in a 9 T PPMS by *Quantum Design*, using *Keithley* 6221 current sources and *Keithley* 2182A nano-voltmeters.

From the measured voltage U, the applied current (typically in range of $I = 1\,\mathrm{mA}$) and the Hall bar dimension (width w, distance between Hall leads l and film thickness t) the longitudinal and transverse resistivity are calculated as $\rho_{xx} = \frac{U}{I}\frac{wt}{l}$ and $\rho_{xy} = \frac{U}{I}t$. ρ_{xy} is shifted along the ordinate axis to correct for offset voltages originating from the voltmeter.

From the temperature dependence of ρ_{xx}, shown in Figure 7.1(a), it becomes evident that MSN shows metallic behavior. The residual resistance ratios $\mathrm{RRR} = \rho_{xx}^{300\,\mathrm{K}}/\rho_{xx}^{5\,\mathrm{K}}$ of the (001)- and (111)-oriented films are 1.7 and 1.4. More importantly, there is no indication of any phase transition in either film.

Hall effect hysteresis loops at various temperatures of the differently oriented films are presented in Figures 7.1(c) and (d). In both growth orientations, the curves are dominated by the linear contribution of the ordinary Hall effect. In the (001)-oriented case, there is an additional contribution identified as the AHE. The two contributions are separated by linear interpolation of the data at high fields. This procedure is shown in Figure 7.1(b) for data recorded at 175 K. The Hall slope is positive at all temperatures and temperature-dependent. This indicates hole-type charge carriers with temperature-dependent charge carrier concentration. A similar effect has previously been observed in $\mathrm{Mn_3GaN}$ and $\mathrm{Mn_3Ge}$ thin films [27, 132]. In both cases, the Hall slope even changes sign, indicating a change in charge carrier type. However, in both cases, the absence (in the case of $\mathrm{Mn_3GaN}$) and presence (in $\mathrm{Mn_3Ge}$) of the AHE is robust under the change in charge carrier type. Therefore, the charge carrier type and concentration are assumed to have no effect on the AHC discussed in the following.

Zero AHC was previously observed in thin films of the NCAF with cubic crystal structure $\mathrm{Mn_3Ir}$ with (111)-growth orientation [131]. Based on theoretical considerations

---

[1] Banabir Pal is greatly acknowledged for performing the device fabrication.

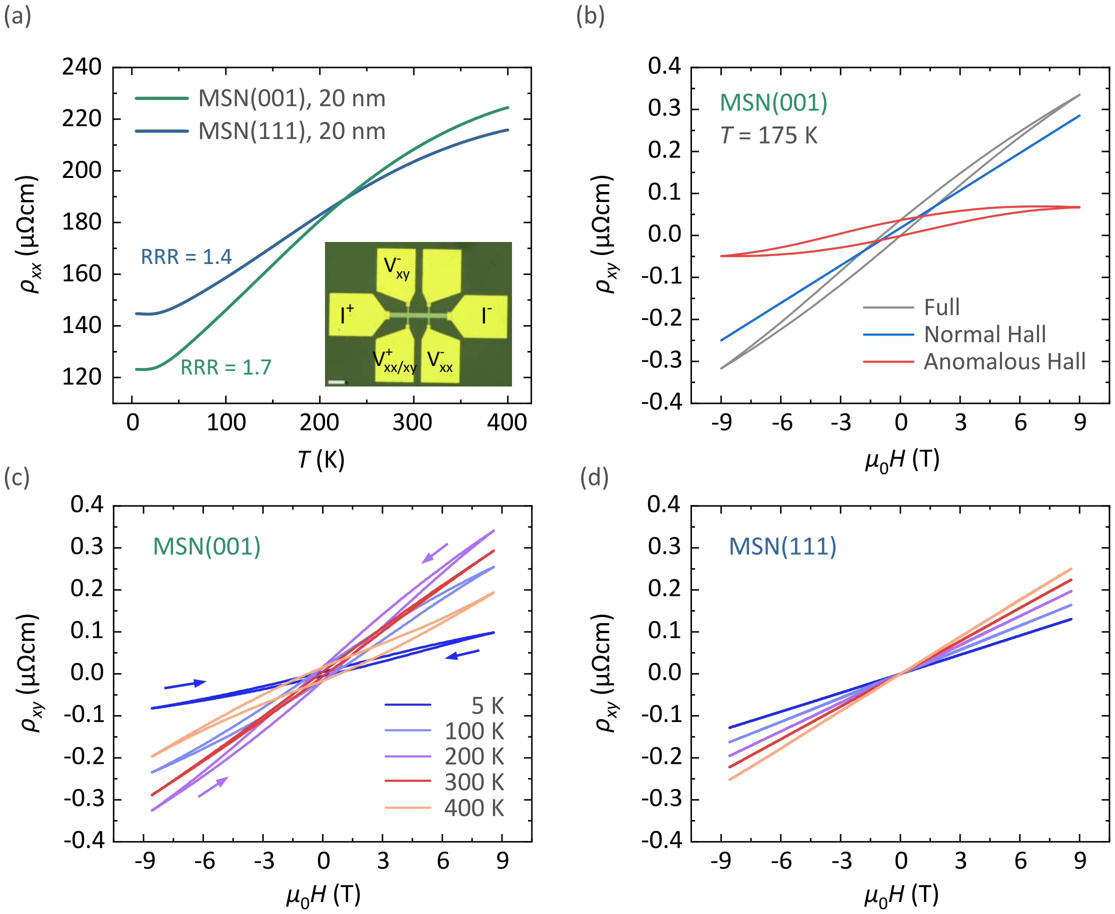

Figure 7.1: Longitudinal and transversal resistivity of 20 nm thin (001)- and (111)-oriented Mn_3SnN films. (a) Temperature dependence of the longitudinal resistivity, displaying metallic behavior. The inset shows an optical image of a fabricated Hall bar device and the bonding scheme employed for the measurements (the scale bar is 50 μm). (b) Full Hall effect loop of (001)-oriented MSN at 175 K and ordinary Hall and anomalous Hall contributions. (c), (d) Full Hall effect loops of differently oriented MSN at various temperatures. A non-zero AHE is only observed in the (001)-oriented sample.

assuming a single domain state, the AHC is expected to be at a maximum in this measurement configuration, as described in Chapter 3.2 (p. 26). However, in this configuration the magnetic field is applied perpendicular to the (111) Kagome planes. Therefore, even if there were weak moments in the Kagome plane, the distribution of magnetic domains related by 180° spin rotation could not be controlled by magnetic field. Therefore, the AHE contributions of the different domains exactly cancel, thus leading to a net zero AHC. This finding underlines the crucial role of weak moments coupled to the NCAF structure in the observation of transport effects in NCAFs. Furthermore, it also shows that potential spin canting out of the (111) plane does not contribute to the hysteretic AHC in either growth orientation. It is possible that spin canting out of the Kagome plane may contribute to the total Hall signal but in a non-hysteretic fashion. Therefore, it would not be possible to distinguish this contribution from the ordinary Hall effect.

The AHC $\sigma_{xy}^{\mathrm{AHE}} = -\rho_{xy}/\rho_{xx}^2$ of the differently oriented samples is plotted in Figures 7.2(a) and (c). With the linear contribution of the ordinary Hall effect removed, a strong

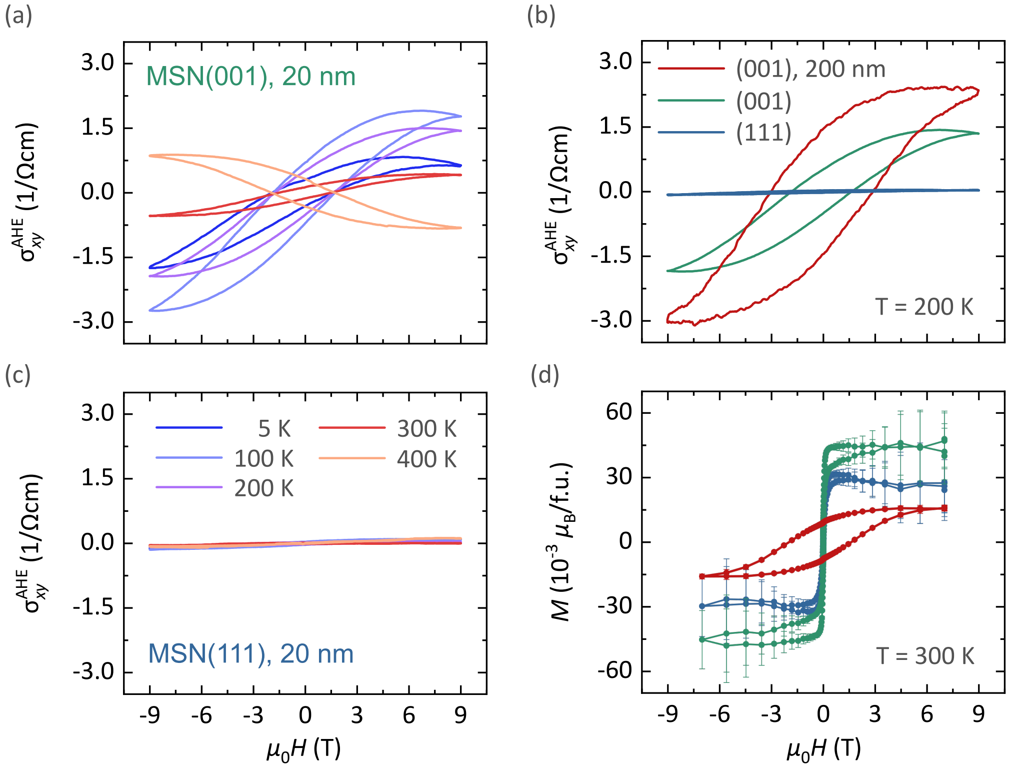

Figure 7.2: Anomalous Hall effect in (001)-oriented Mn_3SnN and comparison with magnetization data. (a), (c) Anomalous Hall conductivity loops of (001)- and (111)-oriented Mn_3SnN at various temperatures. (b), (d) Comparison of the AHC loops at 200 K of 20 nm films with both orientations and a 200 nm (001)-oriented film as well as the corresponding magnetic hysteresis loops at 300 K.

temperature dependence of the AHC in the (001)-oriented sample becomes evident. By comparison of the AHC and magnetization data of both samples, shown in Figures 7.2(b) and (d), magnetization can be excluded as a main contributor to the AHC signal in (001)-oriented MSN. Firstly, as established in Chapter 6.3, the magnetization is very low. Secondly, zero AHC is found in the (111)-oriented sample, despite it having a magnetization similar to that of the (001)-oriented sample. If a magnetization of this magnitude were sufficient to cause the AHC observed in the (001)-oriented sample, an AHC of similar magnitude would also be expected in the (111)-oriented sample, which is not the case.

Furthermore, in a typical ferromagnet, in which the AHC is proportional to the magnetization, the hysteresis loops of magnetization and AHC exhibit the same shape and coercivity. This is not the case in the 20 nm thin (001)-oriented sample. However, a correspondence between the AHC and magnetic hysteresis loops found in the 200 nm film. As discussed in Chapter 6.3, the magnetization of the thinner film is dominated by magnetic defects. Evidently, these magnetic moments do not generate the observed AHE. In the thicker film, an intrinsic magnetization is measured, which originates from the same phenomenon as the AHE in both 20 nm and 200 nm films. One possibility is a weak moment allowed by symmetry in the Γ^{4g} configuration. However, in bulk material, the resulting magnetization is $< 0.5 \times 10^{-3}\,\mu_B/\text{f.u.}$ [92], which is more than one order of magnitude lower than the magnetization measured in the 200 nm film ($M_s = 15 \times 10^{-3}\,\mu_B/\text{f.u.}$).

Therefore, it is more plausible that the magnetization is due to the canted moment resulting from the Mn displacements discussed in the next chapter. These canted moments fulfill several criteria. First, in analogy to Mn_3Sn, the canted moments, which are coupled to the local spin texture, allow for domain structure control by magnetic field. Magnetic hysteresis is associated with domain wall motion. Thus, the canted moments can explain the hysteretic nature of both magnetization and AHC. Secondly, the magnitude of the canted moment is irrelevant for the AHC. This is warranted by the observation that in the 20 nm film the larger magnetization due to defects is not the main contributor to the AHE and that the lower magnetization in the 200 nm film correlates with an even larger AHC compared to the 20 nm film.

One important difference between the AHE in MSN and Mn_3Sn is the non-saturating nature of the loops in the case of MSN, while in Mn_3Sn the magnetic and AHC hysteresis is very sharp with low coercivity [29]. There are two possible explanations for the unusual hysteresis in MSN. Firstly, it may result from the different origins of the canted moments in the two compounds. In Mn_3Sn, the moment is intrinsically coupled to the magnetic structure. In contrast, in MSN, the canted moment is most likely generated by Mn displacements and is, therefore, strongly and locally correlated with Mn displacements. Furthermore, MSN has uniaxial magnetic anisotropy, while in Mn_3Sn, the Kagome plane is an easy plane [110, 133]. Therefore, the energy barrier to achieve spin rotation by 180° is much larger in MSN than in the easy-plane material Mn_3Sn. Another possible explanation is that the application of external magnetic fields affects the details of the NCAF structure. Gomonaj and L'vov have studied the spin-rotational phase in isostructural Mn_3NiN phenomenologically and found that the in-plane spin angle θ_s is a function of both temperature (as found experimentally by powder neutron diffraction) as well as of magnetic field. At a given temperature, assuming the structure is not already in the Γ^{4g} configuration, the application of a magnetic field rotates the spin texture towards the Γ^{4g} configuration. It is possible that this effect contributes to the magnetic and AHE hysteresis. The differences between Mn_3SnN and Mn_3Sn are further addressed in Chapter 9.2.2 (p. 91).

7.1.2 Temperature Dependence

From Figure 7.2(a) it can be seen that the AHC in the (001)-oriented MSN film is strongly temperature-dependent in magnitude and sign. This is highlighted in Figure 7.3(a), which shows the remanent AHC, $\sigma_{xy}^{\mathrm{rem}}$, plotted against temperature. The AHC of the (001)-oriented sample does not display any sudden jumps as a function of temperature. This is in agreement with measurements of the temperature dependences of magnetization, longitudinal resistivity and crystal structure (Chapter 8). The absence of any features indicating crystallographic or magnetic phase transitions is unexpected, given the complex phase diagram of MSN in bulk form. According to powder neutron diffraction measurements, bulk MSN is collinear antiferromagnetic between $T_N = 475\,\mathrm{K}$ and 357 K. From 357 K to 237 K, it is non-collinear antiferromagnetic. At lower temperatures, complex ferroic

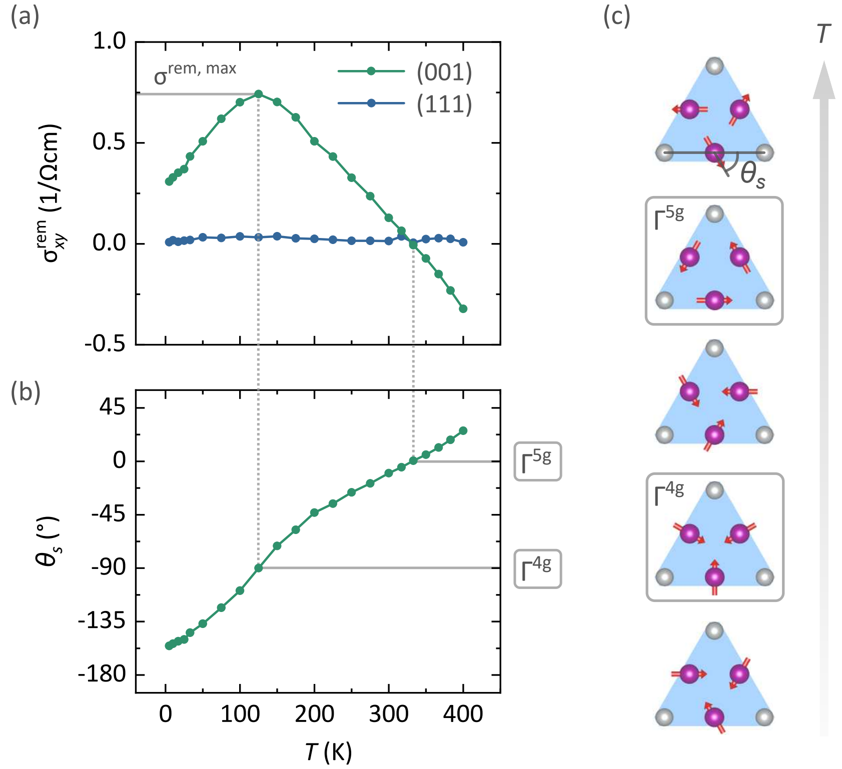

Figure 7.3: Modeling the unusual temperature dependence in (001)-oriented Mn_3SnN by the presence of temperature-dependent spin rotation. (a) Remanent AHC after application of 9 T for both growth orientations. (b) The calculated in-plane spin angle θ_s as a function of temperature. (c) Schematic representations of the corresponding spin structures at selected temperatures, viewed along the [111] direction.

phases with significantly larger magnetization are observed [72,92]. Therefore, the NCAF phase is stabilized in MSN thin films with (001)-orientation over a much wider temperature range than in bulk. Moreover, (111)-oriented films also do not display a pronounced AHE at lower temperature, which would be expected based on the bulk phase diagram. It should be stressed that the presence of NCAF order in the MSN films is inferred from combined magnetic and magneto-transport measurements. The NCAF structure can be measured more directly by neutron diffraction. In the case of Mn_3GaN, neutron diffraction experiments of thin films confirm the presence of the NCAF order corresponding to the Γ^{5g} configuration at all temperatures, which corresponds to the bulk structure of Mn_3GaN [27].

The unusual temperature dependence of the AHC in (001)-oriented MSN is resolved by considering that bulk MSN displays temperature-dependent spin rotation in the NCAF phase [92]. The spins retain an angle of 120° with respect to each other, but rotate coherently within the Kagome plane. Because of the sine dependence of the AHC on the in-plane spin angle, it is expected that this spin rotation manifests in a temperature-dependent AHC. Therefore, $\theta_s(T)$ is calculated using the measured remanent AHC as:

$$\theta_s(T) = \arcsin\left(\frac{\sigma_{xy}^{\mathrm{rem}}}{\sigma_{xy}^{\mathrm{rem,\,max}}}\right) \tag{7.1}$$

It is implicitly assumed that the observed AHE is of intrinsic origin and that spin rotation dominates its temperature dependence. The calculated spin angle is plotted against temperature in Figure 7.3(b) and graphical representations of the corresponding magnetic structures are presented in Figure 7.3(c). θ_s varies continuously and roughly linearly with temperature, as is the case in the powder neutron diffraction measurements of bulk MSN [92], albeit in a much smaller temperature range owing to the reduced phase stability of the NCAF phase. A similar temperature dependence of the AHC was previously reported in (001)-oriented MSN thin films [34]. However, the authors present only data between 50 K and 300 K and only state that the AHC does not scale with the sample magnetization. The discussion of the temperature dependence of the AHC in an antiperovskite nitride based on a spin-rotational phase presented here was the first report of this kind [36].

Within this model, spin rotation occurs in a wide range of θ_s. This is likely due to the NCAF phase being stabilized in the entire temperature range from 4 K to 400 K. In contrast, the NCAF phase is stable in bulk samples over a temperature range of only $\approx 120\,\mathrm{K}$. Here, the spins rotate from $\theta_s \approx 45^\circ$ at the highest temperature of 400 K towards Γ^{5g}. This configuration occurs at 330 K, at which the AHC vanishes. At lower temperatures, the spins rotate further towards the Γ^{4g} configuration, which is reached at 125 K (temperature of maximum AHC) and further at lower temperatures. In contrast, in bulk MSN, spin rotation occurs only from 90° to 45° [92].

The origin of the temperature-dependent spin rotation in antiperovskite nitrides was studied phenomenologically by Gomonaj and L'vov in terms of a temperature-dependent magneto-crystalline anisotropy [104]. This effect is due to small changes in the lattice constants with temperature. The situation is possibly more complex in thin films, since constrictions imposed by the substrate as well as strain-induced symmetry lowering have to be taking into consideration. In fact, as will be discussed in Chapter 8, because of the presence of atomic Mn displacements, the crystal structure of the MSN films reported here deviates significantly from the bulk structure. The Mn displacements may also have an impact on the temperature dependence of the magnetic anisotropy. Thereby, they may affect the spin rotation and, by extension, the temperature dependence of the AHC.

7.2 Discussion

A finite AHE is observed in (001)- but not in (111)-oriented MSN films. Comparison of the magnetization and transport data of the differently oriented samples with different thicknesses shows that the AHE does not result from the small magnetization observed in the samples. The vanishing AHC in (111)-oriented MSN can be explained by the presence of multiple magnetic domains related by spin rotation by 180°. This observation underlines that spin canting in NCAFs is essential to control the magnetic domains, which results in a net AHC.

(001)-oriented MSN films exhibit an unusual temperature dependence of the AHC. Most importantly, the AHC changes sign at around 330 K. This effect has not been observed in any antiperovskite nitride before. A model to explain this unusual trend was developed, which considers that bulk MSN shows a spin-rotational NCAF phase, in which the spins rotate coherently within the Kagome plane as a function of temperature. Because of the magnetic symmetry dependence of the AHC on the in-Kagome-plane spin angle, this spin rotation manifests in a temperature-dependent AHC.

Spin-rotational NCAF phases have been found by powder neutron diffraction in the antiperovskites Mn_3NiN, Mn_3AgN and Mn_3SnN [83, 90, 92]. However, although AHE measurements of Mn_3NiN and Mn_3SnN thin films have been reported before [33, 34], no such temperature dependence was found. A possible explanation is that the spin rotation is highly sensitive to small changes in the crystal structure. For Mn_3NiN there are conflicting reports of the exact phase transition temperature and in-plane spin angle as a function of temperature already in powder samples (see Chapter 4.2.2). More specifically, the NCAF phase is very sensitive to the sample composition. This poses a particular problem in the thin film fabrication of nitride samples, as the nitrogen content is very challenging to quantify accurately. Boldrin *et al.* quantify only the Mn:Ni ratio of their Mn_3NiN samples by energy-dispersive X-ray spectroscopy (EDX). You *et al.* did not report on any quantitative composition analysis of their MSN films. Moreover, they vary the nitrogen content in the films by changing the deposition conditions with the aim of varying the strain state of the sample. However, this approach has a conceptual error, as the chemical effect of varying the nitrogen content may be more significant than its effect on the strain state of the film. In contrast, in this work, RBS is employed for compositional analysis, which is a very accurate quantification technique. Using pyrolytic carbon substrates and with careful fitting of the spectra, this technique allows for quantification of the N content.

The presence of a NCAF phase in the MSN thin films discussed here is a conjecture based on compositional, structural, magnetic and magneto-transport measurements. Direct measurement of the NCAF structure is possible by neutron diffraction. Such experiments were performed by Nan *et al.* on Mn_3GaN samples [27]. It could be confirmed that Mn_3GaN has a the bulk-like [79] NCAF structure corresponding to Γ^{5g} configuration at all temperatures below T_N. In the case of MSN, however, because of the presence of a spin-rotational phase, the fitting procedure involved in the analysis of neutron diffraction data may be challenging. Therefore, probing the NCAF structure of antiperovskite nitrides through magneto-transport measurements, rather than neutron diffraction, is a much more practical approach.

Another important outcome of the transport measurements presented here is that the phase diagram of MSN is very different in bulk and thin films samples. Bulk MSN displays a rich phase diagram with collinear AF, NCAF and complex ferroic phases [see Figure 4.5 (p. 36)]. In both growth orientations, the low-temperature complex phases can be excluded as they exhibit significant magnetization in the bulk. For the (111)-oriented sample, in which no AHE is observed, it cannot be excluded that the samples are collinear AF at all temperatures. However, this is rather unlikely, as the collinear AF phase in bulk MSN is associated with a tetragonal distortion along the c-axis, which is not observed in the (111)-oriented samples. Therefore, it is plausible that the sample is in the NCAF phase at all temperatures, similar to the (001)-oriented sample and that the AHE is simply not detected because of the presence of equal amounts of compensating magnetic domains.

The transport measurements of (001)-oriented MSN provide conclusive evidence for the presence of NCAF order in this compound throughout the measurement range from 4 K to 400 K. In bulk MSN, all magnetic phase transitions are accompanied by crystallographic phase transitions. However, no phase transitions are found in any of the performed measurements in (001)-oriented MSN. Furthermore, a finite AHE is measured despite the vanishingly small magnetization. A similar magnetization does not result in an AHE in the (111)-oriented sample. The temperature dependence of the AHC in (001)-oriented MSN can, moreover, be modeled considering temperature-dependent spin rotation in the compound, as found in bulk powder samples. Thus, it can be concluded with high certainty that a NCAF phase is stabilized in MSN thin films over a much wider temperature range than in bulk material. This observation brings into question the applicability of established bulk phase diagrams of antiperovskite nitrides with NCAF structure to samples in thin films form.

The main open question concerns the non-zero AHE observed in (001)-oriented MSN despite the sample having cubic lattice metric. Previously, it was assumed that strain-induced tetragonal distortions lead to spin canting resulting in net moment coupled to the NCAF structure that allows for control of the magnetic domains. In the next chapter, it is shown through advanced XRD measurements that the Mn atoms are displaced away from high symmetry positions. These displacements drastically lower the crystal symmetry, but remain hidden when only probing the lattice metric of the films. Afterwards, the effect of the Mn displacements on the transport properties will be discussed in Chapter 9.

Chapter 8

Hidden Atomic Manganese Displacements

8.1 Lattice Strain in (001)-oriented Mn_3SnN

The measurements discussed in this chapter were performed using a six-circle diffractometer (SIXC) operated in z-axis mode [49], equipped with a gallium jet X-ray source operated at 70 keV and 100 W electron beam power. The wavelength of the emitted Ga-K_α radiation is $\lambda = 1.3414\,\text{Å}$. The beam was focused onto the sample using a Montel optics, which provides a highly collimated beam of 100 µm height and 2 mm width under an incidence angle of $\approx 1^\circ$. A liquid helium cryostat equipped with a beryllium dome was used for temperature-dependent XRD measurements. For the structural refinement, the integrated intensities of 17 symmetry-inequivalent reflections *hkl* (assuming tetragonal space group symmetry $P4/mmm$) were recorded.

Using the *Bruker* XRD system an out-of-plane lattice parameter of $c = 4.060(7)\,\text{Å}$ was found (see Chapter 6). Using the SIXC all lattice parameters can be measured to be $a = b = c = 4.06(1)\,\text{Å}$. This corresponds to a tetragonality of $c_{\text{MSN}}/a_{\text{MSN}} = 1.000(3)$. Therefore, the film can be considered to have cubic lattice metric within the margin of error of the measurement.

This is unexpected, given the large in-plane lattice mismatch of MSN and STO. In epitaxially grown cubic samples, the lattice mismatch of substrate and film is defined as

$$f = -\frac{\Delta a}{a_s} = \frac{a_f - a_s}{a_s} \tag{8.1}$$

and related to the mismatch biaxial strain as

$$\varepsilon_m = \frac{a_s - a_f}{a_s} = -f \tag{8.2}$$

In the case of MSN grown epitaxially on STO the lattice mismatch is $f = 3.9\,\%$. The resulting in-plane strain is

$$\varepsilon_{xx} = \varepsilon_{yy} = \varepsilon_m(1 - \nu) \tag{8.3}$$

wherein ν is the Poisson's ratio. As a result of volume conservation, this forces a change in the out-of-plane lattice parameter c_f by $\Delta c = c_s - c_f$. The relative changes in lattice parameter due to epitaxial strain are related to each other as [134]:

$$\frac{\Delta c/c_f}{\Delta a/a_f} = -\frac{2\nu}{1-\nu} \tag{8.4}$$

Assuming a Poisson's ratio of $\nu = 0.4$ [34], the expected out-of-plane lattice parameter for a lattice mismatch of 3.9 % is 4.19 Å. This corresponds to a tetragonality of 1.072, which is much larger than the value of 1.000(3) found in the real sample and which is well beyond the error margin of the measurement. Therefore, in the structural refinement presented in the following chapters, the lattice constants are fixed to the bulk value of 4.06 Å.

8.2 Structural Refinement Procedure

General Procedure For a given crystal, the X-ray scattering contribution of the unit cell as a function of the scattering vector $\boldsymbol{q}$ is described by the structure factor [43]:

$$F(\boldsymbol{q}) \propto \sum_{\alpha} f_\alpha \exp\left(-2\pi i \boldsymbol{q} \cdot \boldsymbol{r}_\alpha\right) \cdot T_\alpha^{\mathrm{H}}(\boldsymbol{q}) \tag{8.5}$$

Herein, the scattering contribution of each atom α at a position $\boldsymbol{r}_\alpha$ in real space is described by its atomic form factor f_α, which depends on the atomic number and the scattering angle. T_α^{H} is the Debye-Waller factor, which describes the harmonic (H) disorder. Whether the disorder is of thermal origin or due to statistical disorder can only be distinguished by temperature-dependent structural investigation. The Debye-Waller factor is described in terms of mean squared atomic displacement amplitudes U_α^{kl} $(k,l = 1,2,3)$:

$$T_\alpha^{\mathrm{H}}(\boldsymbol{q}) = \exp\left(-8\pi^2 U_\alpha^{kl} q_k q_l\right) \tag{8.6}$$

q_k, q_l are the components of $\boldsymbol{q}$ and the Einstein sum notation is used.

The intensity $I_{\mathrm{obs}}(hkl)$ measured in an XRD experiment is proportional to the real structure factor amplitude square:

$$I_{\mathrm{obs}}(hkl) \propto |F_{\mathrm{obs}}(hkl)|^2 \tag{8.7}$$

Structural refinement is performed in several iterative steps, as outlined in Fig 8.1. First, a structural model is assumed and a set of free fit parameters $a_1, ..., a_N$ is defined. The number of free fit parameters is limited by the number of measured reflections. These parameters are optimized by performing least squares refinement of the calculated to the

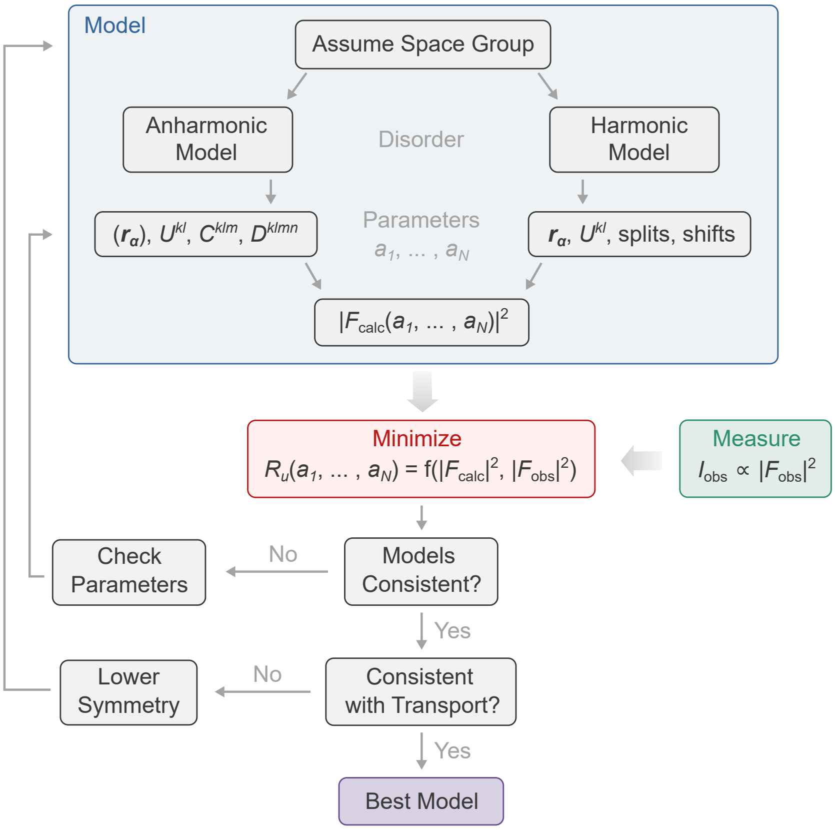
Model
Assume Space Group
Anharmonic Model
Disorder
Harmonic Model
(r_α), U^kl, C^klm, D^klmn
Parameters a_1, … , a_N
r_α, U^kl, splits, shifts
|F_calc(a_1, … , a_N)|^2
Minimize R_u(a_1, … , a_N) = f(|F_calc|^2, |F_obs|^2)
Measure I_obs ∝ |F_obs|^2
Check Parameters
No
Models Consistent?
Yes
Lower Symmetry
No
Consistent with Transport?
Yes
Best Model

Figure 8.1: Workflow of the structural refinement of antiperovskite nitride thin films presented here.

observed structure factor amplitudes [135]. The fit quality can be quantified by the unweighted residual R_u:

$$R_u(a_1,\ldots,a_N) = \frac{\sum_{hkl} \left| |F_{\mathrm{obs}}(hkl)|^2 - |F_{\mathrm{calc}}(hkl)|^2 \right|}{\sum_{hkl} |F_{\mathrm{obs}}(hkl)|^2} \tag{8.8}$$

R_u is a measure for the average relative disagreement of a given structural model with the experimental data. It is an absolute value and as such allows for direct comparison of different models. It is also very sensitive to which data is included in the refinement. Therefore, in this work all recorded and unweighted data is used for the refinement. A more meaningful measure from an error analysis point of view is the goodness of fit (GOF):

$$\mathrm{GOF} = \sqrt{\frac{1}{n-p} \sum_{hkl} \frac{|F_{\mathrm{obs}}(hkl) - F_{\mathrm{calc}}(hkl)|^2}{\sigma_{hlk}^2}} \tag{8.9}$$

where n is the number of measured reflections, p the number of free fit parameters and σ_{hkl} the measurement variance [136, 137]. The GOF has a value of unity when the discrepancies of the model with the data can be explained by experimental errors alone. A value greater than unity implies an inadequate model. Thereby, the GOF can be used to rule out wrong models. However, it cannot determine whether a model is right, as the data may be insufficiently good [137].

Anharmonic Corrections The Debye-Waller factor describes harmonic disorder of 2^{nd} order. To include anharmonicity in the structural models, the Debye-Waller factor can be expanded using a Gram-Chalier (GC) series development [138–140]. The corrected Debye-Waller factor is:

$$T_\alpha^{\mathrm{GC}}(\boldsymbol{q}) = T_\alpha^{\mathrm{H}}(\boldsymbol{q}) \left[1 + \frac{1}{3!}(2\pi i)^3 \cdot q_k q_l q_m \cdot C_\alpha^{klm} + \frac{1}{4!}(2\pi i)^4 \cdot q_k q_l q_m q_n \cdot D_\alpha^{klmn} \right] \tag{8.10}$$

The term in square brackets describes the deviation from the harmonic approximation parametrized by the anharmonic displacement parameters (ADPs) in the form of tensors of rank three (C_α^{klm}) and four (D_α^{klmn}). The structure factor including anharmonic contributions is then given by:

$$F^{\mathrm{GC}}(\boldsymbol{q}) = \sum_\alpha f_\alpha \exp\left(-2\pi i\, \boldsymbol{q} \cdot \boldsymbol{r}_\alpha\right) T_\alpha^{\mathrm{GC}} \tag{8.11}$$

Again, least squares refinement of R_u (Equation 8.8) is performed. However, the number of free fit parameters can be potentially much larger than in the harmonic case, because of the large number of independent ADPs. However, the point group symmetry at a given site greatly reduces the number of ADPs, as it defines which ADPs can be different from zero.

The Debye-Waller factor and the ADPs are defined in reciprocal space. To visualize the result of the structural refinement and specifically the physical significance of the ADPs, the Probability Density Function (PDF) is introduced, which is obtained from the Fourier transform of the Debye-Waller factor. Without anharmonic correction, the PDF is a trivariate Gaussian function:

$$\mathrm{PDF}^{\mathrm{H}}(\boldsymbol{u}) = \sqrt{\frac{\det\left(U_\alpha^{-1}\right)}{(2\pi)^3}} \exp\left(-\frac{1}{2}\boldsymbol{u}^T U_\alpha^{-1} \boldsymbol{u}\right) \tag{8.12}$$

The PDF is written as a function of the displacement vector $\boldsymbol{u}$ away from the site position $\boldsymbol{r}_\alpha$:

$$\boldsymbol{u} = \boldsymbol{r} - \boldsymbol{r}_\alpha \tag{8.13}$$

When anharmonic corrections are included, the PDF becomes:

$$\mathrm{PDF}^{\mathrm{GC}}(\boldsymbol{u}) = \mathrm{PDF}^{\mathrm{H}}(\boldsymbol{u}) \left[1 + \frac{1}{3!} C^{klm} H_{klm}(\boldsymbol{u}) + \frac{1}{4!} D^{klmn} H_{klmn}(\boldsymbol{u}) \right] \tag{8.14}$$

Here, $H(\boldsymbol{u})$ represent the Hermite polynomials [141], which are the 3^{rd} and 4^{th} order derivatives of the three-dimensional harmonic PDF to the components u_i of the displacement vector $\boldsymbol{u}$.

Chapter Outline In this chapter five different models within three different space group (SGR) symmetries are discussed. First, the bulk structure with SGR symmetry $Pm\bar{3}m$

(SGR No. 221) is assumed and it is found that it does not model the experimental data sufficiently well. Therefore, the symmetry is reduced to the tetragonal symmetry $P4/mmm$ (SGR No. 123). Two models are employed that yield consistent results. However, as will be outlined in Chapter 9, this symmetry is inconsistent with the finite AHE observed in (001)-oriented MSN. Therefore, the symmetry is reduced further to the non-centrosymmetric space group symmetry $P4mm$ (SGR No. 99). Again, two equivalent models are employed for structural refinement. Not only does this structure model the measured data better than any of the higher-symmetry structures, it is also consistent with the appearance of an AHE, which is discussed in Chapter 9.

8.3 Centrosymmetric Models

Starting point of the structural refinement is the bulk structure of MSN, shown in Figure 4.2(b), with cubic SGR symmetry $Pm\bar{3}m$, in which all Mn sites at the sites (0, $\frac{1}{2}$, $\frac{1}{2}$) are symmetry-equivalent (Wyckoff site 3c). The site symmetry forces the disorder to be harmonic and isotropic ($U^{11} = U^{22} = U^{33}$). The refined structural parameters are listed in Table 8.1. Using this simple and well established structure of bulk MSN, structural refinement yields a residual of $R_u = 16\,\%$. The GOF of the fit is 7.1, which is very high and which implies that $Pm\bar{3}m$ symmetry is insufficient to describe the real structure of (001)-oriented MSN.

Table 8.1: Refined structural parameters derived from least squares refinement of the bulk structure of Mn_3SnN with space group symmetry $Pm\bar{3}m$ to XRD data obtained from a 20 nm thin MSN film at 300 K. Numbers in brackets represent (1σ) uncertainties with respect to the last digit. Parameters marked with asterisks are fixed.

Model	Bulk Mn_3SnN structure		
SGR	$Pm\bar{3}m$		
Lattice	$a = b = c = 4.06\,Å$		
Residual	$R_u = 0.16$		
Goodness	GOF = 7.10		
Site	Mn (3c)	Sn (1a)	N (1b)
Position*	($\frac{1}{2}$, $\frac{1}{2}$, 0)	(0, 0, 0)	($\frac{1}{2}$, $\frac{1}{2}$, $\frac{1}{2}$)
Occupation*	1.0	1.0	1.0
U^{11}(Å^2)	0.0720(8)	0.077(1)	0.025*
U^{22}(Å^2)	0.0720(8)	0.077(1)	0.025*
U^{33}(Å^2)	0.0720(8)	0.077(1)	0.025*

Thin films of cubic materials commonly show tetragonal distortion, i.e., an elongation or contraction along the c-axis. However, it is found here that the film has cubic lattice metric within the error margin of the measurement. Nevertheless, the symmetry can be lower due to anharmonic or anisotropic disorder. Therefore, the structural model is refined by reducing the assumed symmetry to allow for this kind of disorder. The condition $a = b = c = 4.06\,Å$ is set and the overall symmetry reduced to space group symmetry

$P4/mmm$ (SGR No. 123). The Sn atom is assumed to display harmonic, anisotropic disorder. The two Mn sites are inequivalent in this SGR and denoted $\mathrm{Mn_I}$ (basal plane atom at $z = 0$) and $\mathrm{Mn_{II}}$ (at $z = 1/2$).

The centrosymmetric (CS) SGR symmetry $P4/mmm$ preserves the 4-fold rotational symmetry around the c-axis, but breaks it along the a- and b-axis. It also breaks the three-fold improper rotation around the [111] axis. For the atomic displacements amplitudes, one finds $U^{11} = U^{22} \neq U^{33}$. Furthermore, certain 4th order ADPs are now allowed to be non-zero. At these sites the following ADPs are additionally refined: $D^{1111} = D^{2222} \neq D^{3333}$. On the other hand, none of the 3rd order ADPs C^{klm} are allowed to be non-zero. The anharmonic disorder is then visualized by calculating the PDFs at the two Mn sites using Equation 8.14.

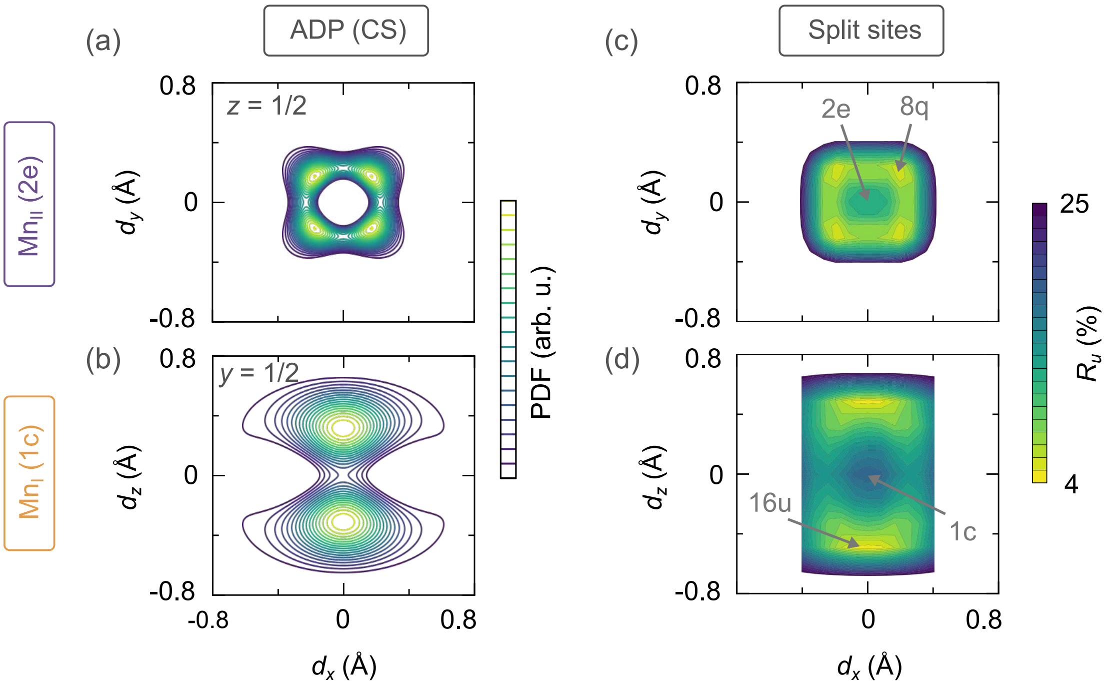

Figure 8.2: Results of refinement of model structures with space group symmetry $P4/mmm$ (SGR No. 123) using two different models. (a), (b) Centrosymmetric (CS) Atomic Displacement Parameter (ADP) model: Sections of the Probability Density Functions (PDFs) at the 2e and 1c sites showing pronounced 4-fold and 2-fold distribution of the PDFs. (c), (d) Split-sites model: Color maps of the residual R_u when varying the site positions.

Sections of the PDFs along certain planes are presented in Figures 8.2(a) and (b). In the presented plots, only positive values of the PDFs are plotted. It can be seen that the atomic disorder is very different at the two Mn sites at $z = 0$ (Wyckoff site 1c in $P4/mmm$) and $z = \frac{1}{2}$ (2e site). At both sites, multi-model distributions of the disorder can be found, which can be interpreted as a static 2-fold (at 1c) and 4-fold (at 2e) splitting of the atomic sites. Thereby, $\mathrm{Mn_I}$ atoms at the 1c site are statistically displaced upwards or downwards along the c-axis. Equivalently, $\mathrm{Mn_{II}}$ atoms at the 2e site are displaced within the plane at $z = \frac{1}{2}$. A schematic representation of the crystal structure with displaced Mn atoms is shown in Figure 8.3(a).

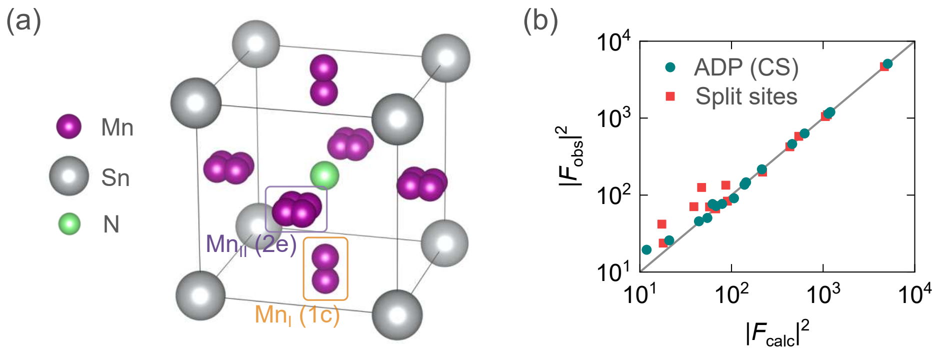

Figure 8.3: (a) Graphical representation of the crystal structure derived from refinement of the centrosymmetric model structures with $P4/mmm$ SGR symmetry. The size of the Mn atoms is reduces compared to images above for clarity. (b) Observed versus calculated squared structure factor amplitudes of 17 symmetry-inequivalent Bragg peaks.

To give more insight into the fit quality, Figure 8.3(b) shows a plot of the observed versus the calculated squares of the structure factor amplitudes. According to Equation 8.7, the measured intensity is proportional to $|F_{\mathrm{obs}}(hkl)|^2$. F_{calc} is calculated for the centrosymmetric (CS) ADP model as well as for the split-sites model (discussed below) using Equation 8.5. The scaling factor is also a fit parameter. It can be seen that there is a clear linear correlation of the observed and calculated values, which reflects the low residual of $R_u = 0.6\,\%$ obtained with the CS-ADP model. This value is significantly smaller than the value obtained when assuming the bulk structure of MSN of $R_u = 16\,\%$, which indicates that the Mn displacements are a real feature of the crystal and not a spurious result of the fitting.

Nevertheless, to further test this hypothesis, another model is employed, in which the Mn atoms are again restricted to display harmonic disorder, but the sites are split into symmetry-equivalent sub-sites. The 2e sites is split into 4 sites at Wyckoff positions 8q (in SGR $P4/mmm$) at $(x,\ y,\ \frac{1}{2})$, each occupied with a probability of 1/4. The 1c site is split into 16 sites at Wyckoff position 16u at $(x,\ y,\ z)$, each occupied with a probability of 1/16. The lowest residual that can be achieved within this model is $R_u = 4\,\%$, which is significantly lower than in the case of the cubic bulk structure, but not as low as for the CS-ADP model.

Figures 8.2(c) and (d) show maps of R_u as a function of the position of the 8q and 16u sites near the high-symmetry 2e and 1c sites. Qualitatively, the same results as in the CS-ADP model are found. The 8q sites fall into four distinct minima of R_u, corresponding to the 4-fold splitting of the site shifted away by $\approx 0.2\,\text{Å}$ in x- and y-direction. At the 1c site, the 16u sites fall into two distinct minima of R_u shifted away from 1c by $\approx \pm 0.45\,\text{Å}$.

On the basis of the low residual values obtained using the CS-ADP and the split-sites model as well as the good qualitative agreement of the two models the structural investigation could be concluded at this point. However, the centrosymmetry enforced by the choice of space group symmetry $P4/mmm$ conflicts with the observation of a finite AHE described in the previous chapter. While the detailed discussion is postponed to

Chapter 9, it should suffice at this point to state that a further symmetry reduction is required to explain the transport signals measured in the MSN films.

8.4 Non-centrosymmetric Models

8.4.1 Structural Refinement

In order to have a structural model consistent with a finite AHE, the mirror symmetry along the c-axis, along which the magnetic field is applied, must be broken. $P4/mmm$ has $4/m$ symmetry along [001], i.e a four-fold symmetry with a mirror plane perpendicular to the rotation axis. If $4/m$ is reduced to 4, then this also reduces the symmetry along the other two axes, $\langle 100\rangle$ and $\langle 110\rangle$, from $2/m$ to m. Thereby, the reduced space group symmetry becomes $P4mm$ (SGR No. 99). This SGR is acentric and a highest-order non-isomorphic subgroup of $P4/mmm$.

In $P4mm$, more ADPs are allowed to be non-zero. Most importantly, there are now components that are symmetrically odd with respect to the c-axis, such as C^{333}. Employing a non-centrosymmetric (NCS) ADP model with this $P4mm$ space group symmetry allows to obtain the best fit to the measured data out of all the presented models. A residual as low as $R_u = 0.019\,\%$ could be achieved. The refined parameters that yield this extraordinarily low residual are presented in Table 8.2. Comparison with Table 8.1 shows that many more parameters have to be refined, as compared to the simple cubic model. In fact, the number of free parameters reaches the limit set by the number of recorded reflections. Nevertheless, the GOF is 0.46 and, therefore, greatly reduced compared to the cubic bulk structure model with fewer fit parameters.

In contrast to the CS-ADP model based on $P4/mmm$ SGR symmetry, the $\mathrm{Mn_I}$ atom resides at Wyckoff site 1b (formerly 1c) and the $\mathrm{Mn_{II}}$ atom at site 2c (formerly 2e). The 1b site ($\frac{1}{2}$, $\frac{1}{2}$, z) is allowed to vary along z, while the 2c site is fixed at $z = \frac{1}{2}$. The 1b site shifts to positive $z = 0.038$. When computing the PDF at this site using Equation 8.14, one has to consider that the PDF is defined as a function of the displacement $\boldsymbol{u}$ away from the site position $\boldsymbol{r}_\alpha$. In order to compare the results of the NCS-ADP model with those of the shifted-sites model discussed below, the PDFs at both Mn sites are plotted in Figures 8.4(a) and (b) as a function of distance d_i ($i = x,y,z$) from the face centers at $(0,\frac{1}{2},\frac{1}{2})$ and $(\frac{1}{2},\frac{1}{2},0)$, respectively. Note that in the case of the CS-ADP model with $P4/mmm$ symmetry, $d_i = u_i$.

The most striking difference between the NCS- and the CS-ADP model is that in the NCS case, the $\mathrm{Mn_I}$ atom appears to not be split, but rather merely shifted to negative z-values. This change can be attributed to the appearance of a non-zero ADP C^{333}. To test this hypothesis, again an alternative model is employed, in which the atoms display harmonic disorder, but the 1b site is allowed to vary in all direction. In this shifted-sites model, this corresponds to optimizing the positional parameters of a Mn atom at Wyckoff site 4f (x,y,z). The 2c site is again split into four symmetry-equivalent sub-sites

Table 8.2: Refined structural parameters derived from least squares refinement of the NCS ADP model. Numbers in brackets represent (1σ) uncertainties with respect to the last digit. Parameters marked with asterisks are fixed.

Model	NCS-ADP model			
SGR	$P4mm$			
Lattice	$a = b = c = 4.06\,\text{Å}$			
Residual	$R_u = 1.9 \times 10^{-4}$			
Goodness	GOF = 0.46			
Site	Mn (1b)	Mn (2c)	Sn (1a)	N (1b)
Position	$(\frac{1}{2}*, \frac{1}{2}*, 0.04(1))$	$(0, \frac{1}{2}, \frac{1}{2})*$	(0, 0, 0)*	$(\frac{1}{2}, \frac{1}{2}, \frac{1}{2})*$
Occupation*	1.0	1.0	1.0	1.0
$U^{11}(\text{Å}^2)$	0.047(5)	0.039(2)	0.0385(8)	0.025*
$U^{22}(\text{Å}^2)$	0.047(5)	0.039(2)	0.0385(8)	0.025*
$U^{33}(\text{Å}^2)$	0.17(4)	0.23(4)	0.28(5)	0.025*
C^{333} (×10³)	3.9(9)	5.0(7)		
C^{113} (×10³)	2.2(8)			
C^{223} (×10³)	2.2(8)			
D^{1111} (×10⁴)	0.43(9)	−0.34*		
D^{2222} (×10⁴)	0.43(9)	−0.34*		
D^{3333} (×10⁴)	−7(2)	1(1)		
D^{1122} (×10⁴)	−0.19(2)			

at Wyckoff site 8g. The maps of the resulting fit residual as a function of site position are presented in Figure 8.4(c) and (d).

The site splitting of the Mn_{II} atom is preserved in this model. At the 1b site, the interpretation is more complex. There are two minima of R_u at negative d_z. However, the local maximum between the two, which corresponds to the 1b site at negative z is only slightly higher in R_u. Therefore, this additional local splitting may be a result of the harmonic picture not being able to capture the pronounced disorder in the xy-plane properly. For simplicity, and in agreement with the NCS-ADP model, it is assumed that there is no additional splitting of the 1b site in the xy-plane. However, an additional minimum of R_u can be observed at positive d_z values. In fact, this indicates that there is also a site splitting at the 1b site, similar to the split-sites model in the CS case, but with the site occupation being unequal at the two sub sites. This may be supported also by the NCS-ADP model, as discussed further in Section 8.5.

It was attempted to improve the model by considering two 4f sites near 1b with unequal occupation and refining the site positions and occupations. However, this model does not converge, but tends to set the site occupation at the upper site to 0 or, else, move both sites to the one at negative z values. This effect may be a result of the additional maximum at positive z-values near the 1b site being indeed an artifact.

Therefore, the model is simplified by considering only one Mn_{I} atom at site 1b shifted to negative z and a four-fold splitting of the Mn_{II} atom at 2c. A graphical representation

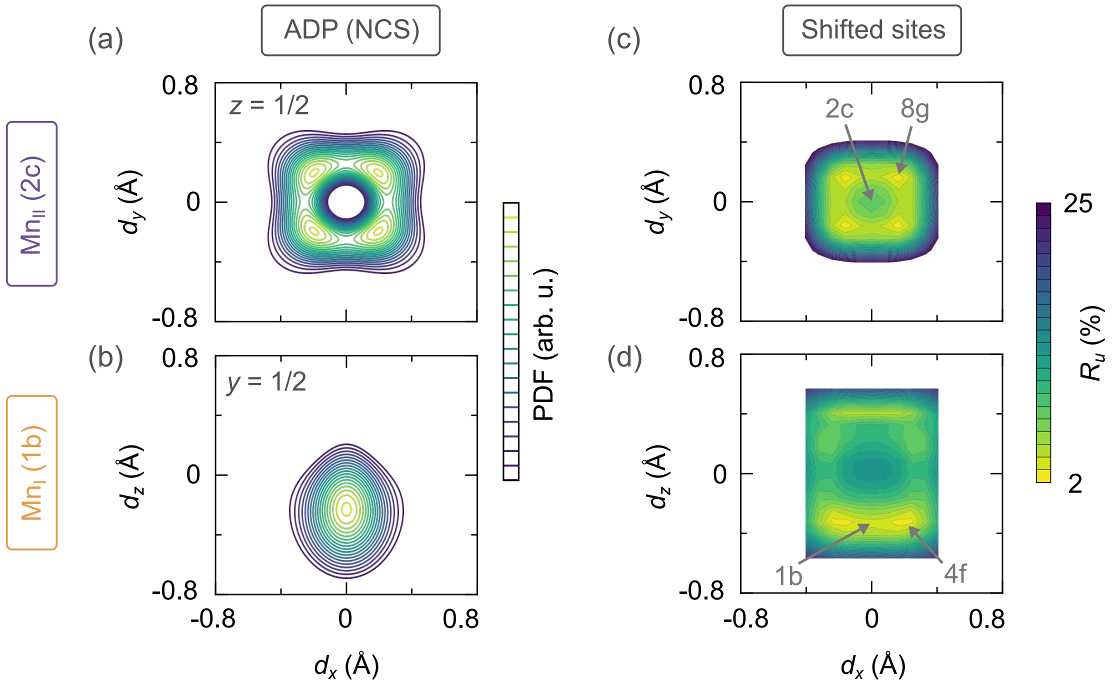

Figure 8.4: Results of refinement of model structures with space group symmetry *P*4*mm* (SGR No. 99). (a), (b) Sections of the Probability Density Functions (PDFs) at the 2c and 1b sites within the non-centrosymmetric (NCS) Atomic Displacement Parameter (ADP) model. (c), (d) Shifted-sites model: Color maps of the residual R_u when varying the site positions.

is presented in Figure 8.5, which, in comparison to Figure 8.3(a) highlights that the shift of the basal plane Mn atom, in contrast to the splitting in the CS case.

8.4.2 Temperature and Thickness Dependence

The shifted-sites model also allows to quantify the magnitude of the Mn displacements at the two sites. To that end, XRD measurements were performed using a liquid He cryostat equipped with a Beryllium dome at temperatures between 4 K and 400 K and the data was refined to the shifted-sites model. As can be seen from Figure 8.5(b), the magnitude of the Mn displacements shows only a small temperature dependence. At both sites, the displacements persist at low temperatures, which confirms that the anharmonic disorder it static in nature (rather than dynamic, through thermal effects, for instance). The figure also shows the temperature dependence of the fit residual R_u. The error bars are not calculated from the residual. Instead, they are estimated from the contour plots in Figure 8.4. The change of R_u from one colored region into the next is quite large with about 1 percentage point. Therefore, the width of the region with minimum $R_u \approx 2\,\%$ can be considered as the uncertainty of the displacement magnitude corresponding to a deviation of R_u of 1 percentage point. Within the error bar, the displacement magnitude of the Mn$_{\mathrm{I}}$ atom is temperature-independent. For the Mn$_{\mathrm{II}}$ atom there is a small increase in displacement magnitude with increasing temperature, which can be attributed to thermal effects. The temperature-dependent XRD measurements again show no sign of any crystallographic phase transition in the entire measurement range.

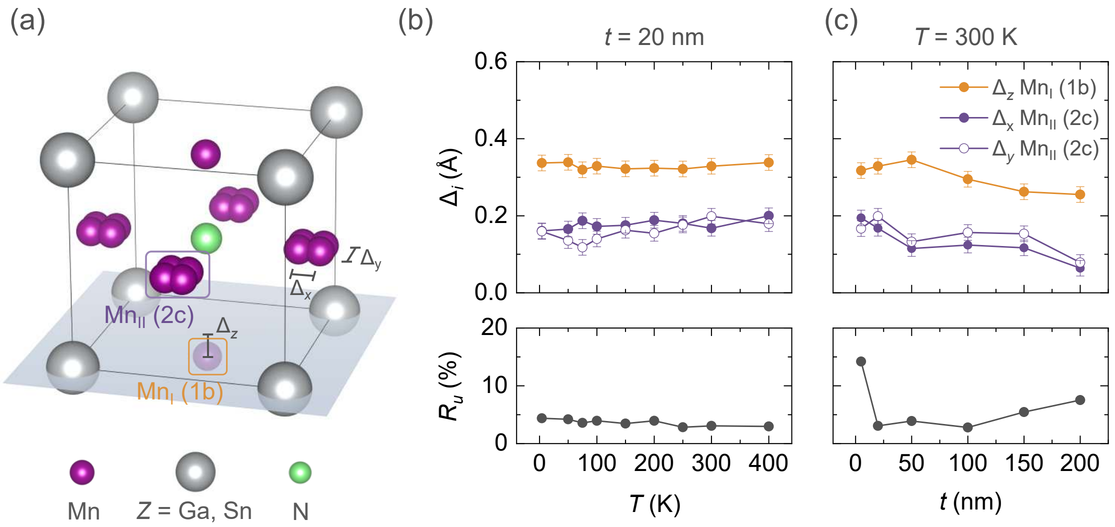

Figure 8.5: (a) Graphical representation of the crystal structure derived from refinement of the non-centrosymmetric model structures with *P*4*mm* SGR symmetry. The basal (001) plane at $z = 0$ is highlighted in gray. (b), (c) Displacement magnitude (top row) and fit residuals (bottom row) at the Mn 1b and 2c site as a function of (b) temperature for a 20 nm film and (c) film thickness at 300 K.

Furthermore, MSN samples of varying film thickness from 5 nm to 200 nm were grown on STO and investigated by XRD at 300 K. The thickness dependence of the displacement magnitudes is plotted in Figure 8.5(c). A general trend of decreasing displacement with increasing thickness is observed. This is expected, as the film structure is expected to become more bulk-like at large film thicknesses. It also suggests that the Mn displacements are induced by substrate strain. The film thicknesses at which the displacements are expected to vanish can be estimated by extrapolation of the data to high film thicknesses. The displacements at both sites are expected to vanish at a film thickness of about 500 nm.

Interestingly, the largest displacements are not observed in the thinnest film, but at a thickness of 50 nm. Assuming that the displacements are strain-induced, this may be explained by an accumulation of stress in the film up to a certain thickness, above which the formation of misfit dislocations is favored [38].

From Figure 8.5(c) it can also be seen that R_u increases, i.e. the fit quality decreases, at higher film thicknesses. This may result from the film structure approaching the bulk structure with no Mn displacements. Similarly, R_u is drastically increased in the 5 nm thin film, reaching a value as high as 14 %. This indicates that the model is insufficient to describe the real crystal structure of very thin films. This is expected, as in thinner films the scattering contributions of the first few atomic layers closer to the interface to the scattering amplitude become more prominent. It is likely that the atomic structure closer to the interface is different than from the bulk of the film, because of the large lattice mismatch of substrate and film. The resulting stress appears to be fully relaxed in films of 20 nm thickness. However, at lower film thicknesses, the atomic structure may be different than in the bulk of the film. Quintela *et al.* found Mn-deficient atomic layers at the interfaces of Mn_3GaN with STO and LSAT substrates, which they attribute to a charge imbalance of the two materials [127]. It is possible that a similar effect occurs in Mn_3SnN in conjunction with the formation of Mn displacements.

8.4.3 Summary of Structural Models

To conclude the main part of this chapter, Table 8.3 summarizes the presented structural models and the resulting fit quality. In the next section, further details concerning the PDFs at the two Mn sites are discussed, which are interesting from the viewpoint of structural refinement of thin film data.

Table 8.3: Summary of the structural models employed in the refinement of XRD data of (001)-oriented Mn_3SnN. Mn_I and Mn_{II} are Mn atoms near high-symmetry sites at $z = 0$ and $z = \frac{1}{2}$, respectively. Structural disorder can be harmonic (H) or anharmonic (AH) as well as isotropic (I) or anisotropic (AI). In all models, the lattice parameters are $a = b = c = 4.06\,\text{Å}$.

Model	SGR	Mn sites		Disorder			R_u (%)
		Mn_I	Mn_{II}	Mn	Sn	N	
Cubic	$Pm\bar{3}m$	3c		H, I	H, I	H, I	16
ADP-CS	$P4/mmm$	1c	2e	AH, AI	H, AI	H, I	0.6
Split-sites		16×16u	4×8q	H, I	H, I	H, I	4
ADP-NCS	$P4mm$	1b	2c	AH, AI	H, AI	H, I	0.019
Shifted-sites		1×4f	4×8g	H, I	H, I	H, I	2.4

8.5 Interpretation of the Probability Density Function

In the last section, a simplified structural model based on the non-centrosymmetric SGR $P4mm$ is given, which is consistent with structural refinement using anharmonic and harmonic displacement parameters as well as with the magneto-transport measurements (see Chapter 9). Nevertheless, in the following, the PDFs at the two Mn sites are discussed in more detail.

First, it is noted that the PDFs plotted in Figures 8.4(a) and (b) are simplified in order to highlight the physically relevant features of the PDFs. Specifically, only positive PDF values are plotted in the figures. With reference to Equation 8.14, the PDF can have negative values, which, however, have no physical meaning [142]. Instead, they result from truncation errors, as the PDF is the Fourier transform of the generalized Debye-Waller factor in reciprocal space (Equation 8.10). As such, truncation errors may arise due to the disorder being described only up to 4th order, especially in the presence of strong gradients of the PDF in real space.

Figure 8.6(a) shows the PDF at the 4-fold symmetrically split 2c site viewed along the y-axis. In this view, the maximum PDF is not found at $u_z = 0$, i.e., at $z = \frac{1}{2}$. Instead, it is shifted towards negative u_z, similar to the 1b site. It can also be seen that at positive u_z the PDF is strongly negative (dashed lines). However, large negative PDFs are unphysical

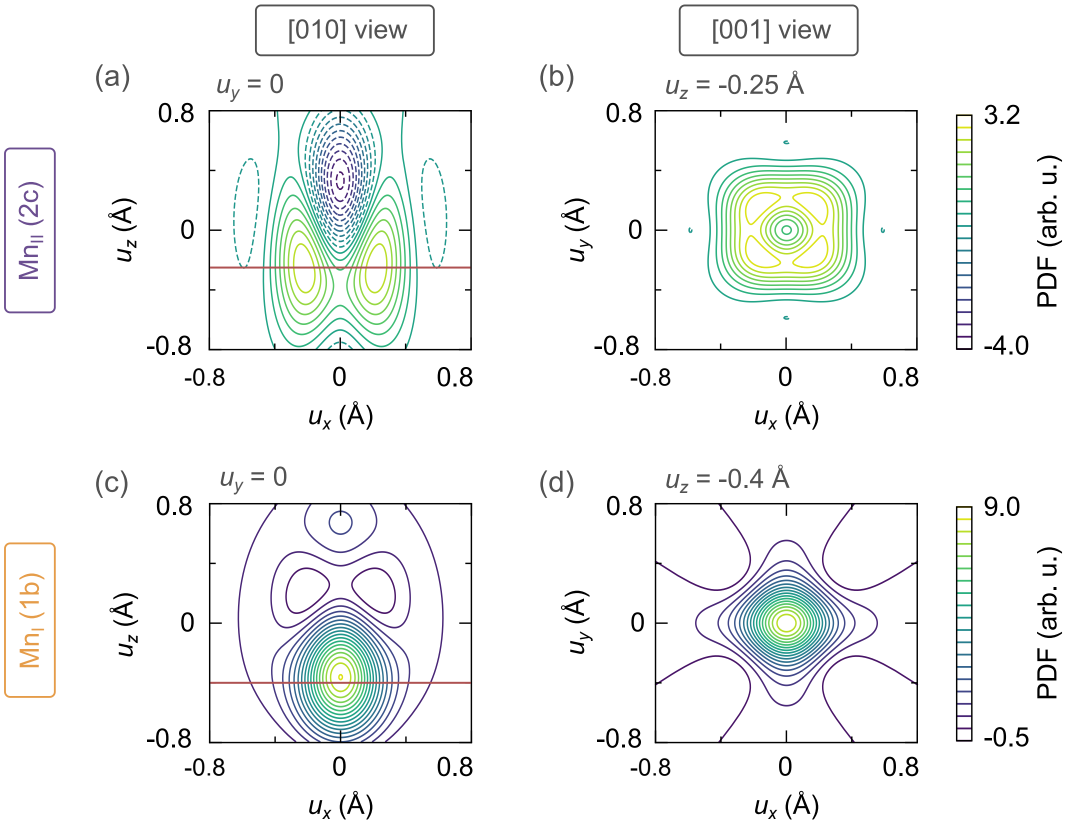

Figure 8.6: Additional sections of the PDFs at the 2c site (top row) and 1b site (bottom row) within the non-centrosymmetric ADP model. In each row, the figures share a common color bar, shown in (b) and (d), respectively. Negative PDF values are shown as dashed lines. (a), (c) Views along the [010] direction of the xz-planes at $u_y = 0$, i.e., at $y = 0$ and $y = \frac{1}{2}$, respectively. Red lines indicate the positions of the xy-sections presented in the right column figures. (b), (d) Views along the [001] direction of the xy-planes at $u_z = -0.25\,\text{Å}$ and $u_z = -0.4\,\text{Å}$, respectively. Red arrows indicate the direction of the elongation of the PDFs at the different sites.

and this effect is considered an artifact [142]. This justifies restricting the 2c site to lie within the xy-plane at $z = \frac{1}{2}$.

Figure 8.6(b) shows the PDF at the 2c site in the same view as in Figure 8.4(a), but at $u_z = -0.25\,\text{Å}$. Note that Figures 8.6(a) and (b) share the same color bar. Again, the pronounced 4-fold splitting of the 2c site can be observed, in agreement with the harmonic shifted-sites model.

Considering the PDF at the 1b site, presented in Figure 8.6(c), the only difference compared to Figure 8.4(b) is the appearance of a low but positive PDF at positive u_z values. This feature is not shown in the previous chapter, as it is unclear whether it has physical significance. Given the second minimum of R_u in the shifted-sites model in Figure 8.4(d), this second maximum in the PDF may reflect the presence of a minority site at positive u_z values. However, as it has no impact on the interpretation of the transport data, this feature is not considered in the structural model. Lastly, Figure 8.6(d) shows a section of the PDF in the xy-plane at $u_z = -0.4\,\text{Å}$, i.e., at the maximum of the PDF at the 1c site. Here, the effect of the ADP D^{1122} in constricting the PDF in-plane along the $\{110\}$ directions becomes apparent.

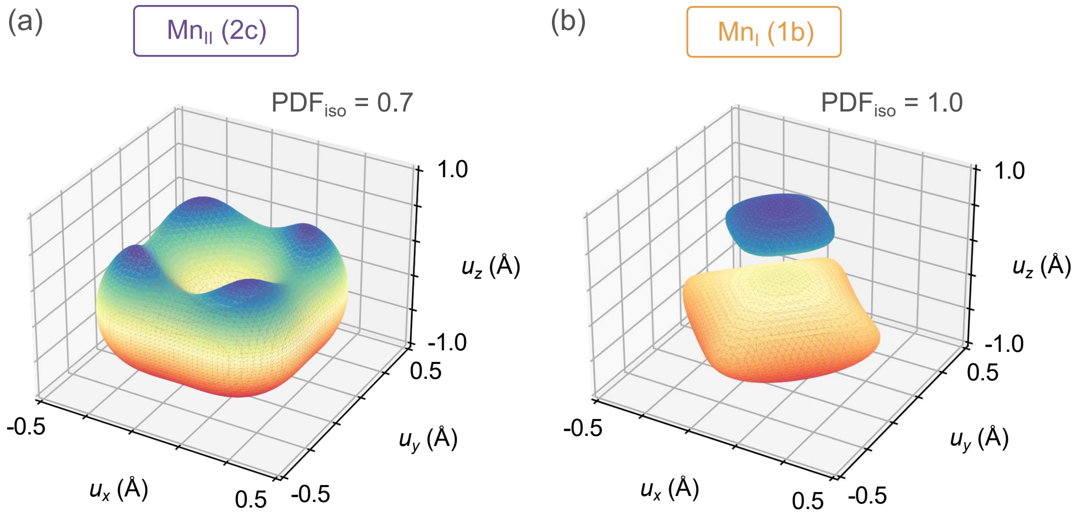

Figure 8.7: Isosurface plots of the PDFs within the NCS-ADP model at the Mn sites in SGR *P*4*mm* (a) 2c with PDF isosurface value of 0.7 and (b) 1b with $\mathrm{PDF_{iso}}$ of 1.0.

Another way to visualize the atomic disorder represented by the PDFs is through three-dimensional isosurface plots at fixed PDF values. This is shown for two different PDF values at the Mn 2c and 1b sites in Figure 8.7. Again, the most important structural features can be observed, namely the four-fold splitting of the $\mathrm{Mn_{II}}$ atom and the shift of the $\mathrm{Mn_{I}}$ atom toward negative u_z values.

This concludes the discussion of the formation of Mn displacements in MSN, resolved by structural refinement of XRD data of MSN thin films. In the following, it is discussed how the results of the magneto-transport measurements presented in Chapter 7 and the structural investigations presented in this chapter are related to each other. Specifically, it will be shown how the presence of atomic Mn displacements can explain the observation of a non-zero AHE in MSN thin films, despite their cubic lattice metric.

Chapter 9

Resolving the Anomalous Hall Effect in Mn_3SnN

9.1 Magneto-structural Coupling and Spin Canting in Antiperovskite Nitrides

Manganese-based antiperovskite nitrides exhibit pronounced coupling of crystal and magnetic structure. From Figure 4.3 (p. 33) it can be seen that most antiperovskite nitrides exhibit non-collinear antiferromagnetic (NCAF) phases with triangular spin textures only if their crystal structure is cubic. Tetragonal crystal structures, on the other hand, are associated with other types of magnetic order. Antiperovskites are also very sensitive to external stimuli as regards their crystal and magnetic structure. For example, in Mn_3NiN the first-order cubic-to-cubic crystallographic phase transitions at the Néel temperature are accompanied by a strong lattice expansion with decreasing temperature, leading to negative thermal expansion coefficients [99, 100, 143–148]. In some cases this leads to low temperature coefficient of the electrical resistivity as well [149, 150]. Another consequence of the strong coupling of magnetism and lattice is the coupling of the lattice to external magnetic field, which results in pronounced magnetostriction and shape-memory effects [151–153]. Furthermore, as phase transitions are associated with latent heat, the magneto-structural coupling entails magneto-caloric effects across phase transitions [154]. Similarly, externally applied pressure induces changes in the magnetization (baromagnetic effects) [155] and in latent heat (barocaloric effect) [101, 156, 157].

Many of the described effects observed in bulk material have counterparts in thin films. Most importantly, a two-dimensional equivalent of the baromagnetic effect is piezomagnetism, in which the application of (biaxial) strain leads to the emergence of a net magnetization. This effects was studied theoretically in several cubic NCAFs [118, 123, 134, 158, 159]. Piezomagnetism was further investigated experimentally in Mn_3NiN thin films by Boldrin *et al.* [160, 161]. Mn_3NiN thin films were grown on different perovskite oxide substrates. The different lattice mismatches between substrates and film led to films with compressive or tensile biaxial strain. By varying the substrate material, other effects that could affect the magnetization could be excluded. In contrast, in another work on Mn_3SnN, You *et al.* varied the nitrogen content rather than the substrate material [34]. Although this is likely to change the strain state due to a change in lattice constants, it stands to reason that the altered material chemistry itself directly affects the spin texture and the measured magnetization. Furthermore, in that work, the film composition was not quantified. Similarly, Boldrin *et al.* report only on the Mn to Ni ratio of their Mn_3NiN films as quantified by energy-dispersive X-ray spectroscopy (EDS) [160]. Therefore, chemical effects cannot be excluded in those Mn_3NiN films.

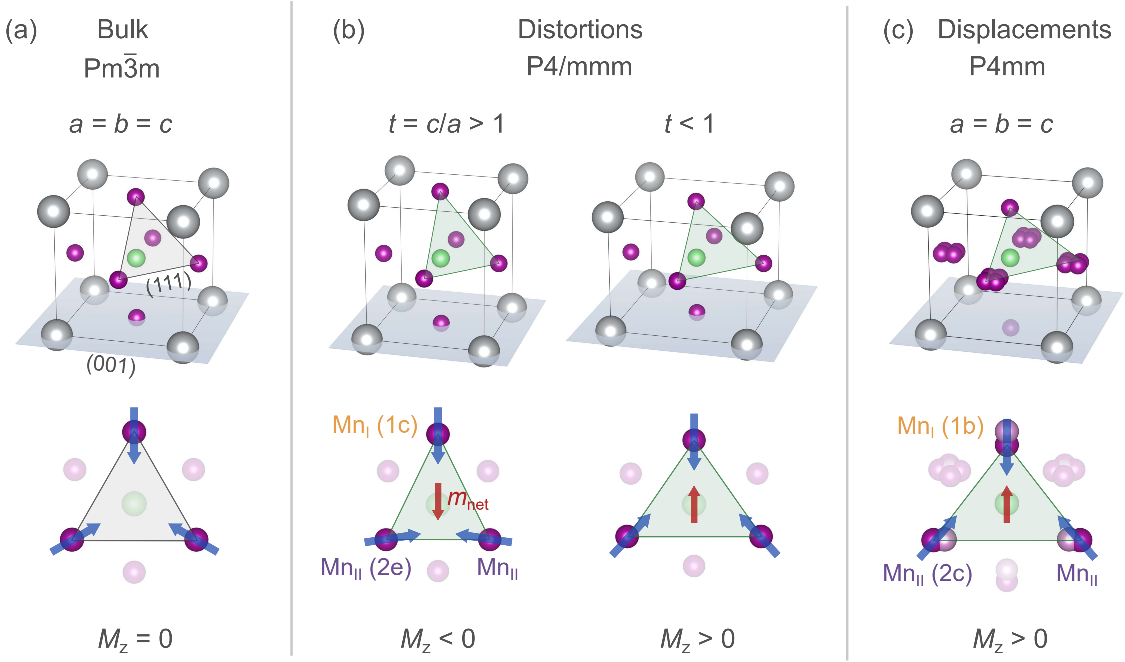

Figure 9.1: Model structures to illustrate the emergence of canted moments in samples with tetragonal distortions and Mn displacements. (a) In the cubic bulk structure the Γ^{4g} spin texture is fully compensated (bottom row, viewed along [111] with spins shown in blue). In contrast, (b) compressive or tensile tetragonal distortions or (c) atomic Mn displacements lead to the emergence of net moments (shown in red).

Figure 9.1 illustrates how symmetry lowering from cubic to tetragonal in the form of tetragonal distortions can lead to the appearance of a net magnetization. In the cubic antiperovskite bulk structure with $Pm\bar{3}m$ SGR symmetry, the Mn atoms form equilateral triangles on the (111) Kagome plane, as highlighted in light gray. The spin residing on the Mn sites are antiferromagnetically coupled. This configuration is a textbook example of a geometrically frustrated system of three spins [64, 65] and, in the case of many cubic NCAFs, leads to the emergence of trigonal spin textures such as the one corresponding to the Γ^{4g} configuration shown in Figure 9.1(a), for example. The spins exactly compensate each other and the net magnetization is zero. In this case, the magnetic texture is insensitive to magnetic field.

Next, the case of biaxially-strained films is considered. In epitaxially grown cubic samples, the in-plane lattice parameter of the film a_f is forced to be equal to that of the substrate a_s. There are two commonly accepted mechanisms for strain relaxation in epitaxial thin films: misfit dislocations and tetragonal distortion [38]. If $a_f > a_s$, the film is compressively strained, often resulting in a tetragonal elongation characterized by $t = c_f/a_f > 1$. If $a_f < a_s$, it is tensile strained leading to tetragonal distortion with $t < 1$. Tetragonal distortions reduce the crystal symmetry from $Pm\bar{3}m$ to the highest-order non-isomorphic subgroup $P4/mmm$. Both cases of tetragonal distortion are schematically shown in Figure 9.1(b). Taking the case $t < 1$ as an example, it can be seen that the distance of the $\mathrm{Mn_I}$ atom to the two $\mathrm{Mn_{II}}$ atoms is reduced. The Kagome plane is distorted and the Mn atoms form an isosceles triangle (highlighted in green). As a result, the antiferromagnetic exchange between the $\mathrm{Mn_I}$ and the $\mathrm{Mn_{II}}$ atoms is larger than between the $\mathrm{Mn_{II}}$ atoms, leading to a canting of the $\mathrm{Mn_{II}}$ spins towards the $\mathrm{Mn_I}$ atom. The three spins no longer exactly compensate each other, thus leading to the emergence of a net magnetization in the [-1-12] direction with z-component along the crystallographic c-axis of $M_z > 0$ (highlighted in red). The direction of the net moment also depends on the details of the spin configuration. When the magnetic texture is in the Γ^{5g} configuration instead of the Γ^{4g} configuration, the net moment points along the [110] direction.

The magnitude of the net magnetization is relatively low; it was calculated to be around $0.04\,\mu_\mathrm{B}/\mathrm{f.u.}$ at 1 % strain in $\mathrm{Mn_3NiN}$ and $\mathrm{Mn_3GaN}$ [118, 134]. In $\mathrm{Mn_3NiN}$ films grown by Pulsed Laser Deposition (PLD) a magnetization of up to around $0.15\,\mu_\mathrm{B}/\mathrm{f.u.}$ at −0.3 % strain was measured [160]. However, it should be noted that already the PLD target used for thin film fabrication showed a magnetization of around $0.04\,\mu_\mathrm{B}/\mathrm{f.u.}$

Through the structural refinement discussed in the previous chapter, it is found in this work that the crystal structure of $\mathrm{Mn_3SnN}$ thin films is characterized not by tetragonal distortion, but by displacements of the Mn atoms away from high symmetry position that lower the space group symmetry to $P4mm$, despite the lattice metric appearing as cubic within the measurement error. Figure 9.1(c) exemplifies how Mn displacements can also lead to the emergence of net moments. Because of the statistical four-fold splitting of the $\mathrm{Mn_{II}}$ atom, the description is more complex than in the case of tetragonal distortions. The exact orientation and magnitude of the net moment due to canting depends on the local site occupation in a given unit cell.

To confirm the hypothesis of displacement-induced spin canting, model spin density functional theoretical calculations were performed.[1] The calculations were performed using a first-principles full relativistic Green function method [162, 163] within the density functional theory in a generalized gradient approximation [164]. This functional adequately reproduces the electronic and magnetic properties of the given compound. The model crystal structure was adopted from the results obtained from structural refinement presented in the previous chapter. The magnetic structure of the system and magnetic interactions were determined using the frozen magnon approximation and the magnetic force theorem, implemented within the multiple scattering theory [163, 165, 166]. In the ground state the magnetic moments were found to form an antiferromagnetic structure with a Néel temperature of 450 K, obtained within a random phase approximation [167].

---

[1] The fruitful collaboration with Arthur Ernst at Johannes Kepler University Linz is greatly appreciated.

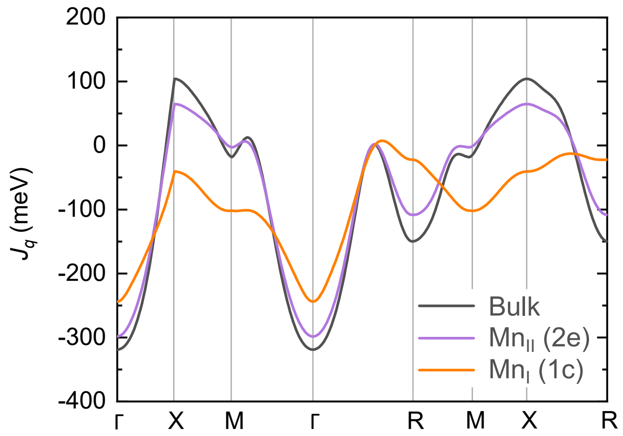

Figure 9.2: The lattice Fourier transform of the exchange interactions $J(\boldsymbol{q})$ in Mn_3SnN in the case of the cubic bulk structure and with Mn displacements at the 2e ($z = 1/2$) and 1c ($z = 0$) site. The maximum of J corresponds to the total energy minimum and determines the ordering vector of the magnetic structure.

The Fourier transform of the exchange interaction J_q was calculated and is shown in Figure 9.2 along high-symmetry lines in the Brillouin zone. This allows for determination of the underlying magnetic structure, since J_q is proportional to the magnetic susceptibility; the maximum of J_q corresponds to the maximum of the magnetic susceptibility.

First, the exchange constants for Mn_3SnN in the cubic structure (SGR $Pm\bar{3}m$) without Mn displacements were calculated. The susceptibility has a maximum at the X high symmetry point of the Brillouin zone. This corresponds to the non-collinear Γ^{5g} magnetic structure. Zero net magnetization is obtained using the frozen magnon approximation. It should be noted that these ground-state calculations were not able to reproduce the experimentally observed magnetic structure, which exhibits temperature-dependent spin rotation. This may be explained by the low energy difference between the two configurations, which is mostly dominated by spin-orbit coupling that can be considered to be orders of magnitude smaller than the exchange interaction [134].

Next, Mn displacements are considered within the centrosymmetric ADP model with $P4/mmm$ SGR symmetry (Chapter 8.3) and the effect of 2e site and 1c site splitting investigated separately. In the case of 2e site splitting the magnetic ordering vector is the same as for the structure without Mn displacements, although the induced disorder affects the magnitude of the exchange interaction in the system. In the case of splitting of the 1c site, the exchange interaction is very different from the two previous cases. The maximum of the Fourier transform J_q is located between the Γ and R points. In real space, the structure is characterized by a canting of the Mn spin at the 1c site by 3.5° into the [001] or [00-1] direction, depending of the direction of the displacement along the c-axis. The resulting moment from the uncompensated spin texture is $0.06\,\mu_\text{B}/\text{f.u.}$

Comparison with the magnetic characterization of the MSN thin films shows that the calculated canted moment is likely to be overestimated, as the measured saturation magnetization in 20 nm as well as 200 nm thin films is below this value [see Table 6.3 (p. 56)]. Nevertheless, the calculations support the hypothesis that the Mn displacements induce canted moments in the NCAF structure. Here, displacements at the two sites are considered independently in order to distinguish their effects on the magnetic structure. In a real sample, there are many possible local arrangements of Mn atoms, resulting in locally varying magnitude and direction of the canted moment. These moments are, therefore, highly correlated with the local Mn atoms and their spin arrangement.

In the case of the non-centrosymmetric ADP model with *P*4*mm* SGR symmetry the $\mathrm{Mn_I}$ atom is shifted towards the substrate. On the other hand, in first approximation, the effect of the splitting of the $\mathrm{Mn_{II}}$ atom can be expected to cancel out on average and only the shift of the $\mathrm{Mn_I}$ atom has to be considered. The above calculations show that displacement of the $\mathrm{Mn_I}$ atom strongly affects the magnetic exchange in the system. Therefore, the system behaves similar to the case of tetragonal contraction shown in Figure 9.1(b) and a net magnetization with $M_z > 0$ emerges. Application of a magnetic field in negative z-direction reorients the weak moment and, thereby, reverses the Mn spins. As a non-zero net moment is required for domain structure control, only the *P*4*mm* SGR is also consistent with the AHE measurements, as will be discussed in the next section.

9.2 Manganese Displacements and the Anomalous Hall Effect

9.2.1 Crystal Structure, Magnetism and Magneto-Transport

In many materials, the crystal structure determines the magnetic order [64]. In turn, magnetism affects the material's magneto-transport properties. Because of the strong magneto-structural coupling in cubic NCAFs, the interplay of crystal structure, magnetism and magneto-transport is very complex. This is illustrated in Figure 9.3 and discussed in the following.

On the level of the crystal, there are two main effects to consider: frustration and atomic displacements. Magnetic frustration of the large spin moments residing on the Mn atoms forming a Kagome lattice is at the heart of the formation of NCAF order in these materials. The formation of the trigonal spin arrangements is an energy compromise. Therefore, the magnetic texture is susceptible to small changes on the level of the crystal structure. In some cubic NCAFs, such as $\mathrm{Mn_3NiN}$ and $\mathrm{Mn_3SnN}$, this manifests as coherent spin rotation within the Kagome plane as a function of temperature, for instance.

Crystal structure and magnetism play an important role in determining the material's electronic band structure. Linear transport theory formulates how (magneto-)transport effects can be calculated from the band structure. In the case of NCAFs, various interesting transport effects result from a non-zero Berry curvature of the bands, in this work exemplified by the intrinsic AHE. Here, the AHE is intrinsic to the material and directly results from the electronic band properties, rather than from extrinsic scattering mechanisms [15]. The symmetry of the Berry curvature in k-space is related to the crystal and, most importantly, to the magnetic symmetry, as discussed in Chapter 7.1 (p. 62). In cubic NCAFs, this manifests as a dependence of the AHC on the in-plane spin angle θ_s. Conversely, in this work, this dependence is utilized to conjecture the presence of

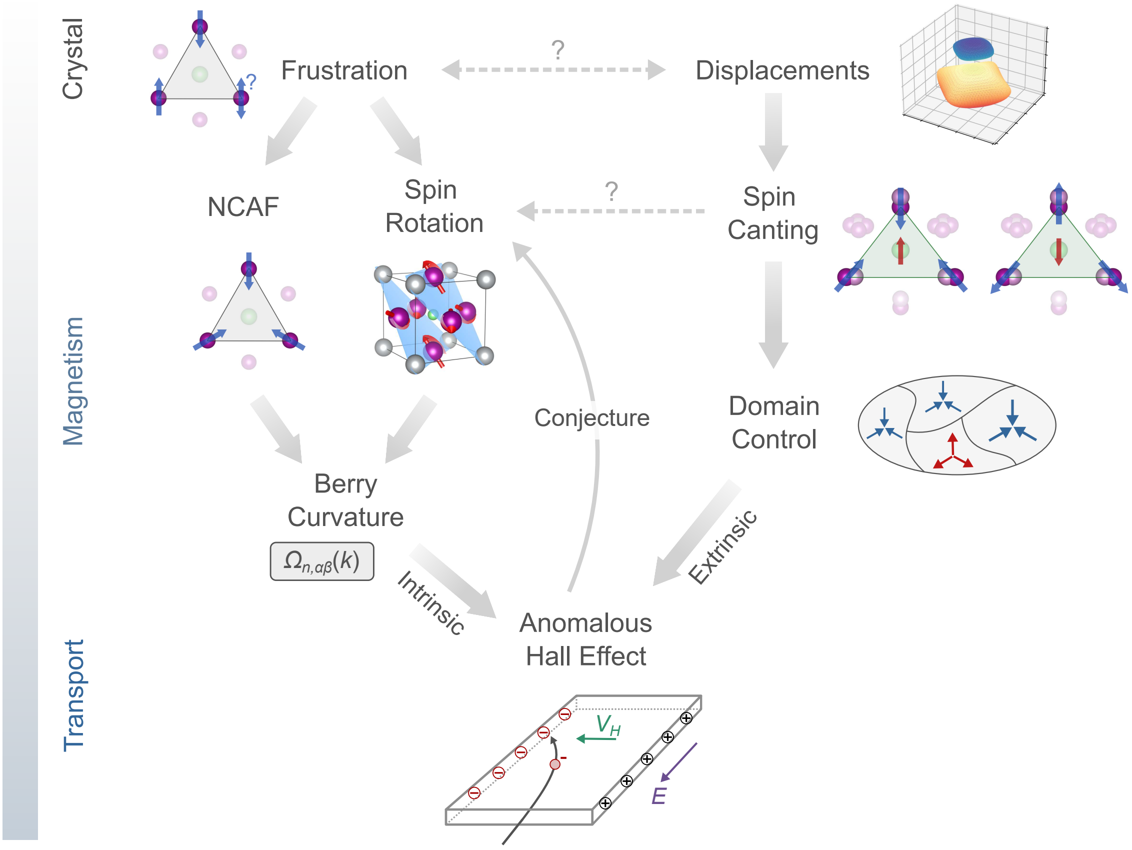
Crystal
Magnetism
Transport
Frustration
?
Displacements
NCAF
Spin Rotation
?
Spin Canting
Conjecture
Domain Control
Berry Curvature
$\Omega_{n,\alpha\beta}(k)$
Intrinsic
Extrinsic
Anomalous Hall Effect
V_H
E

Figure 9.3: Schematic of the relationships and dependencies of crystal structure, magnetism and magneto-transport effects in cubic NCAFs.

temperature-dependent spin rotation in MSN thin films, which, otherwise, is very difficult to observe experimentally.

While the discussion so far describes NCAFs in general, the path on the right side in Figure 9.3 describes the effect of displacements of the Mn atoms. As shown through *ab-initio* calculations, the strong symmetry lowering induced by the atomic displacements leads to spin canting. This is essential to observe a net AHE in MSN, as it allows to set a preponderance of one type of NCAFs domains over others by applying a magnetic field or spin torque. This is exemplified in the figure for a possible local atomic arrangement that generates spin canting. Application of a magnetic field allows to rotate the net moment by 180°. This process corresponds to a rotation of each of the three spins contributing to the net moment by 180°. This 180° spin rotation is equivalent to a time reversal operation. Since the Berry curvature and, by extension, the AHC, are odd under time reversal, this process entails a sign change of the anomalous Hall voltage. The effect of Mn displacements is ultimately extrinsic, as it enables the control of magnetic domains on the level of the real sample. Note that this does not elude to an extrinsic AHE, which is due to scattering from impurities in the presence of strong SOC [15]. The AHE discussed here is, indeed, intrinsic in nature.

There is a correlation of the net magnetization with the AHE. Clearly, the absence of a net magnetization on an atomic level in the case of the bulk crystal structure with cubic symmetry correlated with a vanishing AHE. However, it is not sufficient to break the cubic symmetry. In the case of the tetragonal, centrosymmetric structure with $P4/mmm$ symmetry, the displacements are point symmetric around the high symmetry Wyckoff sites. For each unit cell with a $\mathrm{Mn_I}$ atom displaced to negative z-values, there exists a unit cell, in which the atom is displaced to positive z-values. Averaged over many unit cells, the resulting net moments exactly cancel and, again, no net effect is observed. $P4/mmm$ symmetry is, therefore, inconsistent with the observation of a net AHC. This finding justifies the structural symmetry lowering to the structure with $P4mm$ symmetry in the structural refinement. The key difference is the breaking of the mirror symmetry perpendicular to the [001] direction, allowing for unidirectional, non-centrosymmetric displacement of the $\mathrm{Mn_I}$ atoms with a tendency for the Mn atoms to be displaced toward the substrate. Only then it is possible that the canting caused by the Mn displacements does not average out globally.

In summary, the key role of Mn displacements is to allow the control the NCAF domain structure and, thereby, enable the observation of a net AHC. The novelty of this finding is that, previously, it was assumed that tetragonal distortions need to be present in thin film samples for a non-zero net AHC to be measured. The results presented here prove that the AHE may be, instead, enabled by more subtle structural symmetry lowering. On the one hand, the measurement of Mn displacements requires more elaborate structural analysis, as shown in Chapter 8. On the other hand, it could also be shown that it is possible to perform these experiments in a laboratory setup and access to a synchrotron facility is not necessary.

9.2.2 Comparison of Mn_3SnN and Mn_3Sn

Atomic Mn displacements or tetragonal distortions in thin films of cubic NCAFs serve the same role as the intrinsic spin canting in their hexagonal counterparts. There are, however, notable differences between the two groups of materials as regards the magnetic anisotropy and the mechanisms for domain structure control, as shown in Table 9.1 and discussed in the following.

Mn_3Sn has pronounced easy-plane anisotropy within the Kagome plane. Six stable directions within the Kagome plane are induced by single ion anisotropy, but the energy barrier between them is very low and of the order of magnitude of 0.1 µeV [133]. Mn_3SnN, on the other hand, has strong three-fold symmetric uniaxial anisotropy within the Kagome plane. The energy barrier to reverse the spins along these axes has been calculated for various antiperovskites Mn_3ZN (Z=Ni, Zn, Ga, Ag) and is of the order of magnitude of a few 0.1 meV, a factor of 1000 larger than in the hexagonal case. Therefore, the switching process in Mn_3Sn and Mn_3SnN is very different. In Mn_3Sn the spins can be easily rotated within the Kagome plane by the application of a magnetic field, while in Mn_3SnN a spin reversal of spins pointing along strong anisotropy axes is required. The spin rotation with field in Mn_3Sn has to be distinguished from the temperature-induced spin rotation in Mn_3SnN. The latter results from a temperature dependence of the direc-

Table 9.1: Comparison of the AHE observed in Mn_3SnN and Mn_3Sn: anisotropy, mechanism of domain control and experimental AHC loop shape, theoretically predicted AHC and values measured in thin films and bulk. If not indicated otherwise, values at 300 K are given.

		Mn_3SnN	Mn_3Sn
Anisotropy	Origin	Magneto-crystalline	Single ion
	Direction	Three-fold uniaxial (two stable orientations)	Easy Kagome plane (six stable orientations)
	Energy	≈ 0.1 meV (Mn_3ZN) [110]	≈ 0.1 µeV [133]
Domains	Control	Displacements, distortions	Intrinsic spin canting
	Hysteresis	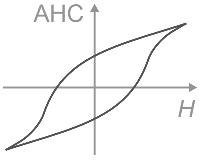	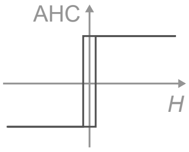
AHC (Ω^{-1}cm^{-1})	Theory	$\sigma_{001} = 133$ [61] $\sigma_{001} = -74$ [168]	$\sigma_{yz} = 248$ [17] $\sigma_{zx} = 129$ [17]
	Bulk	—	$\sigma_{01\bar{1}0} \approx -20$ [29]
	Thin films	$\sigma_{001}^{175K} \approx 0.8$ $\sigma_{001}^{100K} \approx 2.8$ [34]	$\sigma_{20\bar{2}1} = -19$ [169] $\sigma_{40\bar{4}3} = -21$ [130]

tion of the anisotropy axes (parametrized by the anisotropy constants) with temperature, which manifests in a rotation of the spins with temperature [104].

The second key difference is in the mechanisms enabling domain structure control in the two compounds. In Mn_3Sn, on the one hand, single ion anisotropy induces intrinsic spin canting with a defined direction with respect to the crystal axes. In Mn_3SnN, on the other hand, spin canting is induced by Mn displacements or tetragonal distortions. The magnitude and direction of the canted moments depend on their local environment and are, therefore, highly correlated with the local structural disorder.

These two main differences in anisotropy and domain structure control may explain the differences in the shapes of the magnetic and AHC hysteresis loops, as sketched in Table 9.1. While Mn_3Sn bulk and thin film samples show clear, ferromagnet-like hysteresis, Mn_3SnN displays large coercive fields of several Tesla. Furthermore, it exhibits non-saturating AHC hysteresis, reminiscent of minor loops in ferromagnets. This effect is found in AHC loops as well as magnetization loops measured in thick samples, in which the magnetization is not dominated by defects (see Chapter 6.3.1, p. 55), and it persists to high fields of up to 9 T. Gomonaj and L'vov show that the anisotropy constants in antiperovskites are dependent not only on temperature, but also on magnetic field [104]. The application of a field along the [111] direction is expected to result in a spin rotation towards the Γ^{4g} configuration. In the case of (001)-oriented MSN films, the measurement configuration is such that there is a component of the magnetic field along the [111] direction. Therefore, it is possible that field-dependent spin rotation has to be considered to explain the shape of the magnetic and AHE hysteresis in MSN.

Lastly, the magnitude of the AHC of Mn_3SnN and Mn_3Sn are discussed. In Mn_3Sn bulk samples and thin films, the AHC is in the order of a few tens of $\Omega^{-1}cm^{-1}$, which is about 10 % of the theoretically predicted value, as shown in Table 9.1. For Mn_3SnN, no bulk crystal measurements have been reported. Nevertheless, it becomes evident that the AHC of the films presented here as well as reported elsewhere [34] is only a few percent of the calculated values (in Table 9.1, the remanent values measured at the temperature with maximum AHC are reported). Also, the calculated values reported in the literature strongly differ in magnitude and sign. This may be attributed to the subtle effect of temperature-dependent spin rotation, which the thin films sample are subject to, but which are not captured correctly in *ab-initio* calculations. Therefore, comparison of the experimental and the calculated values is difficult. Nevertheless, it is also observed that the AHC is generally lower in Mn_3SnN than in Mn_3Sn, which may also be a result of the non-saturating nature of the AHC hysteresis.

9.3 Open Questions and Outlook

Returning to Figure 9.3, there are two relations that still pose open questions. One concerns the effect that Mn displacements have on the temperature-dependent spin rotation. A linear dependence of the in-plane spin angle θ_s on temperature is found in the thin films samples, similar to bulk samples. This suggests that, in first approximation, the Mn displacements do not interact with the spin rotation. This is supported by the fact that the magnitude of the displacements is mostly temperature-independent, as can be seen from Figure 8.5(b). Nevertheless, as discussed above, because of the strong magneto-structural coupling, the magneto-crystalline anisotropy is likely highly susceptible to small changes in the crystal structure. Therefore, it is plausible that the displacements do affect the spin rotation via the magnetic anisotropy through structural modifications that are below the limit of detection of the measurement.

Figure 9.4 compares the temperature phase diagram of Mn_3SnN in bulk material, obtained by powder neutron diffraction [92], and in thin film form up to 400 K, inferred here from combined structural, magnetic and magneto-transport characterization. The most apparent difference is the absence of phase transitions in thin films. Over the entire temperature range from 5 K to 400 K, the crystal structure with $P4mm$ SGR symmetry characterized by Mn displacements and the canted NCAF structure is stabilized. This is in contrast to bulk MSN, which shows a much richer phase diagram and also exhibits collinear AF and complex ferroic structures, accompanied by pronounced tetragonal distortions.

Given the correlation of Mn displacements with the NCAF structure, it is reasonable to assume that the displacements stabilize the NCAF structure by suppressing the structural distortions encountered in bulk material. It is also possible that this is not a unique feature

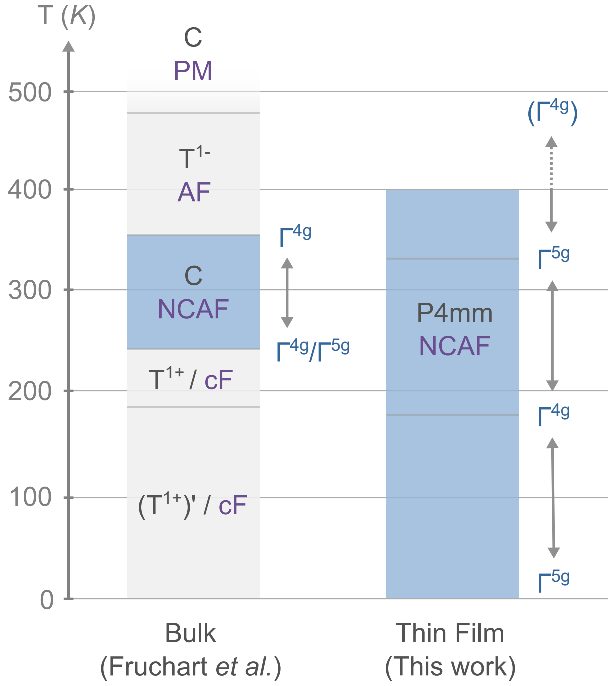

Figure 9.4: Phase diagram of Mn3SnN in bulk material (Ref. [92]) and thin films (this work). Crystallographic phases in gray (C: cubic, T_1^-: tetragonally contracted, T_1^+: tetragonally elongated) and magnetic phases in magenta (cF: complex ferroic).

of the Mn displacements, but may similarly be induced by tetragonal distortions in MSN thin films [34]. Another possibility is that the bulk phase diagram is incorrect. It should be noted that there is only one report of powder neutron diffraction experiments in the literature [92]. Comparison with Mn_3NiN, for which there are several conflicting reports [83, 99, 101], suggests that the phase diagrams of antiperovskites are highly sensitive to sample parameters such as their composition.

There are also clear differences in the details of the temperature-dependent spin rotation between bulk material and thin films. In bulk MSN, spin rotation occurs from $\theta_s = 90^\circ$ (Γ^{4g} configuration) to $\theta_s = 45^\circ$ (combination of Γ^{4g} and Γ^{5g} configuration). This may be a direct result of the greatly enhanced phase stability of the NCAF phase in thin films samples. It is conceivable that the collinear AF phase found in the bulk is suppressed in thin films and the material is NCAF up to the Néel temperature. Although transport measurements were not possible above 400 K due to experimental limitations, linear extrapolation of the in-plane spin angle θ_s to temperature above 400 K yields a Néel temperature of ≈ 490 K, which is slightly above the bulk Néel temperature of 475 K. However, the spin rotation appears to be more complex as compared to bulk MSN. One might expect that the structure rotates from the Γ^{4g} configuration at T_N to the Γ^{5g} configuration at low temperatures. Instead, it is found that the Γ^{5g} structure is reached at ≈ 333 K, as inferred from the vanishing AHC at this temperature. Below this point, the structure rotates further and reaches again the Γ^{4g} configuration at the temperature of maximum AHC of 175 K, below which it rotates again to Γ^{5g}.

There are two hypotheses to explain this unusual temperature-dependent spin-rotation in MSN thin films. The first challenges the underlying assumption that the temperature dependence of the AHC is dominated by the effect of bulk-like spin rotation [see Chapter 7.1.2 (p. 65)]. It cannot be excluded that other so far unexplored effects contribute to the AHE. Another explanation is based on the presence of Mn displacements in MSN thin films. The local symmetry and magnitude of the Mn displacements may have more complex temperature dependences than can be resolved in the structural refinement. It is also noted that the temperature dependence of the AHC is different in MSN thin film samples reported in the literature [34]. Again, this may be attributed to a high susceptibility of the spin rotation to structural parameters.

In summary, the findings presented here reveal very complex and interesting interdependences between structural symmetry lowering in the form of Mn displacements, spin canting, non-collinear antiferromagnetism and intrinsic transport effects in the cubic NCAF Mn_3SnN. An important aspect is that the phase diagram of MSN is very different in bulk and thin film material. Figure 4.3 (p. 33) shows the crystallographic and magnetic phases of various Mn-based antiperovskite nitrides. Assuming that MSN is not unique in its property to have different phase stability in bulk and thin film form, Table 9.2 lists a selection of material candidates whose magnetic properties are unknown or that are known to display NCAF phases in temperature ranges previously considered uninteresting (either very high or very low). The observation of enhanced stability of the NCAF phase in MSN thin films, therefore, motivates the investigation of other previously unexplored antiperovskite nitrides.

Table 9.2: List of antiperovskite nitrides compounds that may be interesting for thin film investigation.

Z	Comment	References
Zn	Γ^{5g}-type NCAF below RT	[82, 84]
Ge	Γ^{5g}-type NCAF at very high T	[72]
Rh	Magnetism for $x = 1$ unclear (Mn_3SbN-like?)	[72, 103]
Pd	Cubic structure, magnetism (AFM) unclear	[72, 102]
Ag	Spin-rotational NCAF at very low T, details unclear	[90, 105]
Cd	Structure and magnetism unknown	[72]
In	Weak ferromagnetic, similar to Mn_3AgN	[72, 98, 100]

So far, the AHE in Mn_3SnN was investigated and shown to be enabled by atomic Mn displacements. This new concept is developed further in the next part. First, it is investigated how various magneto-transport effects in NCAFs are affected by the presence of different kinds of NCAF domains. By comparison with the existing literature and in conjunction with additional structural measurements it is further argued that Mn displacements are not limited to Mn_3SnN and that they may enable the observation of transport effects beyond the AHE in antiperovskites.

Part IV

Manganese Displacements and Transport in Non-collinear Antiferromagnets

Chapter 10

Transport Effects Beyond the Anomalous Hall Effect

10.1 Lead-in

The semi-classical transport formalism was introduced in Chapter 3.1 (p. 25) for the case of the anomalous Hall effect (AHE). In Part III AHE measurements of the cubic non-collinear antiferromagnet (NCAF) Mn_3SnN (MSN) were presented. It was demonstrated that the observation of the AHE in (001)-oriented MSN thin films is not, as commonly assumed, enabled by tetragonal distortion but, instead, by displacements of the Mn atoms away from high symmetry sites. In contrast, (111)-oriented MSN displays no AHE, which results from the presence of a multi-domain state in the sample.

Domain structure control in NCAFs is an important factor that has to be considered, if these materials are to be used in practical spintronic devices. In ferromagnets, the AHE and other transport effects correlated with magnetization can be easily controlled by magnetic field or spin torque. This is not generally the case in NCAFs. The success of hexagonal NCAFs such as Mn_3Sn is likely in great part due to the vanishingly small net magnetization that is intrinsically coupled to the magnetic structure and, thereby, allows for domain structure control by magnetic field [29]. It follows that the mechanisms for domain structure control in cubic systems without such intrinsic mechanism needs to be understood fully, which this work is contributing to.

So far, it has been shown how the presence of multi-domain states in the cubic NCAF MSN leads to a vanishing AHE. This knowledge can be transferred to other charge and spin transport effects. In this part the effect of NCAF domains on magneto-transport effects beyond the AHE is discussed. It is shown that several interesting transport effects cancel in the presence of multi-domain states, similar to the AHE.[1] In Chapter 10.3 this will be discussed and compared with the current literature and it will be shown that there are several works, in which Mn displacements could play the role of enabling the observation of the investigated transport effects. This is supported by experimental evidence of Mn displacements in thin films of the antiperovskite nitrides Mn_3GaN and Mn_3SnN.

---

[1] Fruitful discussion and help with the symmetry analysis by Robin Neumann is greatly appreciated.

10.2 Magnetic Domains in Charge and Spin Transport

10.2.1 Anomalous Nernst Effect

The anomalous Nernst effect (ANE) is the thermoelectric equivalent of the AHE. NCAFs have gained recent attention also in the field of thermoelectric current and spin generation as well as energy harvesting, because they can generate large thermoelectric signals, again with the advantage of having vanishingly small magnetization [170–172].

The ANE describes the generation of a transversal charge current not by an electric field (a mechanical force) but by a thermal gradients $\boldsymbol{\nabla} T$ (a statistical force). The anomalous Nernst conductivity (ANC) $\alpha_{\alpha\beta}$ is related to the AHC as [173, 174]:

$$\alpha_{\alpha\beta} = -\frac{1}{e}\int d\varepsilon \frac{\partial f}{\partial \mu}\sigma_{\alpha\beta}(\varepsilon)\frac{\varepsilon-\mu}{T} \tag{10.1}$$

Herein, e is the electron charge, μ the chemical potential and the integral is over energy ε. f is the Fermi distribution function

$$f(\varepsilon) = \frac{1}{\exp\left(\frac{\varepsilon-\mu}{k_{\mathrm{B}}T}\right)+1} \tag{10.2}$$

The relation between AHC and Berry curvature $\boldsymbol{\Omega}_n$ is given as (Equation 3.4):

$$\sigma_{\alpha\beta} = -\frac{e^2}{\hbar}\sum_n \int_{BZ} \frac{d^3\boldsymbol{k}}{(2\pi)^3} f_n(\boldsymbol{k})\Omega_{n,\alpha\beta}(\boldsymbol{k})$$

In the limit of low temperatures, Equation 10.1 reduces to the standard Mott formula [56]

$$\alpha_{\alpha\beta} = -\frac{\pi^2 k_{\mathrm{B}}^2 T}{3e}\frac{d\sigma_{\alpha\beta}}{d\varepsilon}\bigg|_{\varepsilon=\mu} \tag{10.3}$$

Equation 10.3 shows that the ANC is strongly temperature-dependent and highly sensitive to the slope of the AHC near the Fermi level. A large AHC in a given material does not necessarily mean a large ANC and *vice versa* (the correlation of AHC and ANC in antiperovskite nitrides was studied by *ab-initio* calculations in Ref. [175]).

However, the ANC does inherit the symmetry of the AHC. Therefore, from a symmetry point of view, all statements made so far about the AHE are also true for the ANE. This concerns the shape of the ANC tensors, which are analogous to the AHC tensors shown in Table 3.1 (p. 27), as well as the role of NCAF domains on the net transport effects. Beyond charge transport effects, magneto-optical effects are also allowed by symmetry in NCAFs [110], but the discussion of their spin order dependence lies outside the scope of this work.

10.2.2 Spin Polarized Current and the Spin Hall Effect

The semi-classical theory for charge transport can be generalized to account for effects related to spin transport. In general, the linear response of an observable $\hat{A}$ to an electric field E is [18]:

$$\delta\hat{A} = \chi^{I}E + \chi^{II}E \tag{10.4}$$

with

$$\chi^{I} = -\frac{e\hbar}{\pi}\sum_{\boldsymbol{k},n,m}\frac{\Gamma^2\,\mathrm{Re}\left[\langle n\boldsymbol{k}|\hat{A}|m\boldsymbol{k}\rangle\,\langle m\boldsymbol{k}|\hat{\boldsymbol{v}}\cdot\hat{\boldsymbol{E}}|n\boldsymbol{k}\rangle\right]}{[(E_F-\varepsilon_{n\boldsymbol{k}})^2+\Gamma^2]\,[(E_F-\varepsilon_{m\boldsymbol{k}})^2+\Gamma^2]} \tag{10.5}$$

$$\chi^{II} = -2\hbar e\sum_{\boldsymbol{k},n\neq m}\frac{\mathrm{Im}\left[\langle n\boldsymbol{k}|\hat{A}|m\boldsymbol{k}\rangle\,\langle m\boldsymbol{k}|\hat{\boldsymbol{v}}\cdot\hat{\boldsymbol{E}}|n\boldsymbol{k}\rangle\right]}{(\varepsilon_{n\boldsymbol{k}}-\varepsilon_{m\boldsymbol{k}})^2} \tag{10.6}$$

In Equation 10.6 n are occupied and m unoccupied bands. Γ is a constant broadening parameter taking into account scattering.

Thereby, the linear response $\delta\hat{A}$ is decomposed into two terms that behave differently under time reversal. $\hat{T}$ is an antiunitary operator transforming a matrix element as

$$\langle n\boldsymbol{k}|\hat{A}|n\boldsymbol{k}\rangle \rightarrow \langle n\boldsymbol{k}|T\hat{A}T|n\boldsymbol{k}\rangle^{*} \tag{10.7}$$

Because of the complex conjugate, χ^{I} is invariant under $\hat{T}$, while χ^{II} will have an additional minus sign. Therefore, χ^{I} is even under time reversal, while χ^{II} is odd.

In the case of charge conductance and the AHE, the observable $\hat{A}$ is equal to the charge current density operator

$$\hat{\boldsymbol{j}} = -\frac{e}{V}\hat{\boldsymbol{v}} \tag{10.8}$$

Then, χ^{I} and χ^{II} are, respectively, even and odd functions under time reversal. Physically, they describe (longitudinal) charge conductivity and (transversal) anomalous Hall conductivity (see Table 10.1).

In order to describe spin conductance effects, $\hat{A}$ is chosen to be the spin current density operator

$$\hat{\boldsymbol{j}}^{s}_{i,j} = \frac{1}{2}\{\hat{\boldsymbol{s}}_i,\hat{\boldsymbol{v}}_j\} \tag{10.9}$$

This term contains the spin operator $\hat{\boldsymbol{s}}_i$, which is odd under time reversal. Thus, in contrast to the case of charge conductivity, χ^{I} and χ^{II} are now, respectively, odd and even under $\hat{T}$. The spin conductivity tensor $\sigma^{s}_{i,j}$ is a 3x3x3 tensor, which can be represented as three 3x3 matrices corresponding to the three spin polarization directions s=x, y, z. The off-diagonal terms of the even parts of the spin conductivity tensors describe the spin Hall effect (SHE). Similarly, the off-diagonal terms of the odd part describe spin currents that resemble the SHE, but are odd under time reversal, an effect known as magnetic spin Hall effect (MSHE). Lastly, the diagonal terms of the odd part describe spin polarization along the charge current direction. In analogy to ferromagnets, this corresponds to longitudinally spin-polarized (LSP) currents.

Table 10.1 summarizes the even and odd contributions for the charge and spin current operator. The various effects and their experimental verification is discussed further in Chapter 10.3.

Table 10.1: Evenness and oddness of the contributions of χ^I and χ^{II} to the linear response of charge current and spin current to an applied electric field.

Operator	$\hat{A}$	χ^I	χ^{II}
Charge current	$\hat{\boldsymbol{j}} = -\frac{e}{V}\hat{\boldsymbol{v}}$	Even Charge conductivity	Odd AHE
Spin current	$\hat{\boldsymbol{j}}^s_{i,j} = \frac{1}{2}\{\hat{\boldsymbol{s}}_i, \hat{\boldsymbol{v}}_j\}$	Odd MSHE, LSP	Even SHE

10.2.3 Symmetry Analysis: The Role of Magnetic Domains

In the following, results from symmetry analysis considering the presence of different types of NCAF domains in real samples are presented.

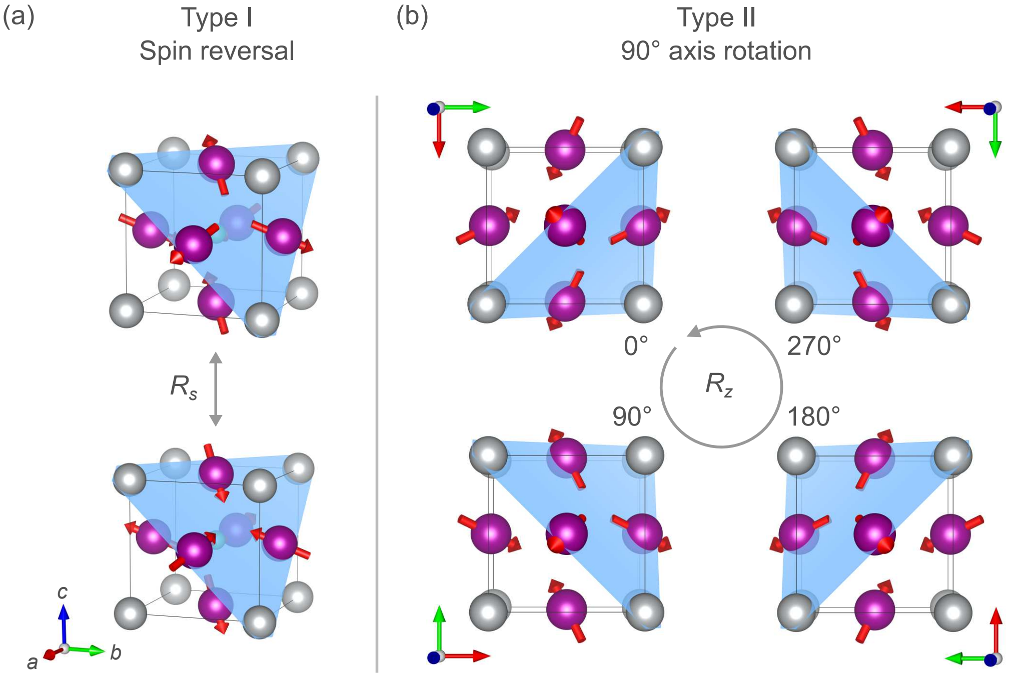

Figure 10.1: Graphical representations of the two types of non-collinear antiferromagnetic domains, shown for the Γ^{4g} configuration. (a) Type I domains related by a spin reversal operation $\hat{R}_s$ and (b) Type II domains related by a rotation $\hat{R}_z$ of the lattice by 90° around the z-axis, viewed along the rotation axis.

The two types of NCAF domains considered here are shown in Figure 10.1. Type I domains are the ones discussed previously in the context of AHE measurements. They are related by a spin reversal operation $\hat{R}_s$ of each spin in the unit cell. As discussed in Chapter 9.2.2 (p. 91), cubic NCAFs differ from their hexagonal counterparts in that they exhibit threefold uniaxial anisotropy axes. This anisotropy gives rise to type I domains, which are, therefore, very similar to ”up” and ”down” domains in ferromagnets with perpendicular magnetic anisotropy.

On the other hand, Figure 10.1(b) shows type II domains, which have no obvious counterpart in ferromagnets. They are generated by four-fold rotation $\hat{R}_z$ by 90° of the magnetic texture around the z-axis. The combination of type I and type II domains yields eight domains in total.

Charge Conductivity Tensor The AHC is proportional to the integral of the Berry curvature, which is odd under time reversal. If two domains are related by spin reversal $\hat{R}_s$, then they are also equivalent under time reversal $\hat{T}$. Therefore, the AHE contributions from the two domains are exactly opposite. This explains the vanishing AHC in (111)-oriented Mn$_3$SnN thin films in Chapter 7.1 (p. 62). In this growth orientation there is no mechanism that allows to set a single-domain state in the sample. Thus, the net AHC vanishes. For brevity, in the following the term single-domain includes domain states characterized by a preponderance of one domain.

To investigate the role of domains related by 4-fold rotation around the z-axis, the corresponding transformation $\hat{R}_z$, given as

$$R_z = \begin{pmatrix} 0 & -1 & 0 \\ 1 & 0 & 0 \\ 0 & 0 & 1 \end{pmatrix} \tag{10.10}$$

is applied to the AHC tensor $\sigma' = R_z \sigma R_z^T$. As shown in Table 10.2, when averaged over the four domains, most of the AHC tensor components vanish. However, the component measured in the experiment (marked in red) remains. Therefore, 4-fold rotation around the z-axis does not cancel the AHC in (001)-oriented thin films with Γ^{4g} magnetic structure. This justifies that type II domains were, so far, not considered in the discussion of the AHE.

Table 10.2: Anomalous Hall conductivity (AHC) tensors in the Γ^{5g} and Γ^{4g} configuration in the case of a single-domain state and averaged over four type II NCAF domains.

IRep	σ	σ^{ave}
Γ^{5g}	$\begin{pmatrix} 0 & 0 & 0 \\ 0 & 0 & 0 \\ 0 & 0 & 0 \end{pmatrix}$	$\begin{pmatrix} 0 & 0 & 0 \\ 0 & 0 & 0 \\ 0 & 0 & 0 \end{pmatrix}$
Γ^{4g}	$\begin{pmatrix} 0 & \sigma_{xy} & -\sigma_{xy} \\ -\sigma_{xy} & 0 & \sigma_{xy} \\ \sigma_{xy} & -\sigma_{xy} & 0 \end{pmatrix}$	$\begin{pmatrix} 0 & \sigma_{xy} & 0 \\ -\sigma_{xy} & 0 & 0 \\ 0 & 0 & 0 \end{pmatrix}$

Spin Conductivity Tensor The shape of the spin conductivity tensor is imposed by the magnetic LGR symmetry [176]. The spin conductivity tensor is then decomposed into two parts that are even and odd under a time reversal symmetry operation. The even and odd spin conductivity tensors for both Γ^{4g} and Γ^{5g} configuration in the case of a single-domain state are presented in Table 10.3. The even components of the spin conductivity tensors are the same in Γ^{4g} and Γ^{5g} configuration, as they are invariant under the additional time reversal operation distinguishing the magnetic LGR $\bar{3}1m$ and $\bar{3}1m'$. In contrast, the odd parts differ in the two cases.

The even components have the same sign in two domains related by spin reversal. The off-diagonal elements in the even spin conductivity tensors correspond to the SHE. The evenness of the intrinsic SHE renders it promising for spin-orbitronic application, as the presence of type I domains does not lead to a cancellation of the effect. However, as shown in the following, in the presence of type II domains, some components of the SHC tensor do cancel out.

The spin conductivity tensors transform as:

$$(\sigma_{ij}^{k})' = \sum_{pqr} R_{ip} R_{jq} R_{kr} \sigma_{pq}^{r} \tag{10.11}$$

Again, $\hat{R}_z$ is applied to generate four domains that are 4-fold symmetric around the z-axis. The averaged spin conductivity tensors are also shown in Table 10.3. The relevance of the symmetry analysis presented here and how it relates to the existing experimental literature is discussed in the next chapter.

Table 10.3: Even and odd parts of the spin conductivity tensor in the Γ^{4g} configuration (magnetic LGR $\bar{3}1m'$) and Γ^{5g} configuration ($\bar{3}1m$) in case of a single domain state and when averaged over four type II domains. Marked in red are those components that are measured in the typical device geometries (Hall bars, ST-FMR devices, magnetic tunnel junctions).

Even parts:
Red: Spin Hall effect terms (measured in ST-FMR)

Γ^{4g}, Γ^{5g}

	σ^x	σ^y	σ^z
Single	$\begin{pmatrix} 0 & -\sigma^x_{xy} & \sigma^x_{xy} \\ \sigma^x_{yx} & -\sigma^x_{yy} & -\sigma^x_{yz} \\ {\color{red}-\sigma^x_{yx}} & \sigma^x_{yz} & \sigma^x_{yy} \end{pmatrix}$	$\begin{pmatrix} \sigma^x_{yy} & -\sigma^x_{yx} & \sigma^x_{yz} \\ \sigma^x_{xy} & 0 & -\sigma^x_{xy} \\ {\color{red}-\sigma^x_{yz}} & \sigma^x_{yx} & -\sigma^x_{yy} \end{pmatrix}$	$\begin{pmatrix} -\sigma^x_{yy} & -\sigma^x_{yz} & \sigma^x_{yx} \\ \sigma^x_{yz} & \sigma^x_{yy} & -\sigma^x_{yx} \\ {\color{red}-\sigma^x_{xy}} & \sigma^x_{xy} & 0 \end{pmatrix}$
Average	$\begin{pmatrix} 0 & 0 & 0 \\ 0 & 0 & -\sigma^x_{yz} \\ {\color{red}0} & \sigma^x_{yz} & 0 \end{pmatrix}$	$\begin{pmatrix} 0 & 0 & \sigma^x_{yz} \\ 0 & 0 & 0 \\ {\color{red}-\sigma^x_{yz}} & 0 & 0 \end{pmatrix}$	$\begin{pmatrix} 0 & -\sigma^x_{yz} & 0 \\ \sigma^x_{yz} & 0 & 0 \\ {\color{red}0} & 0 & 0 \end{pmatrix}$

Odd parts:
Red: Longitudinally spin-polarized current terms (measured in z-direction)

Γ^{4g}

	σ^x	σ^y	σ^z
Single	$\begin{pmatrix} \sigma^x_{xx} & \sigma^x_{xy} & \sigma^x_{xy} \\ \sigma^x_{yx} & \sigma^x_{yy} & \sigma^x_{yz} \\ \sigma^x_{yx} & \sigma^x_{yz} & {\color{red}\sigma^x_{yy}} \end{pmatrix}$	$\begin{pmatrix} \sigma^x_{yy} & \sigma^x_{yx} & \sigma^x_{yz} \\ \sigma^x_{xy} & \sigma^x_{xx} & \sigma^x_{xy} \\ \sigma^x_{yz} & \sigma^x_{yx} & {\color{red}\sigma^x_{yy}} \end{pmatrix}$	$\begin{pmatrix} \sigma^x_{yy} & \sigma^x_{yz} & \sigma^x_{yx} \\ \sigma^x_{yz} & \sigma^x_{yy} & \sigma^x_{yx} \\ \sigma^x_{xy} & \sigma^x_{xy} & {\color{red}\sigma^x_{xx}} \end{pmatrix}$
Average	$\begin{pmatrix} 0 & 0 & \sigma^x_{xy} \\ 0 & 0 & 0 \\ \sigma^x_{yx} & 0 & {\color{red}0} \end{pmatrix}$	$\begin{pmatrix} 0 & 0 & 0 \\ 0 & 0 & \sigma^x_{xy} \\ 0 & \sigma^x_{yx} & {\color{red}0} \end{pmatrix}$	$\begin{pmatrix} \sigma^x_{yy} & 0 & 0 \\ 0 & \sigma^x_{yy} & 0 \\ 0 & 0 & {\color{red}\sigma^x_{xx}} \end{pmatrix}$

Γ^{5g}

Single	$\begin{pmatrix} 0 & -\sigma^x_{xy} & \sigma^x_{xy} \\ \sigma^x_{yx} & -\sigma^x_{yy} & -\sigma^x_{yz} \\ -\sigma^x_{yx} & \sigma^x_{yz} & {\color{red}\sigma^x_{yy}} \end{pmatrix}$	$\begin{pmatrix} \sigma^x_{yy} & -\sigma^x_{yx} & \sigma^x_{yz} \\ \sigma^x_{xy} & 0 & -\sigma^x_{xy} \\ -\sigma^x_{yz} & \sigma^x_{yx} & {\color{red}-\sigma^x_{yy}} \end{pmatrix}$	$\begin{pmatrix} -\sigma^x_{yy} & -\sigma^x_{yz} & \sigma^x_{yx} \\ \sigma^x_{yz} & \sigma^x_{yy} & -\sigma^x_{yx} \\ -\sigma^x_{xy} & \sigma^x_{xy} & {\color{red}0} \end{pmatrix}$
Average	$\begin{pmatrix} 0 & 0 & 0 \\ 0 & 0 & -\sigma^x_{yz} \\ 0 & \sigma^x_{yz} & {\color{red}0} \end{pmatrix}$	$\begin{pmatrix} 0 & 0 & \sigma^x_{yz} \\ 0 & 0 & 0 \\ -\sigma^x_{yz} & 0 & {\color{red}0} \end{pmatrix}$	$\begin{pmatrix} 0 & -\sigma^x_{yz} & 0 \\ \sigma^x_{yz} & 0 & 0 \\ 0 & 0 & {\color{red}0} \end{pmatrix}$

10.3 The Role of Mn Displacements in the Observation of Intrinsic Transport Effects

10.3.1 Overview

This chapter examines how the symmetry arguments presented above relate to the existing experimental literature on magneto-transport effects in cubic NCAFs. The focus lies on the anomalous Hall effect, the spin Hall effect and longitudinally spin polarized charge currents. While the latter is much less investigated than the former two, its potential significant impact in the field of antiferromagnetic spintronics warrants a detailed discussion.

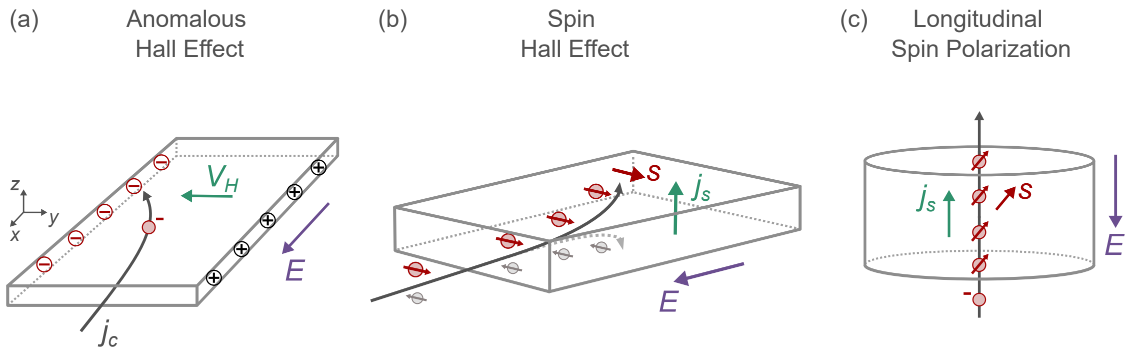

Figure 10.2: Schematic representations of magneto-transport effects in non-collinear antiferromagnets discussed here: (a) anomalous Hall effect (AHE) as well as (b) spin Hall effect (SHE) and (c) longitudinally spin polarized current (LSP) with spin-rotational polarization direction.

Figure 10.2 shows schematic representations of the three effects and Table 10.4 lists works that report on their measurements in cubic NCAFs. The list is limited to the antiperovskite nitrides Mn_3ZN (Z = Ni, Ga, Sn) and the non-nitride compound Mn_3Pt. In the following discussion emphasis is placed on the question whether Mn displacements are a general feature in cubic NCAFs and as to their role in the observation of magneto-transport effects. In this context, the effects are discussed from a symmetry viewpoint and magnitudes of the effects, such as anomalous Hall conductivity or spin Hall angle, are not discussed. It is shown that the structural characterization of different materials presented in the literature suggests that, indeed, Mn displacements are a key component to explaining transport effects in thin films of these materials.

10.3.2 Anomalous Hall Effect and Related Effects

The AHE resulting from symmetry-allowed non-zero Berry curvature has been investigated in many NCAFs [16, 17, 29, 30, 33, 36, 61, 110, 177]. This is likely in part due to the straightforward measurement of the anomalous Hall voltage in thin films or Hall bar devices. Previously, tetragonal distortions were believed to be required in order to observe the AHE in cubic NCAFs, because of the absence of a material-intrinsic effect allowing for control of the NCAF domains. In this work conclusive evidence is presented that the

Table 10.4: Literature summary of works investigating magneto-transport properties of cubic non-collinear antiferromagnets and their structural parameters. d is the film thickness, a and c the lattice parameters, $t = c/a$ the tetragonality and f the lattice mismatch. The samples were grown by sputtering (Sput.), Pulsed Laser Deposition (PLD) or Molecular Beam Epitaxy (MBE). Listed are works investigating the anomalous Hall effect (AHE), anomalous Nernst effect (ANE), spin Hall effect (SHE), magneto-optical Kerr effect (MOKE) and longitudinal spin polarization (LSP). If not stated otherwise, substrate and growth orientations were (001).

Film	Substrate	d (nm)	Growth	Effect	a (Å)	c (Å)	t	f (%)	Comment	Ref.
Mn_3SnN	STO	30	Sput.	AHE				3.9	Composition unclear	[34]
		50		ANE						[177]
		20	Sput.	AHE	4.06	4.06	1.000		Mn displacements	This work
	MgO	16	Sput.	SHE		3.98		—	Grown in (110) and (100)	[178]
Mn_3NiN	STO	50	PLD	AHE	3.887	3.894	1.002	−0.5		[33, 161]
		50		ANE					Scanning ANE microscopy	[35, 161]
		50		MOKE						[161, 179]
Mn_3GaN	LSAT	20	Sput.	SHE	3.916	3.898	0.995	0.6		[27]
	MgO	25	MBE	—	3.89	3.89	1.000	−7.3	Mn displacements	This work
Mn_3Pt	BTO	50	Sput.	AHE			0.999	−3.1		[32]
		10					0.986			[32]
	MgO	50	Sput.	SHE		3.802		−8.1	Bulk value $a = 3.833$ Å	[180]
	$MgAl_2O_4$/MnPt	5	Sput.	LSP		3.805		—	MnPt interlayer	[21]

AHE can also be enabled by displacements of Mn atoms away from high symmetry positions. Therefore, it can also be present in samples with cubic lattice metric.

The AHE in MSN was also investigated in Ref. [34]. However, in that work the nitrogen content of the MSN was varied to change the strain state in the sample, as discussed in Chapter 9 (p. 85). Furthermore, only the out-of-plane lattice parameter c was evaluated and the biaxial in-plane strain calculated, supposedly assuming volume conservation and a unit cell volume of the compound with the correct stoichiometry. Measurement of the out-of-plane lattice parameter is insufficient to prove the presence of tetragonal distortion. The value of c may deviate from the bulk value and the sample may have cubic lattice metric with $a = c$. This is especially true, if the sample composition is unknown. Therefore, the structural characterization presented in that work does not allow any conclusions to be drawn about the presence or absence of tetragonal distortion in the presented samples. The same is true about the report of the ANE and the SHE in samples grown by the same research group [177, 178].

Transport effects in isostructural Mn_3NiN were investigated in several works by Boldrin and Johnson *et al.* [33, 35, 101, 160, 161, 179]. The lattice parameters of 50 nm thin Mn_3NiN films grown by Pulsed Laser Deposition (PLD) were measured by neutron diffraction to be $a = 3.887\,\text{Å}$ and $c = 3.894\,\text{Å}$ [161], which amounts to a tetragonality of $t = c/a = 1.002$. Similar to MSN (tetragonality of $t = 1.000(3)$) this value corresponds to an almost perfectly cubic lattice metric. Given the low lattice mismatch of Mn_3NiN and STO of –0.5 % this low tetragonality is expected. In spite of this observation, non-zero AHE, ANE and magneto-optical Kerr effect (MOKE) were observed in these samples [33, 35, 179]. With reference to Chapter 10.2.1, the observation of ANE and MOKE is expected, given their symmetry equivalence to the AHE. It remains subject of further study whether Mn displacements are also present in Mn_3NiN thin films.

10.3.3 Spin Hall Effect in Mn_3GaN and Mn_3SnN

The off-diagonal terms of the even parts of the spin conductivity tensors describe the spin Hall conductivity (SHC). Historically, the SHE was associated with heavy metals such as Pt, where it is due to spin-orbit coupling. In heavy metals, an electric field applied in x-direction generates a pure spin current in z-direction with spin polarization in y-direction [22, 181]. Spin Hall currents can be measured using various indirect techniques such as spin-torque ferromagnetic resonance (ST-FMR) [182]. Furthermore, the spin-orbit torque (SOT) exerted by the spin accumulation on the adjacent ferromagnet is of practical interest in spin-orbitronic devices [183, 184].

This classical SHE, in which the spin polarization is in the y-direction, is also observed in collinear and non-collinear AFs [185–187]. Furthermore, from the off-diagonal elements of the even spin conductivity tensors in Table 10.3 it can be seen that the magnetic symmetries in some NCAFs allow for non-zero SHC components with spin polarization in directions other than in the y-direction. This is sketched in Figure 10.2(b). These components give rise to ”unconventional” [27] or ”spin-rotational” [25] SOT components

components, which are technologically relevant, as they may allow for field-free switching of magnetic layers with perpendicular magnetic anisotropy [24,27,184].

Table 10.3 also shows that there are off-diagonal terms that are odd under time reversal symmetry. This effect has been referred to as magnetic spin Hall effect (MSHE) and was reported in Mn_3Sn and Mn_3Pt thin films [188, 189]. The oddness of the effect requires a single-type I domain state in the sample. Furthermore, similar to the even SHE, most of the components vanish in the presence of a multi-type II domain state. Nevertheless, MSHE components with spin polarization in x- and y-direction remain in the Γ^{4g} and Γ^{5g} configuration, respectively.

Nan *et al.* have investigated the SHE with time-even and spin-rotational symmetry in Mn_3GaN (MGN) by ST-FMR measurements with varying in-plane field angle [27]. Indeed, they find spin torque components resulting from spin currents with spin polarization direction in x-, y- and z-direction, of which only the y-component remains when heating the sample above the Néel temperature (in the paramagnetic phase, only the y-component is allowed and is due to spin-orbit coupling). Furthermore, the authors find a vanishing AHC, which is consistent with the presence of a Γ^{5g} magnetic texture. These results are consistent with a single-type II NCAF domain state. In a multi-type II domain state, on the other hand, only the y-component is allowed by symmetry.

The authors find that the MGN thin films have almost cubic lattice metric with a tetragonality of $t = 0.995$. They attribute the domain control to this small distortion. The similarity in the apparent structural properties of the MGN films grown by Nan *et al.* and the MSN films grown in this work were noted and it was hypothesized that the domain structure control in MGN is enabled not by tetragonal distortion but by Mn displacement, as in the case in MSN. This motivated the investigation of the SHE by ST-FMR in the MSN thin films grown in this work as well. As presented in Appendix A, a SHE with spin-rotational torque components is also found in (001)-oriented MSN, similar to Refs. [27,178].

10.3.4 Mn Displacements in Mn_3GaN and Domain Structure Control

To test whether Mn displacements are also present in Mn_3GaN, 25 nm thin, (001)-oriented MGN films were grown on MgO(100) by MBE.[2] The lattice parameters of the MGN thin films were measured using the six-circle diffractometer and found to be bulk-like with $a = c = 3.89\,\text{Å}$. This corresponds to a tetragonality of $t = 1.000(4)$. Therefore, within the margin of error of the measurement the sample can be considered to have cubic lattice metric. This in spite of the large lattice mismatch of MGN and MgO of $-7.3\,\%$.

Structural refinement was performed analogous to that of MSN and employing the shifted-sites model introduced in Chapter 8.4 (p. 78). Indeed, it is found that Mn displacements with a magnitude similar to that found in MSN are present in the MGN thin films. Figure 10.3(b) shows the displacement magnitudes at the two Mn sites against the lattice

---

[2] Thin film deposition and growth parameter optimization was performed by Malleswararao Tangi. The grow parameters are reported in Ref. [36].

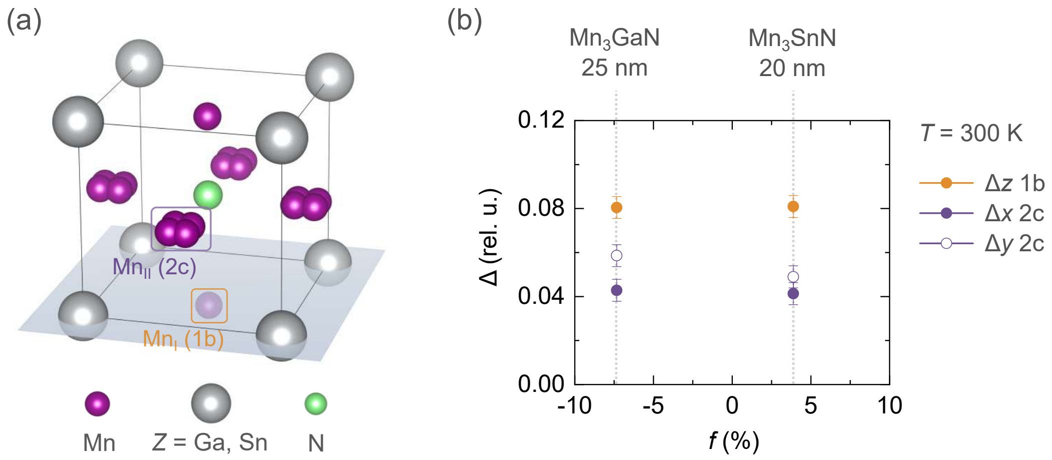

Figure 10.3: Mn displacements in Mn_3GaN and Mn_3SnN: (a) Graphical representation of the refined non-centrosymmetric crystal structure model structures with *P*4*mm* SGR symmetry. (b) Displacement magnitudes against lattice mismatch observed in Mn_3GaN grown on MgO(100) and Mn_3SnN grown on STO(100).

mismatch of substrate and film material. It is found that Mn displacements are formed under tensile (MGN) and compressive (MSN) substrate strain. This also suggests that displacement formation is not due to characteristics of a single depositions techniques, as it is found in samples grown by sputtering and MBE.

In the previous chapter, it was shown how tetragonal distortions allow for domain structure control of type I domains [see Figure 9.1 (p. 86)]. Nan *et al.* argue that type II domains can also be controlled by application of magnetic field. However, the direction of the canted moment depends on the exact spin configuration. Figure 10.4 shows how net moments can be generated by tetragonal distortions and Mn displacements in the Γ^{4g} and Γ^{5g} configuration.

In the Γ^{4g} configuration, the net moment is in {-1-12}-type directions and, therefore, has a component along the z-direction. This allows for control of type I domains by application of magnetic field out-of-plane. Control of type II domains, however, is not possible, as the direction of the in-plane component of the net moment of the four different domains is unaffected by an out-of-plane field [see Figure 10.1(b)]. In the Γ^{5g} configuration the net moment is along {-110}-type directions, and has zero component along the z-direction. Therefore, in this configuration, and within this simplified picture, domain structure control by net moments generated by tetragonal distortion or Mn displacements is not possible with out-of-plane fields for neither of the domain types.

However, type II domains can be controlled by in-plane magnetic fields, as shown in Figure 10.5. This is important in the context of ST-FMR measurements, in which a field is indeed applied in-plane and swept through the resonance condition of the ferromagnetic layer. Furthermore, in the field angle-dependent measurements required to resolve the x-, y- and z-torque components, the field is rotated in-plane around the sample normal. In the ST-FMR measurements by Nan *et al.* the field strength was $\mu_0 H \leq 250\,\mathrm{mT}$. No magnetization loops are reported in that work, but it is possible that the coercive field of

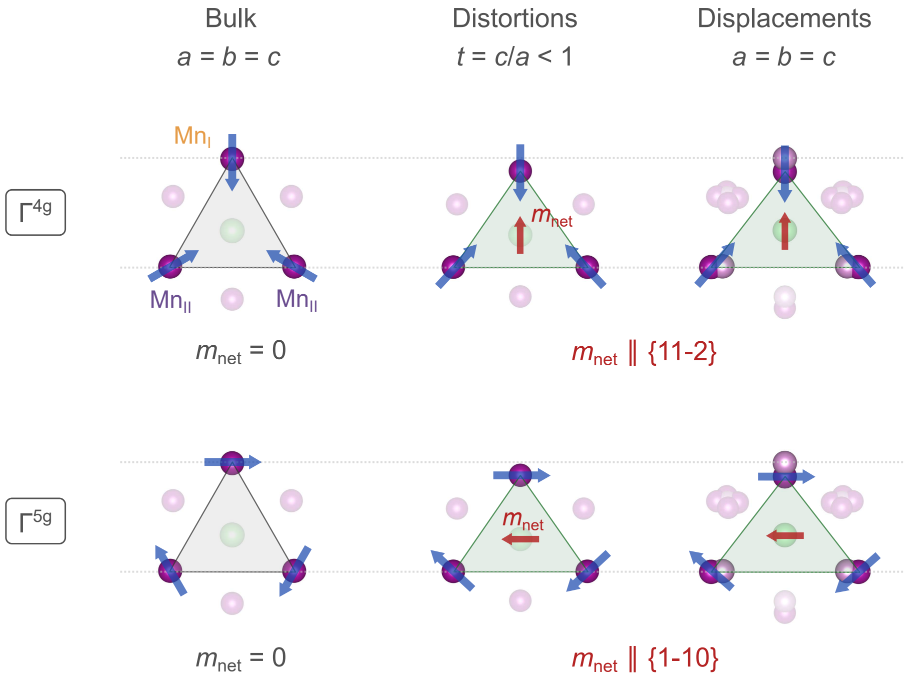

Figure 10.4: Directionality of net moments due to spin canting in the Γ^{4g} and Γ^{5g} configurations induced by tetragonal distortion and Mn displacements.

the weak moment in the films is smaller than 250 mT. For comparison, in Mn_3Pt films with comparable thickness the coercive field was found to be $\mu_0 H_c \approx 130\,\mathrm{mT}$ [32]. Also, the history of the sample is unknown and it cannot be excluded that it was subjected to high in-plane fields prior to the reported ST-FMR measurements and might, thereby, have been brought into a single domain state. Therefore, it is conceivable that a type II single-domain state is generated in the sample prior to or during the ST-FMR measurement.

10.3.5 Longitudinal Spin Polarization

The last effect discussed here is the generation of charge currents with longitudinal spin polarization (LSP). This effect is known from ferromagnets, in which a charge current becomes spin-polarized when passing through the ferromagnet. In this case the spin polarization direction is along the magnetization direction. It cannot be overstated how important this effect was in the development of spintronics, as it is at the heart of spin-transfer torque (STT) and the associated magnetic random access memory (STT-MRAM).

MRAM is based on magnetic tunnel junction (MTJs) comprising two ferromagnetic layers separated by a thin insulating tunneling barrier, typically made of MgO. Such a junction exhibits tunneling magnetoresistance (TMR), in which the resistance of the junction depends on the relative orientation of the magnetization in the two ferromagnetic layers. The properties of the two layers are tailored such that the magnetization of one layer is fixed, while the magnetization of the other can be changed by magnetic field or STT. Thereby, the fixed layer serves as spin polarizer, while the free layer serves as spin detector.

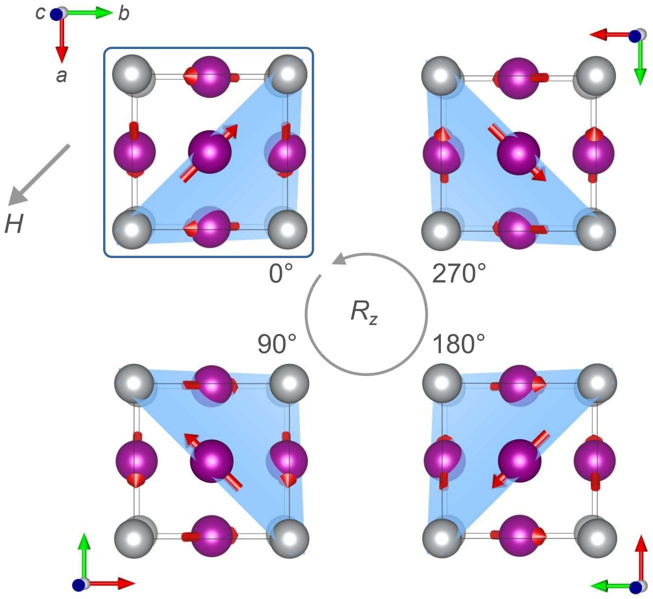

Figure 10.5: Type II domains in the Γ^{5g} configuration viewed along the rotation axis. Application of a field H in [1-10] direction favors the domain at $R_z = 0°$ marked in blue.

LSP is related to the diagonal terms of the odd part of the spin conductivity tensor (see Table 10.3). It was found that these terms can be non-zero in some NCAFs [18, 19]. Given the many advantages of antiferromagnets, it is evident that the prospect of symmetry-allowed spin-polarized charge currents in antiferromagnets is of major technological importance. All-antiferromagnetic tunnel junctions, in which the ferromagnetic layers are replaced by the NCAFs Mn_3Sn and Mn_3Pt, were reported for the first time in 2023 [20, 21]. The reported TMR ratios in Mn_3Sn and Mn_3Pt are of the order of magnitude of, respectively, 1 % and up to 100 %. In the following, the effect is, again, discussed from the viewpoint of symmetry and only the cubic Mn_3Pt is discussed.

Figure 10.2(c) shows a simplified device geometry employed in these measurements, which shows only the fixed layer in the all-antiferromagnetic tunnel junction. A charge current passing through the junction in z-direction is longitudinally spin polarized, i.e. the spin current direction is also in the z-direction. Table 10.3 shows that in a single-domain state all spin polarization components are symmetry-allowed. Furthermore, the effect is odd under time reversal. Therefore, similar to the AHE, it changes sign under a spin reversal operation and cancels in the presence of type I NCAF domains.

In the presence of type II domains, many of the components cancel, similar to the SHE. Most importantly, it is found that in this case only spin currents with spin polarization in z-direction are allowed. Furthermore, this is only true for the Γ^{4g} configuration, while in the Γ^{5g} configuration, all LSP components vanish. Therefore, domain control of both domain types would be required in MTJs comprising materials with Γ^{4g} configuration, such as Mn_3GaN.

In the case of Mn_3Pt, which exhibits a Γ^{4g} NCAF order, only control of type I domains is required to observe a TMR effect in an all-antiferromagnetic tunnel junction. Analogous to the AHE, this requires the presence of tetragonal distortion or Mn displacements in Mn$_3$Pt. The structural characterization of the films grown in that work only reveals an out-of-plane lattice parameter of $c = 3.805\,\text{Å}$. The bulk value is $a = c = 3.883\,\text{Å}$. In a previous work the same group grew Mn$_3$Pt thin films on BTO with a composition very close to the perfect composition (according to energy-dispersive X-ray spectroscopy measurements) [32]. Therein, 50 nm films displayed a tetragonality of $t = 0.99$. This suggests that tetragonal distortion is the mechanism allowing for domain structure control in these Mn$_3$Pt thin films.

It remains subject of further study whether Mn displacements are present in addition to tetragonal distortion in Mn$_3$Pt thin films. If this is not the case, this would suggest that the additional nitrogen atom in antiperovskite nitrides plays is crucial for the formation of Mn displacements.

10.3.6 Summary and Open Questions

Table 10.5 summarizes the transport effects discussed here and their behavior in the presence of multi-type I and multi-type II domain states. Throughout the discussion and with reference to Table 10.4, it becomes evident that there are several works reporting non-zero transport effects that are consistent only with a single-type I domain state (AHE in Mn$_3$SnN and possibly Mn$_3$NiN as well as LSP in Mn$_3$Pt) or single-type II domain state (SHE in Mn$_3$GaN). This is in spite of the samples exhibiting cubic lattice metric. The results of structural refinement of Mn$_3$SnN and Mn$_3$GaN presented in this work strongly suggest that in these cases domain structure control is enabled by Mn displacements that are undetected in conventional structural characterization. This further indicates that Mn displacements are a general feature of antiperovskite nitrides or even other cubic NCAFs. Structural characterization of more materials is required to confirm the generality of this effect.

Table 10.5: Summary of the effect of non-collinear antiferromagnetic domains on several transport effects and experimental works investigating these effects. ”✓” and ”×” indicate whether the effects are present or absent. Materials with Γ^{4g} configuration or spin-rotational phase are marked in red and materials with Γ^{5g} configuration are shown in blue.

Effect	Single domain	Type I	Type II	Experiments
Anomalous Hall effect	✓ ×	× ×	✓ ×	[32, 33, 36, 177] [27]
Spin Hall effect	x, y, z x, y, z	✓	y y	[177, 180] [27]
Magnetic SHE	x, y, z y, z	×	x y	
Longitudinal spin polarization	x, y, z x, y	×	z ×	[21]

In this context, an important active research field is the imaging of NCAF domains. In ferromagnets, this is usually done optically by employing the magneto-optical Kerr effect.

So far, this has only been achieved in Mn_3Sn single crystals, but not in thin films [190]. Another imaging technique is scanning anomalous Nernst microscopy, in which a focused laser beam is scanned over a Hall bar device. The induced heat gradient along the film normal causes an anomalous Nernst current, which is measured in the device as a function of the heating laser position. This indirect technique was employed to image the NCAF domain structure in Mn_3Sn and Mn_3NiN [35, 191].

A thorough understanding of NCAF domain walls themselves is lacking. This is relevant not only in the context of the racetrack memory, which is a novel data storage technology conceptually very different from common approaches [8]. It may also be crucial in the interpretation of transport measurements, as the domain walls themselves might contribute to transport effects such as the AHE. It was theoretically predicted that topological defects occur at the domain walls of the NCAFs Mn_3Sn and Mn_3Ge that may contribute to the AHE in addition to the intrinsic bulk effect. Topological Hall effect-like contributions to the transversal conductivity were indeed found in Mn_3Sn thin films [130], though their observation remains open in cubic NCAFs.

Chapter 11

Conclusions, Implications and Open Questions

At the time of starting this research work, the study of intrinsic transport effects in noncollinear antiferromagnets (NCAFs) was limited to theoretical considerations [16–18] and experimental investigations of a few hexagonal NCAFs, with the research focusing on the hexagonal compounds Mn_3Ge and Mn_3Sn [29, 30]. A comprehensive review of antiferromagnetic spintronics had only been published in 2018 by Baltz *et al.* [2]. Over the following years, more reports of the anomalous Hall effect (AHE) and the spin Hall effect (SHE) in cubic NCAFs were published [27, 32–34].

The initial aim of this work was to study magneto-transport effects in the NCAF Mn_3SnN, which had not yet been reported in thin film form. It was found by standard X-ray diffraction (XRD) that (001)-oriented films exhibit a cubic lattice metric. This was inconsistent with the anomalous Hall effect observed in these films, as it was previously assumed that substrate-induced tetragonal distortions are necessary to create net moments allowing for domain structure control and a net AHE. It was realized that the same could be observed in samples of other NCAFs reported in the literature, which had not been discussed in detail in these works [27, 33, 34]. The research focus then shifted towards resolving the mechanism that enables the observation of the AHE in this material.

By employing more unconventional methods for thin film structural characterization, it was found that the crystal structure, although displaying cubic lattice metric, has, in fact, reduced symmetry. This is due to the presence of displacements of the Mn atoms away from high-symmetry positions, which induce spin canting and, thereby, allow for domain structure control. By structural investigation in conjunction with magnetic characterization and magneto-transport measurements atomic Mn displacements were identified as a novel mechanism allowing for domain structure control in cubic NCAFs. This challenges the long-held assumption that tetragonal distortions are required in these materials in order for non-zero transport signals to be observed.

Nevertheless, open questions concerning the Mn displacements remain. First, the origin of the Mn displacements is not yet resolved. They may be caused by strain induced by the lattice mismatch of substrate and film. As such, they could be a new mechanism for strain relaxation in thin films of cubic NCAFs, in addition to tetragonal distortion and misfit dislocations. Alternatively, they could result from the thin film growth being an out-of-equilibrium process.

In this work, the antiperovskites Mn_3SnN and Mn_3GaN were investigated and Mn displacements found in both compounds. While this provides reasonable evidence that Mn displacements are not limited to a single material or deposition technique, the generality of the effect in antiperovskites or other cubic NCAFs such as Mn_3Pt remains to be established. Nevertheless, it is striking that structural distortions induced by the interplay of crystal and magnetic structure are well-known in compounds containing Mn. An example are Jahn-Teller distortions in transition metal manganites [192]. Against this background, it is noted that many collinear antiferromagnets such as Mn_2Au or MnCuAs [193, 194] as well as material candidates of the newly found class of altermagnets [195] contain Mn. To determine the origin of Mn displacements in these materials, future studies could investigate the dependence of the displacement magnitudes on the lattice mismatch of substrate and film. For instance, this can be achieved by growing different antiperovskites on different substrates or by using interlayers with varying lattice constants in order to yield a more complete picture than could be established in this work [see Figure 10.3(b), p. 110]. From an experimental point of view, this requires a solution to the problem that the XRD reflections from substrate and film are very difficult to distinguish when the two materials have the same space group symmetry and similar lattice constants, i.e. low lattice mismatch. This may be achieved by using non-perovskite substrates with a low mismatch with the film.

The global structural investigation by XRD may be complemented by local techniques. For instance, it would be interesting to study the displacements on an atomic level by advanced transmission electron microscopic imaging. Furthermore, theoretical considerations may help resolve the origin of Mn displacements. For instance, it could be investigated by *ab-initio* calculations, whether the formation of Mn displacements is energetically favorable over tetragonal distortion. Potentially, the frustrated magnetic texture itself could drive the formation of Mn displacement in a Jahn-Teller-like fashion.

A technological goal could be to engineer Mn displacements by strain or growth parameter optimization, for instance. This could also help to strengthen the link of displacements and non-zero transport signatures. If it were possible to switch the displacements on and off, similar to how the strain state of tetragonally distorted films can be switched by using a piezoelectric substrate [32], this could enable new switching schemes. Novel spin-orbitronic devices based on NCAFs instead of heavy metals could be engineered in which the "unconventional" [27] spin-rotational torque components could be switched on and off, which would allow for different writing modes depending on the state of the NCAF spin Hall layer.

The technical viability of NCAFs as materials to substitute conventional materials in spintronic devices remains to be established. The observation of longitudinal spin polarization of charge currents in all-antiferromagnetic tunnel junctions has been demonstrated only very recently in two publications [20, 21]. Because ferromagnetic tunnel junctions are established key components in commercial spintronic memory technologies, there will have to be very convincing arguments as to why NCAFs are better suited for these applications than ferromagnets. For instance, this could be achieved by demonstrating higher writing speeds or read-out signals as well as through an improved scalability.

A similar argument can be made for the application of NCAFs in spin-orbitronic devices, where they could replace critical materials such as Pt as spin Hall materials in spin-orbit torque magnetic random access memory (SOT-MRAM). The spin-rotational spin torques generated in NCAFs are, in principle, a promising route to field-free SOT switching of magnetic layers with perpendicular magnetic anisotropy. However, it remains to be established that the torque efficiencies are high enough to compete with other materials such as van-der-Waals materials or SOT switching schemes in Pt-based SOT devices using novel device architectures [184]. To this end, it is critical to understand the effect of NCAF domains on the SHE and their control in actual devices, to which this work has also contributed.

This work further demonstrates that the generally accepted practice of inferring the crystal symmetry from the lattice parameters alone is generally insufficient to resolve the finer details of the crystal structure of real thin film samples. In the case of cubic NCAFs, this is of major relevance for the interpretation of magneto-transport data. Wrong assumption about the mechanisms allowing for domain structure control may lead to a wrong interpretation of transport data or to valuable experimental data being discarded, because transport signals are measured that are thought to not be allowed based on the supposed crystal structure.

The unique approach taken here is to directly link crystal structure refinement to magneto-transport effects, in this case the AHE. Herein, the performed AHE measurements are standard and straightforward measurements. On the other hand, the structural refinement procedures, especially those including higher-order anharmonic corrections in the structural models, are not yet well-established in the spintronics community. Nevertheless, this work also demonstrates that these experiments are nowadays possible using laboratory X-ray sources and do not require access to synchrotron facilities. As such, this work also aims to stimulate the incorporation of this approach more broadly in the research of novel magnetic materials and spintronics.

Part V

Appendices

Appendix A

ST-FMR Measurements of Mn_3SnN Thin Films

Spin-torque ferromagnetic resonance (ST-FMR) is employed to study the spin torques generated by the spin Hall effect (SHE) in 20 nm thin, (001)- and (111)-oriented Mn_3SnN (MSN) films. The technique was developed to quantify the spin Hall angle of heavy metals (HM) [182, 196]. As can be seen from Figure A.1, a HM layer (here Pt) is in contact with a soft in-plane ferromagnet (FM), here permalloy (Py). Both layers have a thickness of a few nanometers. An external magnetic field and an RF current are applied to the ST-FMR device. The SHE in Pt generates an oscillatory spin accumulation at the HM/FM interface, which excites the FM to precess. The magnetization dynamics of the FM are described by the Landau-Lifshitz-Gilbert-Slonczewski (LLGS) equation:

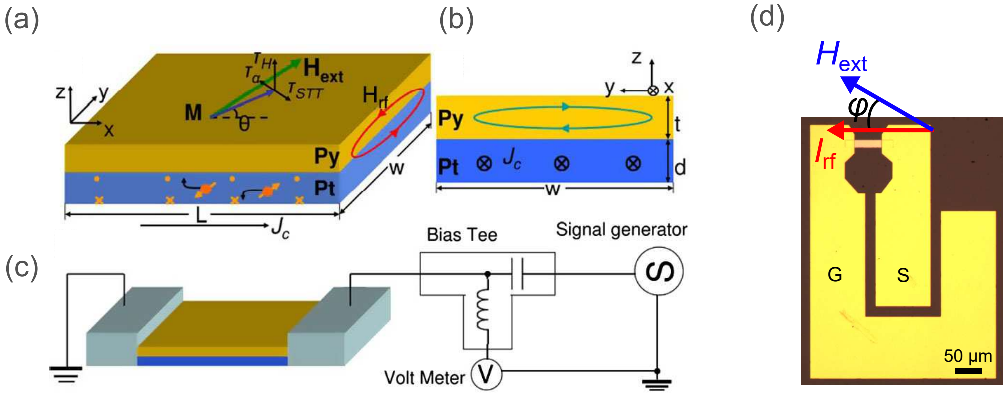

Figure A.1: Schematic showing the principle of spin-transfer ferromagnetic resonance (ST-FMR). (a) A Pt/Py bilayer and the field-like and anti-damping-like spin torques generated by the SHE in Pt. (b) An Oersted field is created by the current passing through the sample. (c) A strip of the Pt/Py bilayer is contacted to an RF signal generator and a DC voltmeter through a bias tee. (d) Optical image of a typical ST-FMR device for field angle-dependent ST-FMR measurements of Mn_3SnN/Cu/Py trilayer devices used here. Figures (a) to (c) taken from Ref. [196].

$$\frac{d\boldsymbol{m}}{dt} = -\gamma \boldsymbol{m} \times \boldsymbol{H}_{\text{eff}} + \alpha \boldsymbol{m} \times \frac{d\boldsymbol{m}}{dt} - |\tau_{\text{FL}}| \boldsymbol{m} \times \boldsymbol{\sigma} - |\tau_{\text{AD}}| \boldsymbol{m} \times (\boldsymbol{m} \times \boldsymbol{\sigma}) \tag{A.1}$$

Herein, $\boldsymbol{m}$ and $\boldsymbol{\sigma}$ are the magnetization and the spin polarization. The two last terms describe the effect of the field-like (FL) and anti-damping-like (AD) torques generated by the spin Hall material.

An optical image of a typical ST-FMR device used here for the study of MSN is shown in Figure A.1(d). 20 nm thin MSN films with (001)- and (111)-growth orientation were grown on SrTiO$_3$ using the deposition parameters shown in Table 6.1. 10 nm thin Py layers were grown as the FM layer. To break any possible exchange bias at the interface of the two magnetic layers, a 2 nm thin Cu spacer was inserted between the two layers and it was confirmed by magnetic measurements that the magnetic layers are decoupled. The full trilayer stack was grown in the MANGO sputtering chamber. The films were patterned into ST-FMR devices consisting of a strip of MSN/Cu/Py trilayer contacted by a coplanar waveguide. Ground-source (GS) RF tips were used to contact the devices. The device resistances were close to 50 Ω to reduce the impedance mismatch of device and RF electronics.

For the ST-FMR measurements RF currents were passed through the devices with frequencies ranging from 4 GHz to 14 GHz. The devices were aligned with the film such that the currents passed in the [100] and [1-10] direction for the (001)- and (111)-oriented sample, respectively. The samples were rotated to set an in-plane field angle φ between the external magnetic field H_{ext} and the current direction, which also explains the U-shaped contact pads visible in Figure A.1(d).

An RF current passing through such a device excites a magnetization precession in the FM, which is measured through the DC mixing voltage V_{mix} that results from the oscillatory anisotropic magnetoresistance (AMR) of the FM:

$$\begin{aligned} V_{\text{mix}}(H_{\text{ext}}) &= V_S F_S(H_{\text{ext}}) + V_A F_A(H_{\text{ext}}) && \text{(A.2)} \\ &= V_S \frac{\Delta^2}{\Delta^2 + (H_{\text{ext}} - H_0)^2} + V_A \frac{\Delta(H_{\text{ext}} - H_0)}{\Delta^2 + (H_{\text{ext}} - H_0)} && \text{(A.3)} \end{aligned}$$

The lineshape of the magnetic field dependence of the mixing voltage can be described as a sum of symmetric and antisymmetric Lorentzian functions F_S and F_A, weighted by the respective voltages V_S and V_A. The resonance spectra measured at an RF frequency of 6 GHz, an RF power level of 21 dBm and a field angle of 45° of trilayer with (001)- and (111)-oriented MSN are shown in Figures A.2(a) and (b).

The spectra are fitted to extract V_S and V_A, the resonance field H_0 and the resonance linewidth Δ, which is described by the Gilbert equation and depends on the damping parameter of the FM α and the RF frequency f:

$$\Delta = \frac{2\pi\alpha}{\mu_0\gamma} \cdot f + \Delta_0 \tag{A.4}$$

γ is the gyromagnetic ratio (a Landé factor of $g_e = 2.07$ is assumed for Py). Δ_0 is the inhomogeneous broadening. α and Δ_0 are extracted from fitting the frequency dependence of Δ, as shown in Figure A.2(c) for the (001)-oriented sample. Furthermore, the effective

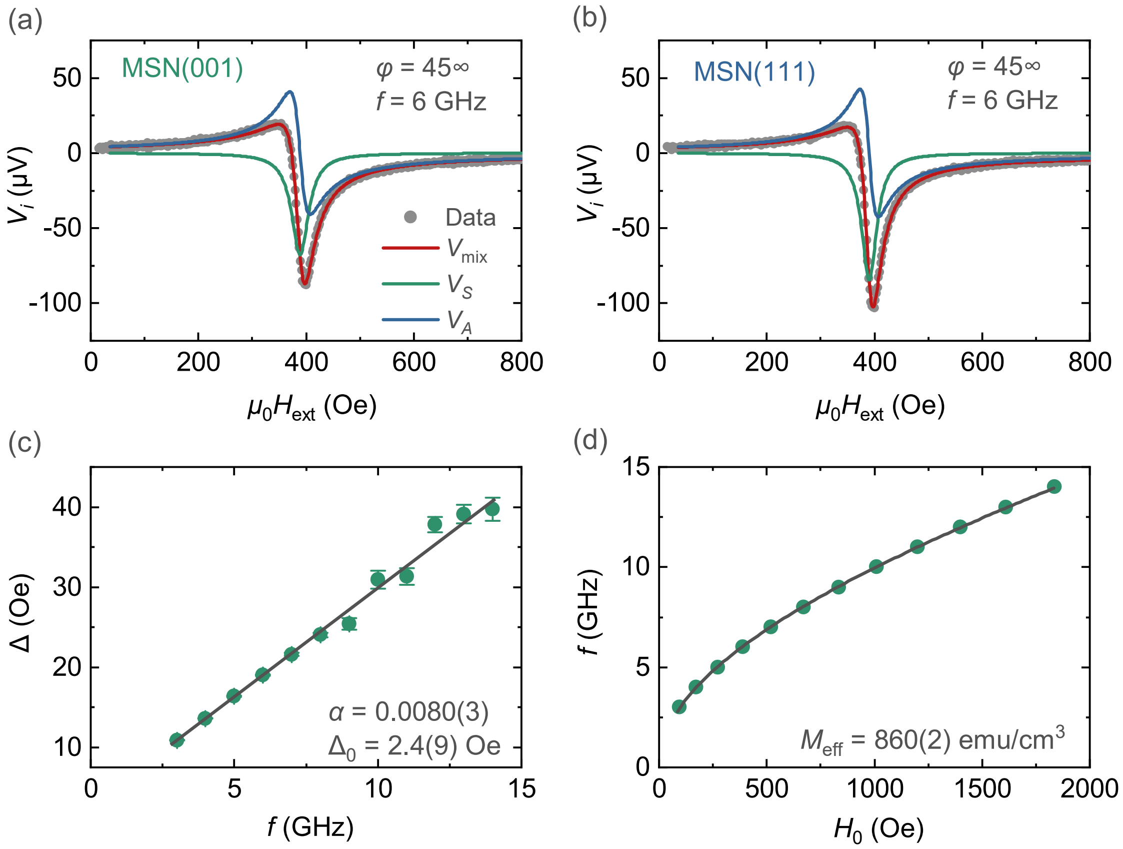

Figure A.2: Results from ST-FMR measurements of 20 nm thin (001)- and (111)-oriented Mn_3SnN/Cu/Py trilayer samples. Measured at a frequency of 6 GHz and at a field angle of 45°. (a), (b) Resonance spectra of (001)- and (111)-oriented samples and fitting of the mixing voltage by symmetric and antisymmetric Lorentzian functions. (c), (d) Frequency dependences of the linewidth broadening and of the resonance field in (001)-oriented MSN.

magnetization M_{eff} is extracted by fitting the dependence of the resonance field on the frequency, described by the Kittel equation:

$$f = \frac{\gamma\mu_0}{2\pi}\sqrt{H_0(H_0 + M_{\mathrm{eff}})} \tag{A.5}$$

The corresponding plot is shown in Figure A.2(d) for the (001)-oriented sample.

In order to investigate the spin torques with spin-rotational symmetry, i.e. spin torques due to spin currents with a spin polarization with components in x-, y- and z-direction, the field-angle dependence of V_S and V_A are investigated. This technique has mostly been used for the study of van-der-Waals materials with low crystal symmetry [197], but has recently also been applied to non-collinear antiferromagnets [27,178,198,199]. The angle dependences of V_S and V_A are given as:

$$V_S = -\frac{I_{\mathrm{RF}}}{2}\left(\frac{dR}{d\varphi}\right)\frac{1}{\alpha\mu_0(2H_0 + M_{\mathrm{eff}})}\cdot\tau_{\parallel} \tag{A.6}$$

$$V_A = -\frac{I_{\mathrm{RF}}}{2}\left(\frac{dR}{d\varphi}\right)\frac{\sqrt{1 + M_{\mathrm{eff}}/H_0}}{\alpha\mu_0(2H_0 + M_{\mathrm{eff}})}\cdot\tau_{\perp} \tag{A.7}$$

Herein, the angle-dependence of R is given by the AMR:

$$\frac{dR}{d\varphi} = R_{\mathrm{AMR}} \sin(2\varphi) \tag{A.8}$$

$\tau_{\|}$ and $\tau_{\perp}$ are torque components that are parallel and perpendicular to the film plane. In the presence of spin torques with x-, y- and z-component, there are three contributions in each direction:

$$\tau_{\|} = \tau_x^{\mathrm{AD}} \sin(\varphi) + \tau_y^{\mathrm{AD}} \cos(\varphi) + \tau_z^{\mathrm{FL}} \tag{A.9}$$

$$\tau_{\perp} = \tau_x^{\mathrm{FL}} \sin(\varphi) + \tau_y^{\mathrm{FL}} \cos(\varphi) + \tau_z^{\mathrm{AD}} \tag{A.10}$$

Herein, τ_i^{AD} describes an anti-damping-like (AD) torque components resulting from the component of the spin polarization in i-direction ($i = x, y, z$) and analogously for the FL components.

The angle-dependence of V_S and V_A was measured by repeatedly rotating the device to vary the angle φ between field and current and recording resonance spectra at each angle at a fixed frequency. The results for samples with both growth orientations are shown in Figure A.3

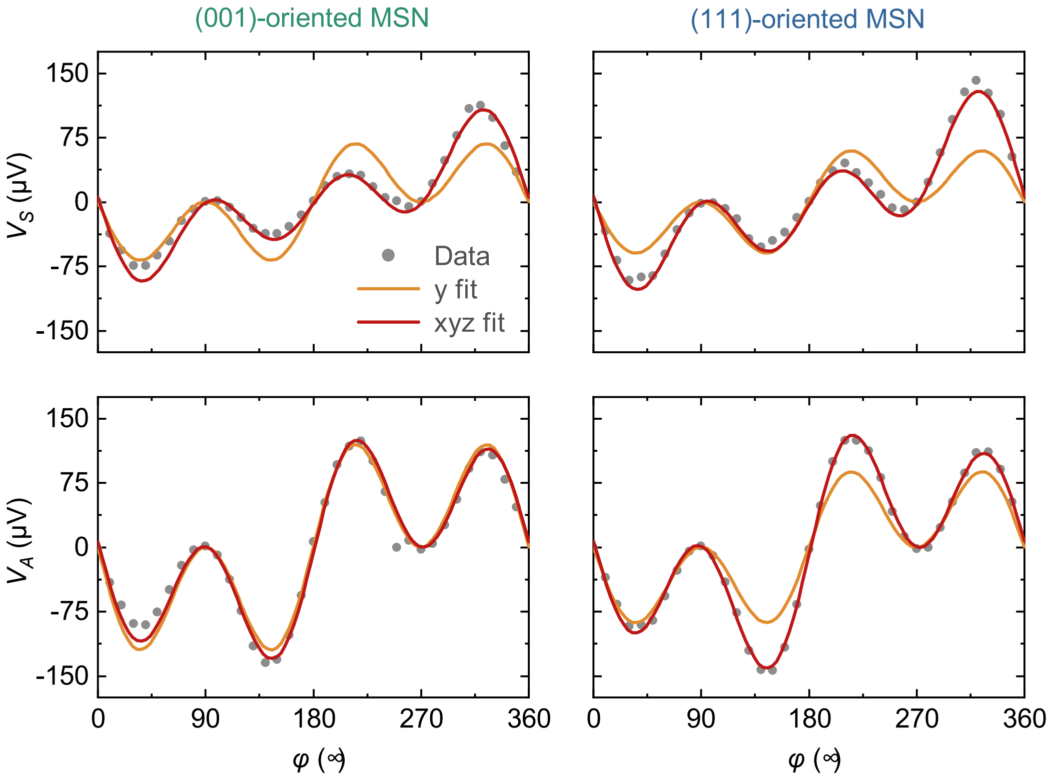

Figure A.3: Results from angle-dependent ST-FMR measurements to study the spin torques with spin-rotational symmetry. Field angle dependence of the symmetric and antisymmetric Lorentzian parts of the mixing voltage V_S (top row) and V_A (bottom row) in (001)-oriented (left column) and (111)-oriented (right column) Mn$_3$SnN (MSN). The data is fitted assuming spin torques resulting from spin currents with spin polarization in the y-direction (orange curve) as well as with spin-rotational symmetry (red curve).

It becomes evident that in samples with both growth orientations the angle-dependences of V_S and V_A cannot be fitted by assuming only the conventionally observed spin polarization in the y-direction. Proper fits are only achieved by considering spin torques resulting from a spin polarization with components in x-, y- and z-direction.

To extract the six torque components, the angle-dependences are fitted. The term $V_{\mathrm{AMR}} = -\frac{I_{\mathrm{RF}}}{2} R_{\mathrm{AMR}}$ in Equations A.6 and A.7 is taken as a fit parameter that couples the two equations. However, this requires that the torque components are normalized. The torque component τ_y^{FL} is chosen for the normalization, as it is assumed to be dominated by the Oersted field generated by the charge current. The normalized torque components for the differently oriented samples are presented in Figure A.4.

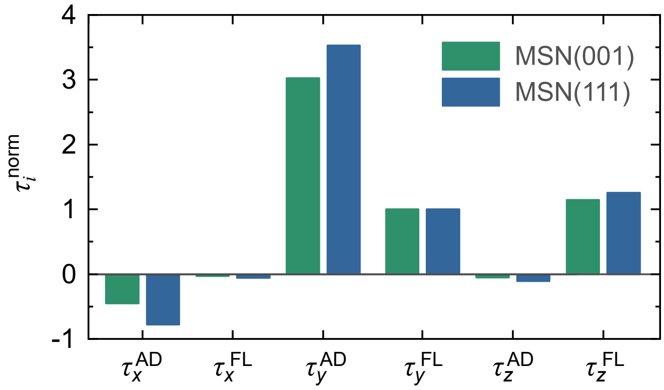

Figure A.4: Results from the fitting procedure of angle-dependent ST-FMR data of differently oriented Mn_3SnN/Cu/Py trilayer devices: Anti-damping-like (AD) and field-like (FL) spin torques resulting from spin currents with spin polarization in x-, y- and z-direction extracted from the angle-dependent ST-FMR measurements of differently oriented Mn_3SnN, normalized to τ_y^{FL}.

The presented results are inconclusive. There are two major inconsistencies to be discussed. First, it is unclear why the AD y-torque τ_y^{AD} is almost three times as large as its FL counterpart in both samples. Possibly, this is because of the large film thicknesses of MSN and Py of 20 nm and 10 nm. It was shown that at such large thicknesses the spin Hall efficiencies can be largely overestimated both in the presence of conventional y-directional spin torques as well as spin-rotational spin torques [200, 201].

Secondly, it becomes evident that the magnitudes of the torques are similar in (001)- and (111)-oriented MSN. Table A.1 shows the even parts of the spin conductivity tensor (i.e. the spin Hall conductivity tensor) in two coordinate systems.

System S corresponds to the case also shown in Table 10.3 (p. 105) in which the three-fold rotational axis $\bar{3}$ is along the [111] crystal axis. These tensors represent the ST-FMR measurement configuration for a (001)-oriented sample. Here, only the single-domain case is considered, the role of antiferromagnetic domains is discussed in Chapter 10.2.3 (p. 102). All three spin polarization directions are expected in the case of the (001)-oriented sample. These torques were previously found in (001)-oriented Mn_3Pt [180], Mn_3GaN [27] and Mn_3SnN [178].

Coordinate system S' corresponds to the case in which the rotational axis is along the [001] axis and describes (111)-oriented samples. From Table A.1 it can be seen that

Table A.1: Spin Hall conductivity tensors (even parts of the spin conductivity tensors) in the Γ^{4g} and Γ^{5g} configurations in two different coordinate systems. In system S: $\bar{3} \parallel [111]$, which corresponds to (001)-oriented samples. In system S': $\bar{3} \parallel [001]$, which corresponds to (111)-oriented samples. Marked in red are the components probed by ST-FMR.

	σ^x	σ^y	σ^z
S	$\begin{pmatrix} 0 & -\sigma^x_{xy} & \sigma^x_{xy} \\ \sigma^x_{yx} & -\sigma^x_{yy} & -\sigma^x_{yz} \\ -\sigma^x_{yx} & \sigma^x_{yz} & \sigma^x_{yy} \end{pmatrix}$	$\begin{pmatrix} \sigma^x_{yy} & -\sigma^x_{yx} & \sigma^x_{yz} \\ \sigma^x_{xy} & 0 & -\sigma^x_{xy} \\ -\sigma^x_{yz} & \sigma^x_{yx} & -\sigma^x_{yy} \end{pmatrix}$	$\begin{pmatrix} -\sigma^x_{yy} & -\sigma^x_{yz} & \sigma^x_{yx} \\ \sigma^x_{yz} & \sigma^x_{yy} & -\sigma^x_{yx} \\ -\sigma^x_{xy} & \sigma^x_{xy} & 0 \end{pmatrix}$
S'	$\begin{pmatrix} \sigma^x_{xx} & 0 & 0 \\ 0 & -\sigma^x_{xx} & \sigma^x_{yz} \\ 0 & \sigma^x_{zy} & 0 \end{pmatrix}$	$\begin{pmatrix} 0 & -\sigma^x_{xx} & -\sigma^x_{yz} \\ -\sigma^x_{xx} & 0 & 0 \\ -\sigma^x_{zy} & 0 & 0 \end{pmatrix}$	$\begin{pmatrix} 0 & \sigma^z_{xy} & 0 \\ -\sigma^z_{xy} & 0 & 0 \\ 0 & 0 & 0 \end{pmatrix}$

only the component of the spin Hall tensor with polarization in the y-direction are non-zero. The x- and z-type spin torques are forced to by zero by symmetry. The spin torque components measured in (111)-oriented MSN are not in agreement with this symmetry requirement. These spin torques have also been observed in (111)-oriented Mn_3Pt [180].

This discrepancy cannot be explained by potential artifact voltages, as they only affect the magnitude of the individual spin torques [201]. However, they cannot explain the presence of symmetry-forbidden spin torques. Another possible explanation is the effect of previously unexplored torques measured by ST-FMR. For instance, it cannot be excluded that the Cu spacer plays a role through the action of an orbital Hall effect [202, 203]. Another possibility is the presence of hidden magnetic symmetry lowering in the (111)-oriented sample. It is possible that such effect do not effect the anomalous Hall effect (AHE) measurements presented in the main body of this work. This is because the AHE is allowed by symmetry in (111)-oriented samples and the reason why no net effect is observed is because there is no mechanism allowing for domain structure control in these samples. However, as the AHE and the SHE behave differently under time reversal symmetry operations, it is possible that such symmetry lowering affects the two Hall effects differently.

In summary, a SHE with a spin-rotational polarization direction was found in (001)- and (111)-oriented MSN. The magnitude of the torques is likely overestimated because of the large layer thicknesses of MSN and Py. Furthermore, spin torques due to a spin polarization in x- and z-direction are observed that are unexpected in this growth orientation, as they are forbidden by the symmetry. It remain subject of further study to disclose the case of these unexpected spin torques.

Curriculum Vitae

Berthold Henry Rimmler

Contact details:
Max Planck Institute of Microstructure
Physics
Weinberg 2
06120 Halle
berthold.rimmler@mpi-halle.mpg.de

Education

2019 – 2023	Doctoral Candidate at Martin-Luther-Universität Halle-Wittenberg and Max Planck Institute of Microstructure Physics
2016 – 2019	Master student in double degree program "Functionalized Advanced Materials Engineering" at Institut polytechnique de Grenoble and Technische Universität Darmstadt
2013 – 2016	Bachelor student Materials Science at Technische Universität Darmstadt
2002 – 2013	Freie Waldorfschule Mannheim (Allgemeine Hochschulreife)

128

List of Figures

1.1 Potential applications of non-collinear antiferromagnets in spintronics . . 4

2.1 Schematic of a typical reactive DC sputtering setup 8
2.2 Common mechanisms for strain relaxation in epitaxial thin films 10
2.3 Common thin films growth modes 10
2.4 Schematic representation of the energy balance of a deposit on a substrate surface 11
2.5 Scattering of a X-ray beam from matter and the definition of the scattering vector 12
2.6 The atomic form factors of atomic sulfur, oxygen and the monovalent sodium ion as a function of the scattering vector 13
2.7 Geometric construction of Bragg's equation 14
2.8 Schematic representation of a single-crystal diffractometer with four-circle geometry 15
2.9 Schematic representation of a six-circle diffractometer with z-axis geometry 18
2.10 Photograph of the six-circle diffractometer used in this work 19
2.11 Schematic of a SQUID and macroscopic quantum interference 21
2.12 Components of a SQUID-VSM 21
2.13 The two-step absorption process in X-ray circular magnetic dichroism (XMCD) and exemplary X-ray absorption and XMCD spectra at the Co $L_{2,3}$ edge 23

3.1 Schematic representation of the intrinsic anomalous Hall effect and optical image of a double Hall bar device 26
3.2 The effect of mirror and time reversal symmetry operations on the non-collinear spin textures corresponding to the Γ^{5g} and Γ^{4g} configuration . . 28

4.1 Periodic table of elements showcasing the elements which form compounds with antiperovskite structures 31
4.2 Crystal structure representations of cubic Mn-based antiperovskites . . . 32
4.3 Crystallographic and magnetic phases of various antiperovskite nitrides . 33
4.4 Schematic representations of some crystal and magnetic structures found in Mn-based antiperovskite nitrides 34

4.5 Crystallographic and magnetic phases of Mn_3SnN bulk samples and graphical representations 36

4.6 The effect of a varying in-plane spin angle on the magnetic anisotropy and the anomalous Hall effect in NCAFs with antiperovskite structure . . 37

4.7 Examples of non-collinear coplanar spin textures with different vector spin chirality 38

4.8 Results of spin density calculations by Lukashev and Sabirianov 40

4.9 Three-sublattice model of NCAF order by Mochizuki *et al.* 41

6.1 Atomic force microscopic images of surfaces of (001)-oriented and (111)-oriented $SrTiO_3$ after substrate preparation. 50

6.2 Results of standard structural XRD characterization of 20 nm thin MSN films on (001)- and (111)-oriented STO. 52

6.3 Atomic force microscopic images and root-mean-square roughnesses of surfaces of 20 nm thin Mn_3SnN films with different growth orientations . 53

6.4 High resolution TEM, scanning TEM and Fast Fourier transform images of (001)- and (111)-oriented MSN films 54

6.5 Results of magnetometric characterization of (001)- and (111)-oriented MSN thin films by SQUID-VSM. 55

6.6 XMCD measurement of 20 nm thin (001)-oriented and (111)-oriented MSN films at 175 K 58

7.1 Longitudinal and transversal resistivity of 20 nm thin (001)- and (111)-oriented Mn_3SnN films 63

7.2 Anomalous Hall effect in (001)-oriented Mn_3SnN and comparison with magnetization data 64

7.3 Modeling the unusual temperature dependence in (001)-oriented Mn_3SnN by the presence of temperature-dependent spin rotation 66

8.1 Workflow of the structural refinement of antiperovskite nitride thin films . 73

8.2 Results of refinement of model structures with space group symmetry $P4/mmm$ (SGR No. 123) using the centrosymmetric atomic displacement parameter model and the split-sites model 76

8.3 Graphical representation of the crystal structure derived from refinement of the centrosymmetric model structures with $P4/mmm$ SGR symmetry and observed versus calculated squared structure factor amplitudes 77

8.4 Results of refinement of model structures with space group symmetry $P4mm$ (SGR No. 99) using the non-centrosymmetric atomic displacement parameter model and the shifted-sites model 80

8.5 Graphical representation of the crystal structure derived from refinement of the non-centrosymmetric model structures with $P4mm$ SGR symmetry and displacement magnitude and fit residuals at the Mn sites as a function of temperature and film thickness 81
8.6 Additional sections of the PDFs at the 2c and 1b site within the non-centrosymmetric atomic displacements parameter model 83
8.7 Isosurface plots of the PDFs within the non-centrosymmetric atomic displacement parameter model at the two different Mn sites in SGR $P4mm$. 84

9.1 Model structures to illustrate the emergence of canted moments in samples with tetragonal distortions and Mn displacements 86
9.2 The lattice Fourier transform of the exchange interactions in Mn_3SnN in the case of the cubic bulk structure and with Mn displacements at the two Mn sites 88
9.3 The relationships and dependencies of crystal structure, magnetism and magneto-transport effects in cubic NCAFs 90
9.4 Phase diagram of Mn_3SnN in bulk material and thin films 94

10.1 Graphical representations of the two types of non-collinear antiferromagnetic domains, shown for the Γ^{4g} configuration 102
10.3 Mn displacement magnitudes against lattice mismatch observed in Mn_3GaN grown on MgO(100) and Mn_3SnN grown on STO(100) 110
10.4 Directionality of net moments due to spin canting in the Γ^{4g} and Γ^{5g} configurations induced by tetragonal distortion and Mn displacements 111
10.5 Type II domains in the Γ^{5g} configuration viewed along the rotation axis . 112

A.1 Schematic showing the principle of spin-transfer ferromagnetic resonance (ST-FMR) 121
A.2 Results from ST-FMR measurements of 20 nm thin (001)- and (111)-oriented Mn_3SnN/Cu/Py trilayer samples 123
A.3 Results from angle-dependent ST-FMR measurements to study the spin torques with spin-rotational symmetry 124
A.4 Results from the fitting procedure of angle-dependent ST-FMR data of differently oriented Mn_3SnN/Cu/Py trilayer devices 125

List of Tables

3.1 Anomalous Hall conductivity tensors in the Γ^{5g} and Γ^{4g} spin configurations in two different coordinate systems, corresponding to samples grown with (111)- and (001)-orientation 27

4.1 Labeling of crystallographic structures found in Mn-based antiperovskites following the notation of Fruchart and Bertaut [72] 32

6.1 Optimized deposition parameters for Mn_3SnN thin films presented here . 51
6.2 Layer thicknesses and roughness of Mn_3SnN films, obtained from XRR and AFM 53
6.3 Summary of magnetic characterization by SQUID-VSM of Mn_3SnN thin films with different orientation and thickness at room temperature. 56
6.4 Normalized XMCD values and effective spin moments of different NCAFs 59

8.1 Refined structural parameters derived from least squares refinement of the bulk structure of Mn_3SnN with space group symmetry $Pm\bar{3}m$ to XRD data obtained from a 20 nm thin film at 300 K 75
8.2 Refined structural parameters derived from least squares refinement of the non-centrosymmetric atomic displacement parameter model 79
8.3 Summary of the structural models employed in the refinement of XRD data of (001)-oriented Mn_3SnN 82

9.1 Comparison of the AHE observed in Mn_3SnN and Mn_3Sn 92
9.2 List of antiperovskite nitrides that may be interesting for thin film investigation 95

10.1 Evenness and oddness of the contributions of χ^{I} and χ^{II} to the linear response of charge current and spin current to an applied electric field . . 102
10.2 Anomalous Hall conductivity tensors in the Γ^{5g} and Γ^{4g} configuration in the case of a single-domain state and averaged over four type II NCAF domains 103
10.3 Even and odd parts of the spin conductivity tensor in the Γ^{4g} and Γ^{5g} configurations in case of a single domain state and when averaged over four type II domains 105

10.4 Literature summary of works investigating magneto-transport properties of cubic non-collinear antiferromagnets and their structural parameters . . 107
10.5 Summary of the effect of non-collinear antiferromagnetic domains on several transport effects and experimental works investigating these effects . 113

A.1 Spin Hall conductivity tensors in the Γ^{4g} and Γ^{5g} configurations in two different coordinate systems corresponding to samples grown with (001)- and (111)-orientation. 126

Bibliography

[1] Dey, P. and Roy, J.N. *Spintronics: Fundamentals and Applications*. Springer Singapore (2021).

[2] Baltz, V., Manchon, A., Tsoi, M., Moriyama, T., Ono, T., and Tserkovnyak, Y. Antiferromagnetic spintronics. *Reviews of Modern Physics* **90**(1), 015005 (2018).

[3] Jungwirth, T., Marti, X., Wadley, P., and Wunderlich, J. Antiferromagnetic spintronics. *Nature Nanotechnology* **11**(3), 231–241 (2016).

[4] Šmejkal, L., Mokrousov, Y., Yan, B., and MacDonald, A.H. Topological antiferromagnetic spintronics. *Nature Physics* **14**(3), 242–251 (2018).

[5] Šmejkal, L., MacDonald, A.H., Sinova, J., Nakatsuji, S., and Jungwirth, T. Anomalous Hall antiferromagnets. *Nature Reviews Materials* **7**, 482–496 (2022).

[6] Parkin, S., Jiang, X., Kaiser, C., Panchula, A., Roche, K., and Samant, M. Magnetically engineered spintronic sensors and memory. *Proceedings of the IEEE* **91**(5), 661–680 (2003).

[7] Bhatti, S., Sbiaa, R., Hirohata, A., Ohno, H., Fukami, S., and Piramanayagam, S.N. Spintronics based random access memory: a review. *Materials Today* **20**(9), 530–548 (2017).

[8] Parkin, S.S.P., Hayashi, M., and Thomas, L. Magnetic Domain-Wall Racetrack Memory. *Science* **320**(5873), 190–194 (2008).

[9] Bläsing, R., Khan, A.A., Filippou, P.C., Garg, C., Hameed, F., Castrillon, J., and Parkin, S.S.P. Magnetic Racetrack Memory: From Physics to the Cusp of Applications Within a Decade. *Proceedings of the IEEE* **108**(8), 1303–1321 (2020).

[10] Šmejkal, L. and Jungwirth, T. Symmetry and Topology in Antiferromagnetic Spintronics. In J. Zang, V. Cros, and A. Hoffmann, editors, *Topology in Magnetism*, volume 192 of *Springer Series in Solid-State Sciences*. Springer International Publishing (2018).

[11] Shull, C.G., Strauser, W.A., and Wollan, E.O. Neutron Diffraction by Paramagnetic and Antiferromagnetic Substances. *Physical Review* **83**(2), 333–345 (1951).

[12] Fruchart, D. Magnetic properties of the metallic perovskite compounds $\mathrm{Mn_3}MX$. *Physica B+C* **86-88**, 423–425 (1977).

[13] Wang, Y., Zhang, H., Zhu, J., Lü, X., Li, S., Zou, R., and Zhao, Y. Antiperovskites with Exceptional Functionalities. *Advanced Materials* **32**(7), 1905007 (2020).

[14] Xiao, D., Chang, M.C., and Niu, Q. Berry phase effects on electronic properties. *Reviews of Modern Physics* **82**(3), 1959–2007 (2010).

[15] Nagaosa, N., Sinova, J., Onoda, S., MacDonald, A.H., and Ong, N.P. Anomalous Hall effect. *Reviews of Modern Physics* **82**(2), 1539–1592 (2010).

[16] Chen, H., Niu, Q., and MacDonald, A. Anomalous Hall Effect Arising from Noncollinear Antiferromagnetism. *Physical Review Letters* **112**(1), 017205 (2014).

[17] Kübler, J. and Felser, C. Non-collinear antiferromagnets and the anomalous Hall effect. *Europhysics Letters* **108**(6), 67001 (2014).

[18] Železný, J., Zhang, Y., Felser, C., and Yan, B. Spin-Polarized Current in Noncollinear Antiferromagnets. *Physical Review Letters* **119**(18), 187204 (2017).

[19] Gurung, G., Shao, D.F., and Tsymbal, E.Y. Transport spin polarization of noncollinear antiferromagnetic antiperovskites. *Physical Review Materials* **5**(12), 124411 (2021).

[20] Chen, X., Higo, T., Tanaka, K., Nomoto, T., Tsai, H., Idzuchi, H., Shiga, M., Sakamoto, S., Ando, R., Kosaki, H., Matsuo, T., Nishio-Hamane, D., Arita, R., Miwa, S., and Nakatsuji, S. Octupole-driven magnetoresistance in an antiferromagnetic tunnel junction. *Nature* **613**(7944), 490–495 (2023).

[21] Qin, P., Yan, H., Wang, X., Chen, H., Meng, Z., Dong, J., Zhu, M., Cai, J., Feng, Z., Zhou, X., Liu, L., Zhang, T., Zeng, Z., Zhang, J., Jiang, C., and Liu, Z. Room-temperature magnetoresistance in an all-antiferromagnetic tunnel junction. *Nature* **613**(7944), 485–489 (2023).

[22] Sinova, J., Valunzela, S.O., Wunderlich, J., Back, C.H., and Jungwirth, T. Spin Hall effects. *Reviews of Modern Physics* **87**(4), 1213–1260 (2015).

[23] Zhang, Y., Sun, Y., Yang, H., Železný, J., Parkin, S.P.P., Felser, C., and Yan, B. Strong anisotropic anomalous Hall effect and spin Hall effect in the chiral antiferromagnetic compounds $\mathrm{Mn_3}X$ (X = Ge, Sn, Ga, Ir, Rh, Pt). *Physical Review B* **95**(7), 075128 (2017).

[24] MacNeill, D., Stiehl, G.M., Guimaraes, M.H.D., Buhrman, R.A., Park, J., and Ralph, D.C. Control of spin–orbit torques through crystal symmetry in $\mathrm{WTe_2}$/ferromagnet bilayers. *Nature Physics* **13**(3), 300–305 (2017).

[25] Humphries, A.M., Wang, T., Edwards, E.R.J., Allen, S.R., Shaw, J.M., Nembach, H.T., Xiao, J.Q., Silva, T.J., and Fan, X. Observation of spin-orbit effects with spin rotation symmetry. *Nature Communications* **8**(1), 911 (2017).

[26] Baek, S.H.C., Amin, V.P., Oh, Y.W., Go, G., Lee, S.J., Lee, G.H., Kim, K.J., Stiles, M.D., Park, B.G., and Lee, K.J. Spin currents and spin-orbit torques in ferromagnetic trilayers. *Nature Materials* **17**(6), 509–513 (2018).

[27] Nan, T., Quintela, C.X., Irwin, J., Gurung, G., Shao, D.F., Gibbons, J., Campbell, N., Song, K., Choi, S.Y., Guo, L., Johnson, R.D., Manuel, P., Chopdekar, R.V., Hallsteinsen, I., Tybell, T., Ryan, P.J., Kim, J.W., Choi, Y., Radaelli, P.G., Ralph, D.C., Tsymbal, E.Y., Rzchowski, M.S., and Eom, C.B. Controlling spin current polarization through non-collinear antiferromagnetism. *Nature Communications* **11**(1), 4671 (2020).

[28] Sugimoto, S., Nakatani, Y., Yamane, Y., Ikhlas, M., Kondou, K., Kimata, M., Tomita, T., Nakatsuji, S., and Otani, Y. Electrical nucleation, displacement, and detection of antiferromagnetic domain walls in the chiral antiferromagnet Mn_3Sn. *Communications Physics* **3**(1), 1–9 (2020).

[29] Nakatsuji, S., Kiyohara, N., and Higo, T. Large anomalous Hall effect in a non-collinear antiferromagnet at room temperature. *Nature* **527**(7577), 212–215 (2015).

[30] Kiyohara, N., Tomita, T., and Nakatsuji, S. Giant Anomalous Hall Effect in the Chiral Antiferromagnet Mn_3Ge. *Physical Review Applied* **5**(6), 064009 (2016).

[31] Nayak, A.K., Fischer, J.E., Sun, Y., Yan, B., Karel, J., Komarek, A.C., Shekhar, C., Kumar, N., Schnelle, W., Kübler, J., Felser, C., and Parkin, S.S.P. Large anomalous Hall effect driven by a nonvanishing Berry curvature in the noncolinear antiferromagnet Mn_3Ge. *Science Advances* **2**(4), e1501870 (2016).

[32] Liu, Z.Q., Chen, H., Wang, J.M., Liu, J.H., Wang, K., Feng, Z.X., Yan, H., Wang, X.R., Jiang, C.B., Coey, J.M.D., and MacDonald, A.H. Electrical switching of the topological anomalous Hall effect in a non-collinear antiferromagnet above room temperature. *Nature Electronics* **1**(3), 172–177 (2018).

[33] Boldrin, D., Samathrakis, I., Zemen, J., Mihai, A., Zou, B., Johnson, F., Esser, B.D., McComb, D.W., Petrov, P.K., Zhang, H., and Cohen, L.F. Anomalous Hall effect in noncollinear antiferromagnetic Mn_3NiN thin films. *Physical Review Materials* **3**(9), 094409 (2019).

[34] You, Y., Bai, H., Chen, X., Zhou, Y., Zhou, X., Pan, F., and Song, C. Room temperature anomalous Hall effect in antiferromagnetic Mn_3SnN films. *Applied Physics Letters* **117**(22), 222404 (2020).

[35] Johnson, F., Kimák, J., Zemen, J., Šobáň, Z., Schmoranzerová, E., Godinho, J., Němec, P., Beckert, S., Reichlová, H., Boldrin, D., Wunderlich, J., and Cohen,

L.F. Identifying the octupole antiferromagnetic domain orientation in Mn_3NiN by scanning anomalous Nernst effect microscopy. *Applied Physics Letters* **120**(23), 232402 (2022).

[36] Rimmler, B.H., Hazra, B.K., Pal, B., Mohseni, K., Taylor, J.M., Bedoya-Pinto, A., Deniz, H., Tangi, M., Kostanovskiy, I., Luo, C., Neumann, R.R., Ernst, A., Radu, F., Mertig, I., Meyerheim, H.L., and Parkin, S.S.P. Atomic Displacements Enabling the Observation of the Anomalous Hall Effect in a Non-Collinear Antiferromagnet. *Advanced Materials* **35**(23), 2209616 (2023).

[37] Harsha, K.S. *Principles of Vapor Deposition of Thin Films*. Elsevier Ltd. (2006).

[38] Lüth, H. *Solid Surfaces, Interfaces and Thin Films*. Graduate Texts in Physics. Springer, Heidelberg, 5. edition (2010).

[39] Wutz, M., Adam, H., Walcher, W., and Jousten, K. *Handbuch Vakuumtechnik: Theorie und Praxis*. Viewg & Sohn, 7. edition (2000).

[40] Pansila, P.P., Witit-Anun, N., Jamnongkan, T., and Chaiyakun, S. Preparation of Pure Anatase TiO_2 Thin Films by DC Sputtering Technique: Study on the Effect of Oxygen Partial Pressure. *Advanced Materials Research* **463-464**, 1415–1419 (2012).

[41] Rimmler, B.H. *3d-5d Double perovskites $Sr_2CrB''O_6$ (B" = Re, Os) in Pulsed Laser Deposition*. Master's thesis, TU Darmstadt (2019).

[42] Cullity, B. *Elements of X-Ray Diffraction*. Addison-Wesley Publishing Company (1956).

[43] Spieß, L. *Moderne Röntgenbeugung: Röntgendiffraktometrie für Materialwissenschaftler, Physiker und Chemiker*. Vieweg + Teubner, Wiesbaden, 2. revised and enlarged edition (2009).

[44] Als-Nielsen, J. and McMorrow, D. *Elements of Modern X-ray Physics*. John Wiley & Sons, Inc., Hoboken, NJ, USA, 2. edition (2011).

[45] Prince, E. and of Crystallography., I.U. *International tables for crystallography. Volume C: Mathematical, physical and chemical tables*. Dordrecht, London (2006).

[46] Blanton, T.N. and Hoople, C.R. X-ray diffraction analysis of ultrathin platinum silicide films deposited on (100) silicon. *Powder Diffraction* **17**(1), 7–9 (2002).

[47] Kriegner, D., Wintersberger, E., and Stangl, J. xrayutilities: a versatile tool for reciprocal space conversion of scattering data recorded with linear and area detectors. *Journal of Applied Crystallography* **46**(4), 1162–1170 (2013).

[48] Moritz, W. and Van Hove, M.A. *Surface Structure Determination by LEED and X-rays*. Cambridge University Press (2022).

[49] Lohmeier, M. and Vlieg, E. Angle calculations for a six-circle surface X-ray diffractometer. *Journal of Applied Crystallography* **26**(5), 706–716 (1993).

[50] Robach, O., Garreau, Y., Aïd, K., and Véron-Jolliot, M.B. Corrections for surface X-ray diffraction measurements using the Z-axis geometry: finite size effects in direct and reciprocal space. *Journal of Applied Crystallography* **33**(4), 1006–1018 (2000).

[51] Clarke, J. and Braginski, A.I., editors. *The SQUID Handbook. Vol. I: Fundamentals and Technology of SQUIDs and SQUID Systems*. Wiley-VCH, Weinheim (2004).

[52] Fagaly, R.L. Superconducting quantum interference device instruments and applications. *Review of Scientific Instruments* **77**(10), 101101 (2006).

[53] Kittel, C. *Introduction to solid state physics*. Wiley, Hoboken, NJ, 8th ed edition (2005).

[54] Wende, H. and Antoniak, C. X-Ray Magnetic Dichroism. In E. Beaurepaire, H. Bulou, F. Scheurer, and J.P. Kappler, editors, *Magnetism and Synchrotron Radiation*. Springer-Verlag Berlin Heidelberg (2010).

[55] van der Laan, G. and Figueroa, A.I. X-ray magnetic circular dichroism – A versatile tool to study magnetism. *Coordination Chemistry Reviews* **277-278**, 95–129 (2014).

[56] Ashcroft, N.W. and Mermin, N.D. *Solid State Physics*. Saunders College Publishing (1976).

[57] Karplus, R. and Luttinger, J.M. Hall Effect in Ferromagnetics. *Physical Review* **95**(5), 1154–1160 (1954).

[58] Berry, M.V. Quantal phase factors accompanying adiabatic changes. *Proceedings of the Royal Society of London. A. Mathematical and Physical Sciences* **392**(1802), 45–57 (1984).

[59] Gradhand, M., Fedorov, D.V., Pientka, F., Zahn, P., Mertig, I., and Györffy, B.L. First-principle calculations of the Berry curvature of Bloch states for charge and spin transport of electrons. *Journal of Physics: Condensed Matter* **24**(21), 213202 (2012).

[60] Grimmer, H. General relations for transport properties in magnetically ordered crystals. *Acta Crystallographica Section A: Foundations of Crystallography* **49**(5), 763–771 (1993).

[61] Gurung, G., Shao, D.F., Paudel, T.R., and Tsymbal, E.Y. Anomalous Hall conductivity of noncollinear magnetic antiperovskites. *Physical Review Materials* **3**(4), 044409 (2019).

[62] Suzuki, M.T., Koretsune, T., Ochi, M., and Arita, R. Cluster multipole theory for anomalous Hall effect in antiferromagnets. *Physical Review B* **95**(9), 094406 (2017).

[63] Wiberg, E. and Wiberg, N. *Lehrbuch der anorganischen Chemie*. Walter de Gruyter, Berlin, New York, 102. edition (2007).

[64] Blundell, S. *Magnetism in Condensed Matter*. Oxford master series in condensed matter physics. Oxford university press, 1. edition (2001).

[65] Coey, J. *Magnetism and Magnetic Materials*. Cambridge University Press (2009).

[66] Coey, J.M.D., Givord, D., and Fruchart, D. Metallic Nitride and Carbide Perovskites: History and Prospects. *ECS Journal of Solid State Science and Technology* **11**(5), 055002 (2022).

[67] Momma, K. and Izumi, F. VESTA 3 for three-dimensional visualization of crystal, volumetric and morphology data. *Journal of Applied Crystallography* **44**(6), 1272–1276 (2011).

[68] Goodenough, J.B. Metallic oxides. *Progress in Solid State Chemistry* **5**, 145–399 (1971).

[69] Zhou, Y., Kanoda, K., and Ng, T.K. Quantum spin liquid states. *Reviews of Modern Physics* **89**(2), 025003 (2017).

[70] Shaginyan, V.R., Stephanovich, V.A., Msezane, A.Z., Japaridze, G.S., Clark, J.W., Amusia, M.Y., and Kirichenko, E.V. Theoretical and experimental developments in quantum spin liquid in geometrically frustrated magnets: a review. *Journal of Materials Science* **55**(6), 2257–2290 (2020).

[71] Barberon, M., Madar, R., Fruchart, M.E., Lorthioir, G., and Fruchart, R. Les deformations quadratiques T_1 et T_4 dans les carbures et nitrures perowskites du manganese. *Materials Research Bulletin* **5**(1), 1–7 (1970).

[72] Fruchart, D. and Bertaut, E.F. Magnetic Studies of the Metallic Perovskite-Type Compounds of Manganese. *Journal of the Physical Society of Japan* **44**(3), 781–791 (1978).

[73] Takei, W.J., Shirane, G., and Frazer, B.C. Magnetic Structure of Mn_4N. *Physical Review* **119**(1), 122–126 (1960).

[74] Takei, W.J., Heikes, R.R., and Shirane, G. Magnetic Structure of Mn_4N-Type Compounds. *Physical Review* **125**(6), 1893–1897 (1962).

[75] Kuriyama, M., Hosoya, S., and Suzuki, T. Electron Number of the Nitrogen Atom in Mn_4N. *Physical Review* **130**(3), 898–899 (1963).

[76] Mekata, M., Haruna, J., and Takaki, H. Localized Magnetic Moments in Mn_4N. *Journal of the Physical Society of Japan* **21**(11), 2267–2273 (1966).

[77] Bouchaud, J.P. *Contribution à l'étude du système manganèse-carbone et des perowskites métalliques du manganèse*. Thèse de doctorat d'Etat, Paris (1967). No. C.N.R.S.: 1592.

[78] Fruchart, M.R., Bouchaud, J.P., Fruchart, M.E., Lorthioir, M.G., Madar, R., and Rouault, A. Sur les transitions magnetiques du premier ordre dans les perowskites metalliques du manganese. *Materials Research Bulletin* **2**(11), 1009–1020 (1967).

[79] Bertaut, E.F., Fruchart, D., Bouchaud, J.P., and Fruchart, R. Diffraction neutronique de Mn_3GaN. *Solid State Communications* **6**(5), 251–256 (1968).

[80] Barberon, M., Madar, R., Fruchart, E., Lorthioir, G., and Fruchart, R. Etude du facteur de diffusion de l'azote dans la solution solide Mn_4N-$GaMn_3N$. *Materials Research Bulletin* **5**(11), 903–912 (1970).

[81] Madar, R. *Contribution à l'étude des transitions magnétiques du premier ordre des nitrures métalliques du manganèse de type perowskite*. Thèse de doctorat d'Etat, Orsay (1970). No. C.N.R.S.: 686.

[82] Fruchart, D., Bertaut, E.F., Madar, R., and Fruchart, R. Diffraction neutronique de Mn_3ZnN. *Le Journal de Physique Colloques* **32**(C1), 876 (1971).

[83] Fruchart, D., Bertaut, E.F., Madar, R., Lorthioir, G., and Fruchart, R. Structure magnetique et rotation de spin de Mn_3NiN. *Solid State Communications* **9**(21), 1793–1797 (1971).

[84] Fruchart, R., Madar, R., Barberon, M., Fruchart, E., and Lorthioir, M.G. Transitions magnétiques et déformations cristallographiques associées dans les nitrures du type perowskite $ZnMn_3N$ et $SnMn_3N$. *Le Journal de Physique Colloques* **32**(C1), C1–982–C1–984 (1971).

[85] Barberon, M., Fruchart, E., Fruchart, R., Lorthioir, G., Madar, R., and Nardin, M. Un nouveau type de deformation orthorhombique dans les perovskites metalliques. *Materials Research Bulletin* **7**(2), 109–118 (1972).

[86] Bertaut, E.F. and Fruchart, D. Rotation des moments magnetiques du manganese dans Mn_3NiN. *International Journal of Magnetism* **2**, 259–264 (1972).

[87] Nardin, M., Lorthioir, G., Barberon, M., Fruchart, F., and Fruchart, R. Étude de cinq nouveaux nitrures MCr_3N de type perovskite. *Comptes rendus hebdomadaires des séances de l'académie des sciences* **274**, 4 (1972).

[88] Barberon, M. *Transformations cristallographiques et transitions magnétiques des perowskites métalliques du manganèse MMn_3N (M = Ge, Sn, As, Sb)*. Thèse de doctorat d'Etat, Paris (1973). No. C.N.R.S.: 702.

[89] Fruchart, D., Madar, R., Fruchart, E., and Fruchart, R. Structure et Comportement Magnetique de Mn_3CuN et Mn_3SnC. *Int. Kern. Kerntechn* **8A**, 1326–1330 (1973).

[90] Fruchart, D. and Bertaut, E.F. Magnetic behavior of the perovskite-type compound: Mn_3AgN. *Proceedings of the International Conference on Magnetism* **4**, 572 (1974).

[91] Fruchart, D. *Etudes par diffraction neutronique des perovskites metalliques Mn_3MX, carbures (X=C; M = Zn, Ga, Sn), nitrures (X = N; M = Ni, Cu, Zn, Ga, Rh, Ag, Sn, Sb, Pt).* Thèse de doctorat d'Etat, Grenoble INP (1976). No. C.N.R.S.: 11922.

[92] Fruchart, D., Bertaut, E.F., Sénateur, J.P., and Fruchart, R. Magnetic studies on the metallic perovskite-type compound Mn_3SnN. *Journal de Physique Lettres* **38**(1), 21–23 (1977).

[93] l'Héritier, P., Boursier, D., Fruchart, R., and Fruchart, D. Structures magnetiques et transitions du premier ordre dans les perovskites metalliques $GaMn_3(C_{1-x}N_x)$. Relation avec les composes de terres rares a changement de valence. *Materials Research Bulletin* **14**(9), 1203–1212 (1979).

[94] l'Héritier, P., Fruchart, D., Madar, R., and Fruchart, R. Instabilites electroniques dans les composes du manganese de type perovskite metallique. Relation avec les changements de valence dans les composes de terres rares. *Materials Research Bulletin* **14**(8), 1089–1094 (1979).

[95] Fruchart, D., L'Héritier, P., and Fruchart, R. Transformations de phases dans les nitrures et carbures du manganese de structure-type perovskite. *Materials Research Bulletin* **15**(4), 415–420 (1980).

[96] L'Héritier, P. *Etude expérimentale des instabilités électroniques dans les carbures et nitrures ternaires du manganèse de type pérovskite*. Thèse de doctorat d'Etat, Grenoble INP (1980). No. C.N.R.S.: DE 95.

[97] Sun, Y., Wang, C., Huang, Q., Guo, Y., Chu, L., Arai, M., and Yamaura, K. Neutron Diffraction Study of Unusual Phase Separation in the Antiperovskite Nitride Mn_3ZnN. *Inorganic Chemistry* **51**(13), 7232–7236 (2012).

[98] Sun, Y.S., Guo, Y.F., Wang, X.X., Yi, W., Li, J.J., Zhang, S.B., Sathish, C.I., Belik, A.A., and Yamaura, K. Magnetic and electrical properties of antiperovskite Mn_3InN synthesized by a high-pressure method. *Journal of Physics: Conference Series* **400**(3), 032094 (2012).

[99] Wu, M., Wang, C., Sun, Y., Chu, L., Yan, J., Chen, D., Huang, Q., and Lynn, J.W. Magnetic structure and lattice contraction in Mn_3NiN. *Journal of Applied Physics* **114**(12), 123902 (2013).

[100] Takenaka, K., Ichigo, M., Hamada, T., Ozawa, A., Shibayama, T., Inagaki, T., and Asano, K. Magnetovolume effects in manganese nitrides with antiperovskite structure. *Science and Technology of Advanced Materials* **15**(1), 015009 (2014).

[101] Boldrin, D., Mendive-Tapia, E., Zemen, J., Staunton, J.B., Hansen, T., Aznar, A., Tamarit, J.L., Barrio, M., Lloveras, P., Kim, J., Moya, X., and Cohen, L.F. Multisite Exchange-Enhanced Barocaloric Response in Mn_3NiN. *Physical Review X* **8**(4), 041035 (2018).

[102] Tan, S., Gao, C., Yuan, H., Wu, J., Wang, C., Cao, R., and Sun, Y. An antiperovskite compound with multifunctional properties: Mn_3PdN. *Journal of Solid State Chemistry* **302**, 122389 (2021).

[103] He, Y., Lenne, S., Gercsi, Z., Atcheson, G., O'Brien, J., Fruchart, D., Rode, K., and Coey, J.M.D. Noncollinear ferrimagnetism and anomalous Hall effects in Mn_4N thin films. *Physical Review B* **106**(6), L060409 (2022).

[104] Gomonaj, E.V. and L'vov, V.A. Phenomenologic study of phase transitions in noncollinear antiferromagnets of metallic perovskite type. *Phase Transitions* **38**(1), 15–31 (1992).

[105] Gomonaj, E.V. and L'vov, V.A. A theory of spin reorientation and piezomagnetic effect in noncollinear Mn_3AgN antiferromagnet. *Phase Transitions* **40**(1-4), 225–237 (1992).

[106] Krén, E., Kádár, G., Pál, L., Sólyom, J., and Szabó, P. Magnetic structures and magnetic transformations in ordered Mn_3(Rh, Pt) alloys. *Physics Letters* **20**(4), 331–332 (1966).

[107] Krén, E., Kádár, G., Pál, L., Sólyom, J., Szabó, P., and Tarnóczi, T. Magnetic Structures and Exchange Interactions in the Mn-Pt System. *Physical Review* **171**(2), 574–585 (1968).

[108] Tomeno, I., Fuke, H.N., Iwasaki, H., Sahashi, M., and Tsunoda, Y. Magnetic neutron scattering study of ordered Mn_3Ir. *Journal of Applied Physics* **86**(7), 3853–3856 (1999).

[109] Sticht, J., ck, K.H.H., and bler, J.K. Non-collinear itinerant magnetism: the case of Mn_3Sn. *Journal of Physics: Condensed Matter* **1**(43), 8155–8176 (1989).

[110] Zhou, X., Hanke, J.P., Feng, W., Li, F., Guo, G.Y., Yao, Y., Blügel, S., and Mokrousov, Y. Spin-order dependent anomalous Hall effect and magneto-optical effect in the noncollinear antiferromagnets Mn_3XN with X = Ga, Zn, Ag, or Ni. *Physical Review B* **99**(10), 104428 (2019).

[111] Busch, O., Göbel, B., and Mertig, I. Microscopic origin of the anomalous Hall effect in noncollinear kagome magnets. *Physical Review Research* **2**(3), 033112 (2020).

[112] Kawamura, H. Spin- and chirality-orderings of frustrated magnets stacked-triangular anti-ferromagnets and spin glasses. *Canadian Journal of Physics* **79**(11-12), 1447–1458 (2001).

[113] Zhang, Z. and Mi, W. Progress in ferrimagnetic Mn_4N films and its heterostructures for spintronics applications. *Journal of Physics D: Applied Physics* **55**(1), 013001 (2021).

[114] Abe, H., Matsuura, M., Hirai, A., Haruna, J., and Mekata, M. Nuclear Magnetic Resonances of Mn^{55} and N^{14} in Ferrimagnetic Intermetallic Mn_4N - Anisotropic and Transferred Hyperfine Fields in Intermetallic Compound. *Journal of the Physical Society of Japan* **22**(2), 558–572 (1967).

[115] Nagakura, S., Ōtsuka, N., and Hirotsu, Y. Electron State of Ni_4N Studied by Electron Diffraction. *Journal of the Physical Society of Japan* **35**(5), 1492–1495 (1973).

[116] Jardin, J.P. and Labbé, J. Modèle pour la structure électronique des composés perovskites du manganèse. *Journal de Physique* **36**(12), 1317–1326 (1975).

[117] Jardin, J.P. and Labbe, J. Phase transitions and band structure in metallic perovskites (carbides and nitrides). *Journal of Solid State Chemistry* **46**(3), 275–293 (1983).

[118] Zemen, J., Gercsi, Z., and Sandeman, K.G. Piezomagnetism as a counterpart of the magnetovolume effect in magnetically frustrated Mn-based antiperovskite nitrides. *Physical Review B* **96**(2), 024451 (2017).

[119] Yu, R., Chong, X., Jiang, Y., Zhou, R., Yuan, W., and Feng, J. The stability, electronic structure, elastic and metallic properties of manganese nitrides. *RSC Advances* **5**(2), 1620–1627 (2015).

[120] Chen, S., Tong, P., Wu, J., Wang, W.H., and Wang, W. Electronic structures and crystal field splitting of antiperovskite $X\mathrm{NMn}_3$ (X=3d and 4d elements). *Computational Materials Science* **132**, 132–136 (2017).

[121] Antonov, V.N. and Bekenov, L.V. Electronic structure and x-ray magnetic circular dichroism in the Mn_3CuN perovskite. *Low Temperature Physics* **40**(7), 641–648 (2014).

[122] Mekata, M. Magnetic Study on Mn_4N and its Related Compounds. *Journal of the Physical Society of Japan* **17**(5), 796–803 (1962).

[123] Lukashev, P. and Sabirianov, R.F. Spin density in frustrated magnets under mechanical stress: Mn-based antiperovskites. *Journal of Applied Physics* **107**(9), 09E115 (2010).

[124] Mochizuki, M., Kobayashi, M., Okabe, R., and Yamamoto, D. Spin model for nontrivial types of magnetic order in inverse-perovskite antiferromagnets. *Physical Review B* **97**(6), 060401 (2018).

[125] Biswas, A., Yang, C.H., Ramesh, R., and Jeong, Y.H. Atomically flat single terminated oxide substrate surfaces. *Progress in Surface Science* **92**(2), 117–141 (2017).

[126] Wang, Y. and Nastasi, M. *Handbook of modern ion beam materials analysis*. Materials Research Society (2009).

[127] Quintela, C.X., Song, K., Shao, D.F., Xie, L., Nan, T., Paudel, T.R., Campbell, N., Pan, X., Tybell, T., Rzchowski, M.S., Tsymbal, E.Y., Choi, S.Y., and Eom, C.B. Epitaxial antiperovskite/perovskite heterostructures for materials design. *Science Advances* **6**(30), eaba4017 (2020).

[128] Coey, J.M.D., Venkatesan, M., and Stamenov, P. Surface magnetism of strontium titanate. *Journal of Physics: Condensed Matter* **28**(48), 485001 (2016).

[129] Quantum Design. VSM Sample Mounting Techniques: Application Note 1096-306 (2009).

[130] Taylor, J.M., Markou, A., Lesne, E., Sivakumar, P.K., Luo, C., Radu, F., Werner, P., Felser, C., and Parkin, S.S.P. Anomalous and topological Hall effects in epitaxial thin films of the noncollinear antiferromagnet Mn_3Sn. *Physical Review B* **101**(9), 094404 (2020).

[131] Taylor, J.M., Lesne, E., Markou, A., Dejene, F.K., Sivakumar, P.K., Pöllath, S., Rana, K.G., Kumar, N., Luo, C., Ryll, H., Radu, F., Kronast, F., Werner, P., Back, C.H., Felser, C., and Parkin, S.S.P. Magnetic and electrical transport signatures of uncompensated moments in epitaxial thin films of the noncollinear antiferromagnet Mn_3Ir. *Applied Physics Letters* **115**(6), 062403 (2019).

[132] Wang, X., Pan, D., Zeng, Q., Chen, X., Wang, H., Zhao, D., Xu, Z., Yang, Q., Deng, J., Zhai, T., Wu, G., Liu, E., and Zhao, J. Robust anomalous Hall effect and temperature-driven Lifshitz transition in Weyl semimetal Mn_3Ge. *Nanoscale* **13**(4), 2601–2608 (2021).

[133] Pal, B., Hazra, B.K., Göbel, B., Jeon, J.C., Pandeya, A.K., Chakraborty, A., Busch, O., Srivastava, A.K., Deniz, H., Taylor, J.M., Meyerheim, H., Mertig, I., Yang, S.H., and Parkin, S.S.P. Setting of the magnetic structure of chiral kagome antiferromagnets by a seeded spin-orbit torque. *Science Advances* **8**(24), eabo5930 (2022).

[134] Lukashev, P., Sabirianov, R.F., and Belashchenko, K. Theory of the piezomagnetic effect in Mn-based antiperovskites. *Physical Review B* **78**(18), 184414 (2008).

[135] Zucker, U.H., Perenthaler, E., Kuhs, W.F., Bachmann, R., and Schulz, H. PROMETHEUS. A program system for investigation of anharmonic thermal vibrations in crystals. *Journal of Applied Crystallography* **16**(3), 358–358 (1983).

[136] Abrahams, S.C. Indicators of accuracy in structure factor measurement. *Acta Crystallographica Section A: Crystal Physics, Diffraction, Theoretical and General Crystallography* **25**(1), 165–173 (1969).

[137] Robinson, I. Surface Crystallography. In G. Brown and D. Moncton, editors, *Handbook on Synchrotron Radiation*, volume 3, pages 221–266. Elsevier Science Publishers B. V., North-Holland (1991).

[138] Zucker, U.H. and Schulz, H. Statistical approaches for the treatment of anharmonic motion in crystals. I. A comparison of the most frequently used formalisms of anharmonic thermal vibrations. *Acta Crystallographica Section A: Crystal Physics, Diffraction, Theoretical and General Crystallography* **38**(5), 563–568 (1982).

[139] Zucker, U.H. and Schulz, H. Statistical approaches for the treatment of anharmonic motion in crystals. II. Anharmonic thermal vibrations and effective atomic potentials in the fast ionic conductor lithium nitride (Li_3N). *Acta Crystallographica Section A: Crystal Physics, Diffraction, Theoretical and General Crystallography* **38**(5), 568–576 (1982).

[140] Kuhs, W.F. Generalized atomic displacements in crystallographic structure analysis. *Acta Crystallographica Section A: Foundations of Crystallography* **48**(2), 80–98 (1992).

[141] Ederly, A. *Higher Transcendental Functions*, volume 3. McGraw-Hill, New York (1953).

[142] Perenthaler, E. and Schulz, H. Anharmonic temperature factors up to sixth order and atomic potentials in the fast ionic conductor α-Ag_3SI. *Solid State Ionics* **2**(1), 43–46 (1981).

[143] Takenaka, K. and Takagi, H. Giant negative thermal expansion in Ge-doped anti-perovskite manganese nitrides. *Applied Physics Letters* **87**(26), 261902 (2005).

[144] Iikubo, S., Kodama, K., Takenaka, K., Takagi, H., and Shamoto, S. Magnetovolume effect in $Mn_3Cu_{1-x}Ge_xN$ related to the magnetic structure: Neutron powder diffraction measurements. *Physical Review B* **77**(2), 020409 (2008).

[145] Qu, B.Y. and Pan, B.C. Nature of the negative thermal expansion in antiperovskite compound Mn_3ZnN. *Journal of Applied Physics* **108**(11), 113920 (2010).

[146] Sun, Y., Wang, C., Wen, Y., Chu, L., Pan, H., Nie, M., and Tang, M. Negative Thermal Expansion and Magnetic Transition in Anti-Perovskite Structured

$Mn_3Zn_{1-x}Sn_xN$ Compounds. *Journal of the American Ceramic Society* **93**(8), 2178–2181 (2010).

[147] Qu, B.Y., He, H.Y., and Pan, B.C. Origin of the Giant Negative Thermal Expansion in $Mn_3(Cu_{0.5}Ge_{0.5})N$. *Advances in Condensed Matter Physics* **2012**, 1–7 (2012).

[148] Deng, S., Sun, Y., Wu, H., Huang, Q., Yan, J., Shi, K., Malik, M.I., Lu, H., Wang, L., Huang, R., Li, L., and Wang, C. Invar-like Behavior of Antiperovskite $Mn_{3+x}Ni_{1-x}N$ Compounds. *Chemistry of Materials* **27**(7), 2495–2501 (2015).

[149] Sun, Y., Wang, C., Chu, L., Wen, Y., Nie, M., and Liu, F. Low temperature coefficient of resistivity induced by magnetic transition and lattice contraction in Mn_3NiN compound. *Scripta Materialia* **62**(9), 686–689 (2010).

[150] Ding, L., Wang, C., Chu, L., Yan, J., Na, Y., Huang, Q., and Chen, X. Near zero temperature coefficient of resistivity in antiperovskite $Mn_3Ni_{1-x}Cu_xN$. *Applied Physics Letters* **99**(25), 251905 (2011).

[151] Asano, K., Koyama, K., and Takenaka, K. Magnetostriction in Mn_3CuN. *Applied Physics Letters* **92**(16), 161909 (2008).

[152] Shimizu, T., Shibayama, T., Asano, K., and Takenaka, K. Giant magnetostriction in tetragonally distorted antiperovskite manganese nitrides. *Journal of Applied Physics* **111**(7), 07A903 (2012).

[153] Takenaka, K., Hamada, T., Shibayama, T., and Asano, K. Ferromagnetic shape memory effects in tetragonally distorted antiperovskite manganese nitrides. *Journal of Alloys and Compounds* **577**, S291–S295 (2013).

[154] Yan, J., Sun, Y., Wu, H., Huang, Q., Wang, C., Shi, Z., Deng, S., Shi, K., Lu, H., and Chu, L. Phase transitions and magnetocaloric effect in $Mn_3Cu_{0.89}N_{0.96}$. *Acta Materialia* **74**, 58–65 (2014).

[155] Shi, K., Sun, Y., Yan, J., Deng, S., Wang, L., Wu, H., Hu, P., Lu, H., Malik, M.I., Huang, Q., and Wang, C. Baromagnetic Effect in Antiperovskite $Mn_3Ga_{0.95}N_{0.94}$ by Neutron Powder Diffraction Analysis. *Advanced Materials* **28**(19), 3761–3767 (2016).

[156] Matsunami, D., Fujita, A., Takenaka, K., and Kano, M. Giant barocaloric effect enhanced by the frustration of the antiferromagnetic phase in Mn_3GaN. *Nature Materials* **14**(1), 73–78 (2015).

[157] Rendell-Bhatti, F., Zeng, M., Lloveras, P., Tamarit, J.L., Barrio, M., Connolly, E.T., MacLaren, D.A., Johnson, F., Cohen, L.F., and Boldrin, D. Improving barocaloric properties by tailoring transition hysteresis in $Mn_3Cu_{1-x}Sn_xN$ antiperovskites. *Journal of Physics: Energy* **5**(2), 024018 (2023).

[158] Lukashev, P. and Sabirianov, R.F. Flexomagnetic effect in frustrated triangular magnetic structures. *Physical Review B* **82**(9), 094417 (2010).

[159] Zemen, J., Mendive-Tapia, E., Gercsi, Z., Banerjee, R., Staunton, J.B., and Sandeman, K.G. Frustrated magnetism and caloric effects in Mn-based antiperovskite nitrides: Ab initio theory. *Physical Review B* **95**(18), 184438 (2017).

[160] Boldrin, D., Mihai, A.P., Zou, B., Zemen, J., Thompson, R., Ware, E., Neamtu, B.V., Ghivelder, L., Esser, B., McComb, D.W., Petrov, P., and Cohen, L.F. Giant Piezomagnetism in Mn_3NiN. *ACS Applied Materials & Interfaces* **10**(22), 18863–18868 (2018).

[161] Boldrin, D., Johnson, F., Thompson, R., Mihai, A.P., Zou, B., Zemen, J., Griffiths, J., Gubeljak, P., Ormandy, K.L., Manuel, P., Khalyavin, D.D., Ouladdiaf, B., Qureshi, N., Petrov, P., Branford, W., and Cohen, L.F. The Biaxial Strain Dependence of Magnetic Order in Spin Frustrated Mn_3NiN Thin Films. *Advanced Functional Materials* **29**(40), 1902502 (2019).

[162] Geilhufe, M., Achilles, S., Köbis, M.A., Arnold, M., Mertig, I., Hergert, W., and Ernst, A. Numerical solution of the relativistic single-site scattering problem for the Coulomb and the Mathieu potential. *Journal of Physics: Condensed Matter* **27**(43), 435202 (2015).

[163] Hoffmann, M., Ernst, A., Hergert, W., Antonov, V.N., Adeagbo, W.A., Matthias Geilhufe, R., and Ben Hamed, H. Magnetic and Electronic Properties of Complex Oxides from First-Principles. *physica status solidi (b)* **257**, 1900671 (2020).

[164] Perdew, J.P., Burke, K., and Ernzerhof, M. Generalized Gradient Approximation Made Simple. *Phys. Rev. Lett.* **77**(18), 3865–3868 (1996).

[165] Liechtenstein, A.I., Katsnelson, M.I., Antropov, V.P., and Gubanov, V.A. Local spin density functional approach to the theory of exchange interactions in ferromagnetic metals and alloys. *Journal of Magnetism and Magnetic Materials* **67**(1), 65 – 74 (1987).

[166] Halilov, S.V., Eschrig, H., Perlov, A.Y., and Oppeneer, P.M. Adiabatic spin dynamics from spin-density-functional theory: Application to Fe, Co, and Ni. *Phys. Rev. B* **58**(1), 293–302 (1998).

[167] Tyablikov, S. *Methods in the quantum theory of magnetism.* Plenum Press (1967).

[168] Huyen, V.T.N., Suzuki, M.T., Yamauchi, K., and Oguchi, T. Topology analysis for anomalous Hall effect in the noncollinear antiferromagnetic states of Mn_3AN (A=Ni, Cu, Zn, Ga, Ge, Pd, In, Sn, Ir, Pt). *Physical Review B* **100**(9), 094426 (2019).

[169] Ikeda, T., Tsunoda, M., Oogane, M., Oh, S., Morita, T., and Ando, Y. Anomalous Hall effect in polycrystalline Mn_3Sn thin films. *Applied Physics Letters* **113**(22), 222405 (2018).

[170] Bauer, G.E.W., Saitoh, E., and Wees, B.J.v. Spin caloritronics. *Nature Materials* **11**(5), 391–399 (2012).

[171] Mizuguchi, M. and Nakatsuji, S. Energy-harvesting materials based on the anomalous Nernst effect. *Science and Technology of Advanced Materials* **20**(1), 262–275 (2019).

[172] Puebla, J., Kim, J., Kondou, K., and Otani, Y. Spintronic devices for energy-efficient data storage and energy harvesting. *Communications Materials* **1**(1), 1–9 (2020).

[173] Xiao, D., Yao, Y., Fang, Z., and Niu, Q. Berry-Phase Effect in Anomalous Thermoelectric Transport. *Physical Review Letters* **97**(2), 026603 (2006).

[174] Zhou, X., Hanke, J.P., Feng, W., Blügel, S., Mokrousov, Y., and Yao, Y. Giant anomalous Nernst effect in noncollinear antiferromagnetic Mn-based antiperovskite nitrides. *Physical Review Materials* **4**(2), 024408 (2020).

[175] Singh, H.K., Samathrakis, I., Shen, C., and Zhang, H. Giant anomalous Hall and anomalous Nernst Conductivities in Antiperovskites and their Tunability via Magnetic Fields. *arXiv:2107.13496 [cond-mat]* (2021).

[176] Seemann, M., Ködderitzsch, D., Wimmer, S., and Ebert, H. Symmetry-imposed shape of linear response tensors. *Physical Review B* **92**(15), 155138 (2015).

[177] You, Y., Lam, H., Wan, C., Wan, C., Zhu, W., Han, L., Bai, H., Zhou, Y., Qiao, L., Chen, T., Pan, F., Liu, J., and Song, C. Anomalous Nernst Effect in an Antiperovskite Antiferromagnet. *Physical Review Applied* **18**(2), 024007 (2022).

[178] You, Y., Bai, H., Feng, X., Fan, X., Han, L., Zhou, X., Zhou, Y., Zhang, R., Chen, T., Pan, F., and Song, C. Cluster magnetic octupole induced out-of-plane spin polarization in antiperovskite antiferromagnet. *Nature Communications* **12**(1), 6524 (2021).

[179] Johnson, F., Zázvorka, J., Beran, L., Boldrin, D., Cohen, L.F., Zemen, J., and Veis, M. Room-temperature weak collinear ferrimagnet with symmetry-driven large intrinsic magneto-optic signatures. *Physical Review B* **107**(1), 014404 (2023).

[180] Bai, H., Zhou, X.F., Zhang, H.W., Kong, W.W., Liao, L.Y., Feng, X.Y., Chen, X.Z., You, Y.F., Zhou, Y.J., Han, L., Zhu, W.X., Pan, F., Fan, X.L., and Song, C. Control of spin-orbit torques through magnetic symmetry in differently oriented noncollinear antiferromagnetic Mn_3Pt. *Physical Review B* **104**(10), 104401 (2021).

[181] Sinova, J., Culcer, D., Niu, Q., Sinitsyn, N.A., Jungwirth, T., and MacDonald, A.H. Universal Intrinsic Spin Hall Effect. *Physical Review Letters* **92**(12), 126603 (2004).

[182] Nguyen, M.H. and Pai, C.F. Spin-orbit torque characterization in a nutshell. *APL Materials* **9**(3), 030902 (2021).

[183] Miron, I.M., Garello, K., Gaudin, G., Zermatten, P.J., Costache, M.V., Auffret, S., Bandiera, S., Rodmacq, B., Schuhl, A., and Gambardella, P. Perpendicular switching of a single ferromagnetic layer induced by in-plane current injection. *Nature* **476**(7359), 189–193 (2011).

[184] Han, X., Wang, X., Wan, C., Yu, G., and Lv, X. Spin-orbit torques: Materials, physics, and devices. *Applied Physics Letters* **118**(12), 120502 (2021).

[185] Fukami, S., Zhang, C., DuttaGupta, S., Kurenkov, A., and Ohno, H. Magnetization switching by spin-orbit torque in an antiferromagnet-ferromagnet bilayer system. *Nature Materials* **15**(5), 535–541 (2016).

[186] Zhang, W., Han, W., Yang, S.H., Sun, Y., Zhang, Y., Yan, B., and Parkin, S.S.P. Giant facet-dependent spin-orbit torque and spin Hall conductivity in the triangular antiferromagnet $IrMn_3$. *Science Advances* **2**(9), e1600759 (2016).

[187] Chen, X., Shi, S., Shi, G., Fan, X., Song, C., Zhou, X., Bai, H., Liao, L., Zhou, Y., Zhang, H., Li, A., Chen, Y., Han, X., Jiang, S., Zhu, Z., Wu, H., Wang, X., Xue, D., Yang, H., and Pan, F. Observation of the antiferromagnetic spin Hall effect. *Nature Materials* **20**(6), 800–804 (2021).

[188] Kimata, M., Chen, H., Kondou, K., Sugimoto, S., Muduli, P.K., Ikhlas, M., Omori, Y., Tomita, T., MacDonald, A.H., Nakatsuji, S., and Otani, Y. Magnetic and magnetic inverse spin Hall effects in a non-collinear antiferromagnet. *Nature* **565**(7741), 627–630 (2019).

[189] Yu, L., Karube, S., Liu, M., Tsunoda, M., Oogane, M., and Ando, Y. Observation of unconventional spin-polarization induced spin-orbit torque in $L1_2$-ordered antiferromagnetic Mn_3Pt thin films. *Applied Physics Express* **15**(3), 033002 (2022).

[190] Higo, T., Man, H., Gopman, D.B., Wu, L., Koretsune, T., van 't Erve, O.M.J., Kabanov, Y.P., Rees, D., Li, Y., Suzuki, M.T., Patankar, S., Ikhlas, M., Chien, C.L., Arita, R., Shull, R.D., Orenstein, J., and Nakatsuji, S. Large magneto-optical Kerr effect and imaging of magnetic octupole domains in an antiferromagnetic metal. *Nature Photonics* **12**(2), 73–78 (2018).

[191] Reichlova, H., Janda, T., Godinho, J., Markou, A., Kriegner, D., Schlitz, R., Zelezny, J., Soban, Z., Bejarano, M., Schultheiss, H., Nemec, P., Jungwirth, T.,

Felser, C., Wunderlich, J., and Goennenwein, S.T.B. Imaging and writing magnetic domains in the non-collinear antiferromagnet Mn_3Sn. *Nature Communications* **10**(1), 1–6 (2019).

[192] Köppel, H., Yarkony, D.R., and Barentzen, H., editors. *The Jahn-Teller Effect: Fundamentals and Implications for Physics and Chemistry*, volume 97 of *Springer Series in Chemical Physics*. Springer Berlin Heidelberg (2009).

[193] Wadley, P., Howells, B., Železný, J., Andrews, C., Hills, V., Campion, R.P., Novák, V., Olejník, K., Maccherozzi, F., Dhesi, S.S., Martin, S.Y., Wagner, T., Wunderlich, J., Freimuth, F., Mokrousov, Y., Kuneš, J., Chauhan, J.S., Grzybowski, M.J., Rushforth, A.W., Edmonds, K.W., Gallagher, B.L., and Jungwirth, T. Electrical switching of an antiferromagnet. *Science* **351**(6273), 587–590 (2016).

[194] Chen, X., Zhou, X., Cheng, R., Song, C., Zhang, J., Wu, Y., Ba, Y., Li, H., Sun, Y., You, Y., Zhao, Y., and Pan, F. Electric field control of Néel spin-orbit torque in an antiferromagnet. *Nature Materials* **18**(9), 931–935 (2019).

[195] Šmejkal, L., Sinova, J., and Jungwirth, T. Emerging Research Landscape of Altermagnetism. *Physical Review X* **12**(4), 040501 (2022).

[196] Liu, L., Moriyama, T., Ralph, D.C., and Buhrman, R.A. Spin-Torque Ferromagnetic Resonance Induced by the Spin Hall Effect. *Physical Review Letters* **106**(3), 036601 (2011).

[197] Liu, Y. and Shao, Q. Two-Dimensional Materials for Energy-Efficient Spin–Orbit Torque Devices. *ACS Nano* **14**(8), 9389–9407 (2020).

[198] Kondou, K., Chen, H., Tomita, T., Ikhlas, M., Higo, T., MacDonald, A.H., Nakatsuji, S., and Otani, Y. Giant field-like torque by the out-of-plane magnetic spin Hall effect in a topological antiferromagnet. *Nature Communications* **12**(1), 6491 (2021).

[199] Hazra, B.K., Pal, B., Jeon, J.C., Neumann, R.R., Goebel, B., Grover, B., Deniz, H., Styervoyedov, A., Meyerheim, H., Mertig, I., Yang, S.H., and Parkin, S.S.P. Generation of out-of-plane polarized spin current by spin swapping (2022). ArXiv:2211.12398 [cond-mat].

[200] Karimeddiny, S., Mittelstaedt, J.A., Buhrman, R.A., and Ralph, D.C. Transverse and Longitudinal Spin-Torque Ferromagnetic Resonance for Improved Measurement of Spin-Orbit Torque. *Physical Review Applied* **14**(2), 024024 (2020).

[201] Cham, T.M., Karimeddiny, S., Gupta, V., Mittelstaedt, J.A., and Ralph, D.C. Separation of Artifacts from Spin-Torque Ferromagnetic Resonance Measurements of Spin-Orbit Torque for the Low-Symmetry Van der Waals Semi-Metal $ZrTe_3$. *Advanced Quantum Technologies* **5**(2), 2100111 (2022).

[202] Go, D., Jo, D., Kim, C., and Lee, H.W. Intrinsic Spin and Orbital Hall Effects from Orbital Texture. *Physical Review Letters* **121**(8), 086602 (2018).

[203] Go, D., Jo, D., Lee, H.W., Kläui, M., and Mokrousov, Y. Orbitronics: Orbital currents in solids. *EPL (Europhysics Letters)* **135**(3), 37001 (2021).